UNIVERSIDADE DE BRASÍLIA – UNB

INSTITUTO DE GEOCIÊNCIAS – IG

PÓS-GRADUAÇÃO EM GEOLOGIA

# ESPECTRORRADIOMETRIA DE REFLECTÂNCIA APLICADA À ANÁLISE QUANTITATIVA DA MINERALOGIA DO DEPÓSITO N4WS, PROVÍNCIA MINERAL DE CARAJÁS, PARÁ, BRASIL.

**Elias Martins Guerra Prado**

**Dissertação de Mestrado nº 342**

**Orientadora: Profa. Dra. Adalene Moreira Silva**

**Co-orientador: Dr. Diego Fernando Ducart**

**BRASÍLIA - DF**

**2015**

ELIAS MARTINS GUERRA PRADO

# ESPECTRORRADIOMETRIA DE REFLECTÂNCIA APLICADA À ANÁLISE QUANTITATIVA DA MINERALOGIA DO DEPÓSITO N4WS, PROVÍNCIA MINERAL DE CARAJÁS, PARÁ, BRASIL.

Dissertação de mestrado elaborada junto ao curso de Pós-Graduação em Geologia (Área de concentração em Geologia Econômica), Instituto de Geociências, Universidade de Brasília, como requisito parcial para a obtenção do título de Mestre em Geologia.

Orientador: Prof. Dra. Adalene Moreira Silva

Co-orientador Dr. Diego Fernando Ducart

Banca examinadora:

Prof. Dra. Adalene Moreira Silva (Presidente)

Prof. Dr. Álvaro Penteado Crósta (IG-UNICAMP)

Prof. Dr. Farid Chemale Jr. (IG-UnB)

BRASÍLIA - DF

2015

## FICHA CATALOGRÁFICA

Prado, Elias Martins Guerra

Espectrorradiometria de reflectância aplicada à análise quantitativa da mineralogia do depósito N4WS, Província Mineral de Carajás, Pará, Brasil – Brasília, 2015.

Nº de páginas: 107

Área de concentração: Geologia Econômica e Prospecção Mineral

Orientadora: Profa. Dra. Adalene Moreira Silva

# AGRADECIMENTOS

A memoria de meu pai, Edson Martins de Oliveira, e a minha mãe, Germana Albuquerque Guerra, a eles todos os créditos dedico.

A toda equipe envolvida no projeto do depósito N4WS, Vitor Nascimento Ferreira, Marta Henriques Jácomo, Luciano Mozer de Assis, Prof.ª Dra. Catarina Labouré Bemfica Toledo e Pedro Luiz Gomez Martins sem os quais este caminho teria sido mais difícil.

Aos meus orientadores, Prof.ª Dra. Adalene Moreira Silva e Dr. Diego Fernando Ducart, pela dedicação e orientação neste período de aprendizado.

A Vale S.A. pela disponibilização das bases de dados.

“Aprenda como se você fosse viver para sempre. Viva como se você fosse morrer amanhã.”

Mahatma Gandhi.

# SUMÁRIO

## LISTA DE FIGURAS E TABELAS

# RESUMO

## ESPECTRORADIOMETRIA DE REFLECTÂNCIA APLICADA À CARACTERIZAÇÃO MINERALÓGICA DO DEPÓSITO DE FERRO N4W, CARAJÁS, BRASIL

A quantificação da abundância e da físico-química mineral utilizando a espectrorradiometria de reflectância no visível, infravermelho próximo e infravermelho de ondas curtas (região entre 400-2.500nm) é um ferramenta importante na exploração mineral. Neste trabalho foram obtidos espectros de reflectância de testemunhos de sondagem do depósito de ferro de classe mundial N4WS, localizado na Província Mineral de Carajás. Estes espectros foram validados utilizando analises geoquímicas de fluorescência de raio-x (XRF) e lâminas delgadas. Os espectros de reflectância foram coletados utilizando o espectrorradiômetro ASD FielsSpec em 9 testemunhos de sondagem. A mineralogia do depósito é predominantemente hematita, com quantidades menores de magnetita, goetita, quartzo, caulinita, gibbsita, esmectita, talco, carbonato e clorita. A mineralogia do depósito de ferro foi extraída dos dados espectrais utilizando a geometria (profundidade e comprimento de onda) do espectro de reflectância removido do contínuo. A profundidade das feições de absorção é proporcional à abundância mineral e o comprimento de onda proporcional à composição química. As feições de absorção diagnósticas de cada mineral foram utilizadas para determinar a abundância e a composição mineral. Os produtos finais incluem: abundância de (hidrox-)óxido de ferro (RMSE 15,8 %$Fe_2O_3$); Abundância de argilas aluminosas (RMSE 6 %$Al_2O_3$); abundância de talco (RMSE 8 %MgO); identificação do tipo de argila (caulinita, montmorilonita, gibbsita); composição do carbonato (dolomita vs. calcita); e composição da clorita (Mg vs. Fe). Os resultados de abundância e composição mineral obtidos permitem uma caracterização efetiva do minério, protominério e encaixantes, e mostram variações dentro do corpo de minério.

**Descritores:** Província Mineral de Carajás**,** Espectrorradiometria de reflectância, Minério de ferro.

## ABSTRACT

## Reflectance Spectroradiometry Applied to a Quantitative Analysis of the Mineralogy of the N4WS Deposit, Carajás Mineral Province, Pará, Brazil.

Quantifying the abundance and physicochemical properties of minerals using reflectance spectroradiometry in the visible, near infrared and shortwave infrared (400-2,500 nm) regions is an important tool in mineral exploration. In this study, the reflectance spectra of drill cores from the world-class N4WS iron deposit located in the Carajás Mineral Province, Brazil, were obtained. These spectra were validated using a geochemical analysis of X-ray fluorescence (XRF) and thin sections. The reflectance spectra were collected using an FieldSpec 3 spectroradiometer (ASD, Boulder, Colorado, USA) in 9 drill cores. The mineralogy of the deposit is mainly hematite, with lesser amounts of magnetite, goethite, quartz, kaolinite, gibbsite, smectite, talc, carbonate and chlorite. The mineralogy of the iron deposit was extracted from the spectral data using the geometry (depth and wavelength) of the reflectance spectrum removed from the continuum. The depth of the absorption features is proportional to the mineral abundance, and the wavelength is proportional to the mineral chemical composition. The diagnostic absorption features of each mineral were used to determine the mineral abundance and composition. The final products include the abundance of iron (hydro) oxide (15.8% root-mean-square error [RMSE] Fe2O3); abundance of aluminous clays (RMSE 6% Al2O3); abundance of talc (8% RMSE MgO); identification of clay type (kaolinite, montmorillonite or gibbsite); composition of carbonate (dolomite vs. calcite); and composition of chlorite (Mg vs. Fe). The mineral abundance and composition results provided an effective characterisation of the ore, protore and host rocks and showed variations within the ore body.

**Key words:** Carajás Mineral Province, reflectance spectroradiometry, iron ore.

# 1 INTRODUÇÃO

# 1 INTRODUÇÃO

A espectroradiometria de reflectância é uma técnica muito conhecida e efetiva para a identificação da mineralogia de depósitos minerais nas diferentes etapas da exploração mineral (Herrmann et al., 2001; Ducart et al., 2006; Silva et al., 2009; Harraden et al., 2013; Dalm et al., 2014). A análise espectral destes depósitos permite o melhor entendimento das zonas mineralizadas, auxiliando tanto no entendimento da distribuição espacial do minério, como dos contaminantes (Ducart et al., 2006; Silva et al., 2009).

A quantificação pode ser feita por meio da correlação dos dados espectrais com bibliotecas espectrais, que apresentam espectros de amostras com composição mineralógica conhecida, ou por meio da correlação dos dados espectrais com dados multi-fonte, como dados geoquímicos e propriedades físicas de rocha (Clark e Roush, 1984; Cudahy et al., 2008; Haest et al., 2012).

Para realizar a análise quantitativa da mineralogia de um rocha por meio da espectroradiometria de reflectância deve-se supor que: (1) A energia eletromagnética medida percorreu a mesma distância durante sua trajetória, da fonte luminosa para amostra e da amostra para o sensor (cf. Clark e Roush, 1984); (2) A intensidade de absorção de um determinado mineral, relativa ao *background* (normalmente considerada como o contínuo do espectro), é função do coeficiente de absorção do mineral  e de sua abundância. Quando o mineral é identificado, a abundância do mineral pode ser determinada pela intensidade de absorção (Hunt e Ashley, 1979; Clark e Roush, 1984); (3) A composição química de um determinado mineral determina o comprimento de onda de sua feição de absorção diagnóstica (cf. Hunt e Salisbury, 1971; Clark et al., 1990; Cudahy e Ramanaidou, 1997); (4) O espalhamento (orientação do cristal, tamanho/distribuição/orientação das partículas) é isotrópico (cf. Adams e Filice, 1967; Clark e Roush, 1984; Morris et al., 1985).

Uma variedade de métodos podem ser utilizados para extrair as informações minerais dos espectros de reflectância: razões de bandas (Crowley et al., 1989); ajustes polinomiais (Cudahy et al., 2008); gaussianos (Mustard, 1992); e métodos estatísticos supervisionados como análise de variáveis canônicas (ex. The Spectral Assistant TM, Berman et al., 1999), minimos quadrados (ex. Tetracorder, Clark et al., 2003), e minimos quadrados parciais (Haaland e Thomas, 1988; Nadler e Coifman, 2005). Todos estes métodos não se baseiam em obter o coeficiente de absorção em um determinado comprimento de onda, mas em extrair informações a respeito de minerais específicos por meio da correlação dos dados espectrais com bibliotecas espectrais ou com dados independentes, como análises químicas.

A partir deste enfoque metodológico, por meio da análise de dados espectrorradiométricos e do desenvolvimento de novas procedimentos de análise e integração, pretende-se contribuir para a aplicação da espectroradiometria de reflectância como uma uma técnica efetiva para a identificação da mineralogia de depósitos minerais nas diferentes etapas da exploração mineral do minério de ferro. Os resultados compõem uma das vertentes de um projeto maior intitulado "Geração de modelos prospectivos para minério de ferro", desenvolvido pela Universidade de Brasília em parceria com a Vale S.A. e envolve subsídios financeiros e apoio técnico-científico.

## 1.1OBJETIVO

O objetivo central é desenvolver um método para aplicação da espectrorradiometria de reflectância no mapeamento de formação ferrífera bandada e do minério de ferro do depósito de N4WS, por meio das suas assembleias minerais de alteração e suas relações espaciais e temporais com base em dados de testemunhos de sondagem e sua comparação com dados geológicos, petrográficos, geoquímicos e de propriedades físicas de rocha.

Para que o objetivo central fosse atingido, traçaram-se os seguintes objetivos específicos:

- ✓Identificar as variações mineralógicas dos diversos litotipos do depósito N4WS;
- ✓Quantificar a mineralogia identificada a partir da correlação dos dados espectrais com análises geoquímicas (XRF e Titulação);

- ✓Analisar a distribuição mineralógica em 1D e em 2D dos litotipos do depósito N4WS e comparar com os dados de susceptibilidade magnética e geoquímica de rocha;
- ✓Avaliar a utilização da espectroradiometria de reflectância para a análise sistemática em testemunhos de sondagem;

## 1.2LOCALIZAÇÃO E ACESSO

O depósito N4WS, alvo do presente trabalho, está localizada no distrito mineiro Serra Norte, Província Mineral de Carajás – PA, e faz parte dos depósitos de ferro encontrados na Serra Norte, e têm Paraupebas como município referente. O município de Paraupebas se encontra no sudeste do estado do Pará, o acesso é feito via Belém (PA), pela rodovia pavimentada BR 010, seguindo sentido sul, sudoeste para a cidade de Marabá que se encontra na rodovia pavimentada BR 230 (Figura 1.1).

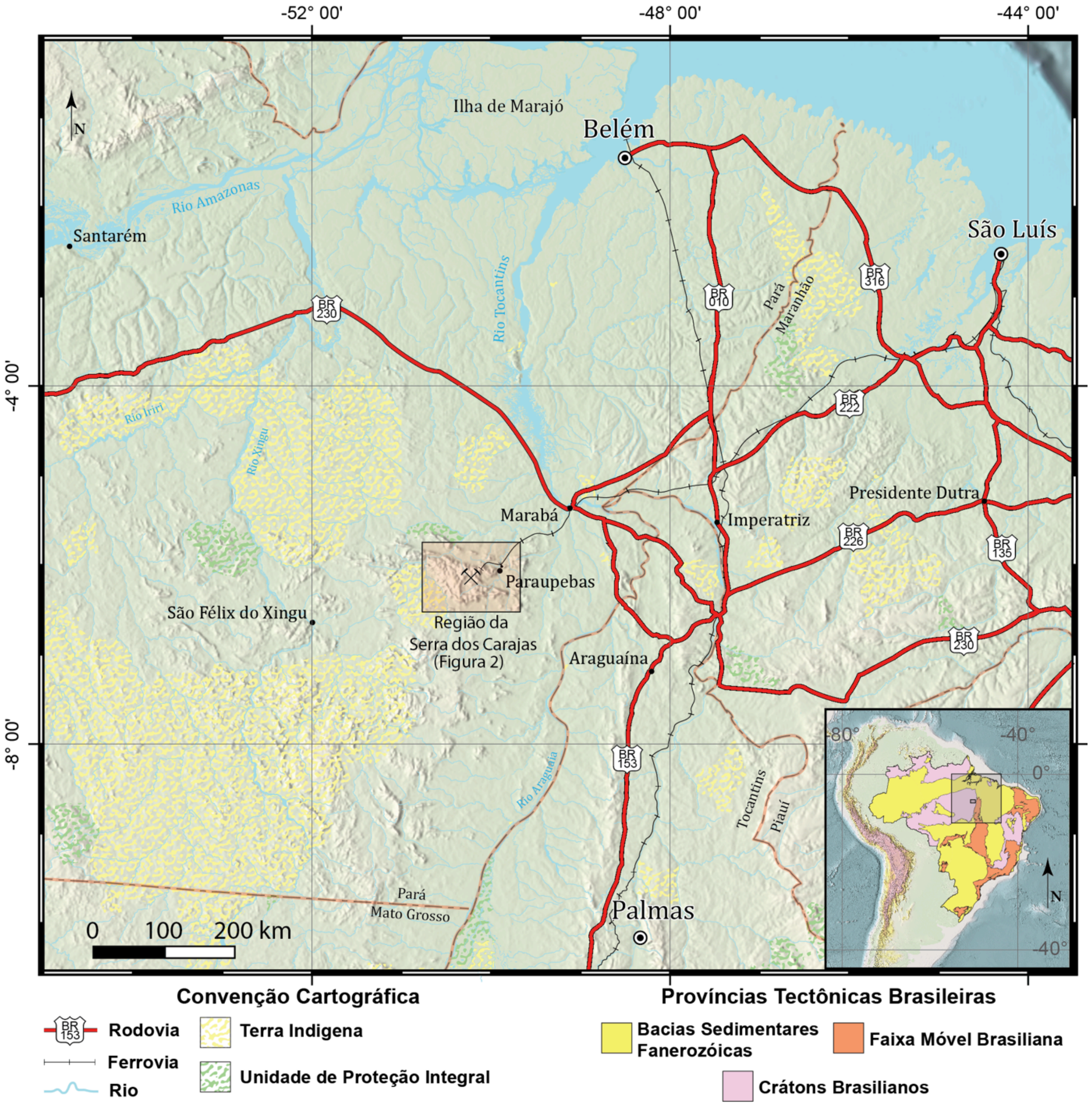

**Figura 1.1** Mapa de localização da região da Serra dos Carajás, mostrando as principais vias de acesso, unidades de proteção integral e terras indígenas. No canto inferior direito, apresenta-se a localização da área de estudo em relação às Províncias Tectônicas Brasileiras definidas por Almeida et al.( 1977).

# 2 MATERIAIS E METODOS

# 2 MATERIAIS E METODOS

A seguir apresentam-se os materiais utilizados para elaboração da presente dissertação de mestrado, bem como a metodologia desenvolvida para aplicação de espectrorradiometria de reflectância em testemunhos de sondagem de formações ferríferas bandadas.

## 2.1MATERIAIS

As amostras deste estudo foram coletadas em testemunhos correspondentes a nove sondagens, distribuídas em três seções na direção EW que seccionam o depósito de N4WS. Cada furo de sondagem foi amostrado de dois em dois metros, onde foram coletadas amostras representativas de 15 cm , o que totalizam 1766 amostras . As amostras foram seccionadas ao meio na laminação para facilitar a análise, sendo que uma parte foi separada para análise geoquímica (XRF, ICP-MS, ICP-AES e Titulação) e a outra metade foi utilizada para medições a aquisição de dados espectrorradiométricos. Algumas amostras foram selecionadas para a confecção de lâminas delgadas, com o intuito de validar os minerais identificados pela análise espectral. Dados de susceptibilidade magnética obtido de Ferreira (2014) também foram utilizados para comparar os intervalos mapeados e para auxiliar na interpretação dos resultados.

O espectro de reflectância das amostras foi medido utilizando espectrorradiômetro de reflectância FieldSpec3 Hi-Res® (ASD). As medidas foram realizadas utilizando a sonda de contato, que apresenta como fonte de luz uma lâmpada de halogênio. A janela de aquisição da sonda de contato tem área de 1 cm$^2$, e o espectro salvo representa a média de 75 espectros coletados na mesma área. Ao total foram efetuadas 5111 medidas.

Este trabalho utiliza um espectrômetro de reflectância pontual (ASD FieldSpec) com uma sonda de contato para a coleta dos dados. A sonda de contato apresenta iluminação interna, e a coleta do dado é feita com a sonda em contato direto com a amostra.

O dispositivo coleta os espectros em três módulos, o primeiro cobrindo os comprimentos de onda do visível ao infravermelho próximo (VNIR: 350-1000 nm) e o segundo cobre a região do infravermelho de ondas curtas (SWIR: 1.000-2500 nm). O intervalo de amostragem do espectrômetro é de 1,4 nm no VNIR e de 2,0 nm do SWIR, com uma precisão de comprimento de onda de ±0,5 nm. A resolução espectral é de 3 nm no VNIR e 8 nm no SWIR. Os espectros coletados pelo ASD são convertidos de radiação para reflectância utilizando o sinal do Spectralom™, coletado por meio de uma calibração feita a cada 20 minutos durante a coleta dos dados.

Os dados foram analisados por meio do software comercial "The Spectral Geologist" (TSG Core™, versão 7.1.0.062). O software foi utilizado para processar os dados espectrais de reflectância, obter os parâmetros espectrais e extrair as informações de abundância mineral, composição e cristalinidade.

Foram confeccionadas e descritas seis lâminas delgadas polidas com intuito de comparar a mineralogia observada nas lâminas com a mineralogia obtida pelos dados de espectrorradiometria de reflectância.

A preparação e a análise das amostras foram realizadas nos laboratórios da ALS Minerals e as dosagens de elementos maiores, menores e traço foram efetuadas a partir de quatro métodos distintos (Tabela 2.1): XRF (Fluorescência de Raio-X) e Titulação. A titulação do ferro foi utilizado pois as demais análises não permitem a diferenciação entre $Fe^{2+}$ e $Fe^{3+}$, o que é de suma importância para o estudo de formações ferríferas. Para minimizar custos o ferro férrico ($Fe^{3+}$) foi calculado utilizando o ferro ferroso ($Fe^{2+}$) e o ferro total ($Fe_2O_3$). O banco de metadados geoquímicos foi importado dentro do software TSG para análise dos resultados espectrais.

Tabela 2.1 Métodos de análise química de rocha total utilizados dentro do Projeto Ferro Carajás. O banco de metadados geoquímicos foi importado dentro do software TSG para análise dos resultados espectrais.

| *Fluorescência de Raio-X (ME-XRF06)* | *Titulação (Fe-VOL05)* |
|---|---|
| $SiO_2$, $Al_2O_3$, CaO, $TiO_2$, $Fe_2O_3$, $P_2O_5$, BaO, MgO, $Na_2O$, $K_2O$, $Cr_2O_3$, MnO e SrO | FeO |

## 2.2METODOLOGIA PARA AQUISIÇÃO DOS DADOS ESPECTRAIS

A metodologia de coleta dos dados foi desenvolvida a partir de experimentos realizados em uma etapa preliminar, com o intuito de investigar qual sensor (pistola ou sonda de contato) apresenta maior acurácia e precisão. Para isso, foi analisado o espectro de uma amostra obtido por diferentes métodos de aquisição, utilizando a pistola e a sonda de contato.

Foi escolhida uma amostra de testemunho de sondagem do deposito N4WS, que possui o bandamento típico das formações ferríferas bandadas, com níveis de óxido de ferro e jaspe intercalados. A amostra foi serrada ao meio, para que as medições fossem efetuadas na superfície serrada da amostra.

A análise quantitativa dos dados espectrais é uma técnica conhecida e estudada há alguns anos. Entretanto, devido à variedade de sensores disponíveis para a coleta dos dados, não existe uma metodologia padrão para este tipo de análise. Em geral, nos trabalhos que utilizam a técnica para quantificar a mineralogia de solos, os espectros são obtidos com espectrômetros de reflectância difusa (Fernandes et al., 2004; Carioca et al., 2011, Gonçalves et al., 2012). Nos trabalhos em que a técnica é utilizada para quantificar a mineralogia de amostras de rocha, os espectros geralmente são obtidos por espectrômetros de reflectância portáreis (ex. ASD, PIMA; Yang et al., 2011, Sonntag et al., 2012), espectrômetros montados em sistemas robotizados (ex. HyLogger System; Haest et al., 2012), ou por *scanners* hiperespectrais (Ross et al., 2013). Este trabalho utiliza um espectrômetro de reflectância pontual (ASD FieldSpec), que tem a opção de dois sensores para coleta dos dados, a pistola ou a sonda de contato. A pistola necessita de uma fonte luminosa externa para a coleta dos dados, portanto deve-se definir uma configuração de posicionamento (distância, inclinação e altura) da pistola (sensor), da fonte luminosa e da amostra para que as medidas sejam realizadas. A sonda de contato apresenta iluminação interna, e a coleta do dado é feita com a sonda em contato direto com a amostra. As análises quantitativas de dados espectrais obtidos por espectrômetros como este podem ser realizadas utilizando ambos sensores (pistola ou sonda de contato), entretanto não existem estudos que apontam qual seria o melhor sensor para este tipo de análise.

As medições efetuadas com a pistola foram realizadas em quatro configurações, variando o ângulo de inclinação da pistola e da iluminação (60° e 80°), e o ângulo entre a pistola e a iluminação (180° e 90°; Figura 2.1). A altura da pistola foi calculada para que a janela de aquisição dos dados estivesse completamente dentro da área da amostra. A amostra utilizada para os experimentos apresentava 5 cm de largura, portanto o raio da janela de aquisição foi calculada para ser de 1.5 cm. A altura da lâmpada foi fixada em 50 cm.

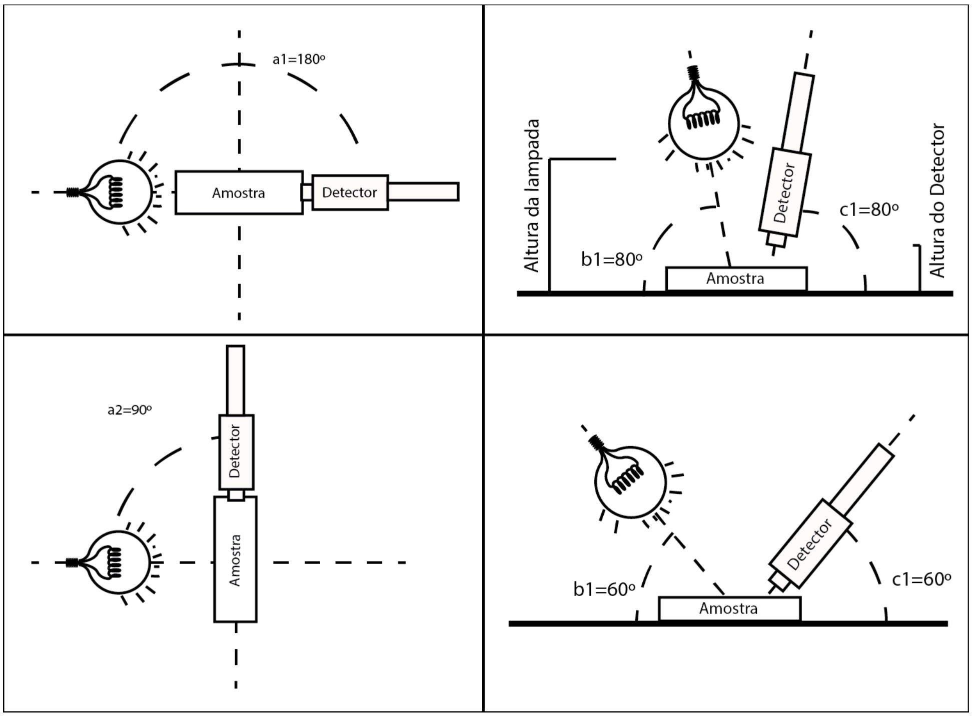

**Figura 2.1** Configurações utilizadas para efetuar as medições com a pistola. À esquerda variando o ângulo entre a pistola e a iluminação e à direita variando o ângulo de inclinação da pistola e da iluminação.

Duas medidas foram realizadas em cada configuração, uma ao lado da outra, com o objetivo de recobrir toda a área da amostra.

A sonda de contato possui uma janela de aquisição de 1 cm de diâmetro, e as medidas realizadas foram efetuadas em sequência, uma ao lado da outra. Dois métodos de amostragem foram analisados utilizando a sonda de contato, sendo eles: a. realizando uma sequência de medições em uma linha, no centro da amostra; b. realizando a sequência de medições em duas linhas. Em ambos os métodos as linhas são paralelas ao comprimento da amostra (Figura 2.2).

Após a aquisição dos dados, a média dos espectros de cada método de amostragem foi calculada, obtendo apenas um espectro médio para cada método. Estes espectros médios foram comparados quanto à razão sinal/ruído no VNIR e no SWIR, e quanto à repetibilidade dos parâmetros espectrais. Todos os espectros apresentavam feições espectrais características da hematita, logo os parâmetros espectrais analisados foram: a máxima reflectância entre 650-750 nm (pico do vermelho), a profundidade da mínima reflectância entre 700-1050 nm e seu comprimento de onda (Curtis, 1985; Morris et al., 1985).

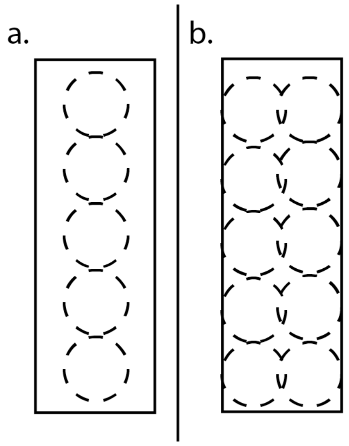

**Figura 2.2**-Metodologia utilizada nas medida realizadas com a sonda de contato. a. medições realizadas em apenas uma linha no centro da amostra. b. medições realizadas em duas linhas. Círculos pontilhados representam a área de contato da sonda.

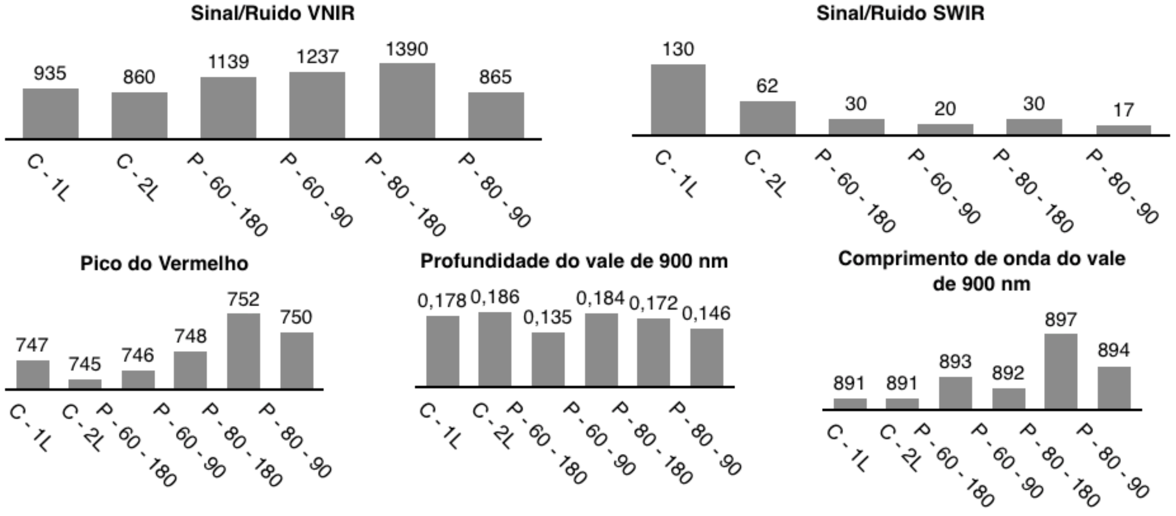

**Figura 2.3**Gráficos elaborados para comparar a razão sinal/ruído e os parâmetros espectrais de cada método.C-1L = Sonda de Contato, 1 linha; C-2L = Sonda de Contato, 2 linhas; P-60-180 = Pistola, 60° em relação a horizontal e a 180° da iluminação; P-60-90 = Pistola, 60° em relação a horizontal e a 90° da iluminação; P-80-180 = Pistola, 80° em relação a horizontal e a 180° da iluminação; P-80-90 = Pistola, 80° em relação a horizontal e a 90° da iluminação.

No VNIR a razão sinal/ruído das medidas realizadas com a pistola foi até 48% maior, e no SWIR a da sonda de contato foi até 330% maiores (Figura 2.3). Entretanto, ao analisar os espectros na região do VNIR, observa-se que o ruído associado a diminuição da razão sinal/ruído das medidas realizadas com a sonda de contato se encontra entre 350-450 nm, região que não apresenta feições espectrais características. O ruído no SWIR das medidas realizadas com a pistola se encontra entre 2100-2500 nm, podendo comprometer feições diagnósticas de alguns minerais (Figura 2.4).

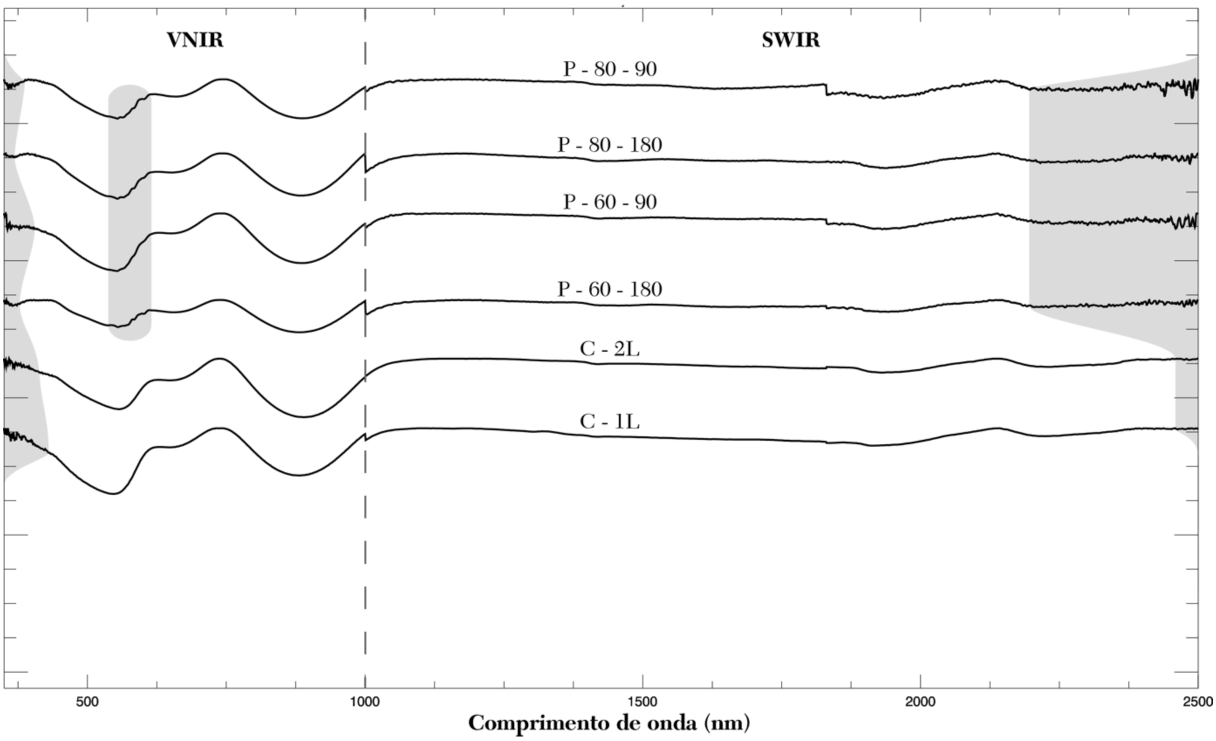

**Figura 2.4** Média dos espectros obtidos em cada um dos métodos analisados. Regiões sombreadas destacam o ruído dos espectros. C-1L = Sonda de Contato, 1 linha; C-2L = Sonda de Contato, 2 linhas; P-60-180 = Pistola, 60° em relação a horizontal e a 180º da iluminação; P-60-90 = Pistola, 60° em relação a horizontal e a 90° da iluminação; P-80-180 = Pistola, 80° em relação a horizontal e a 180° da iluminação; P-80-90 = Pistola, 80° em relação a horizontal e a 90° da iluminação.

Os espectros da pistola, apesar de apresentarem uma razão sinal/ruído até 48% maior no VNIR, se encontram ruidosos entre 520-600 nm (Figura 2.4), região do visível importante para identificação de óxidos.

Os parâmetros espectrais das medidas realizadas com as duas metodologias propostas para sonda de contato não apresentaram grandes variações, variando em até 4,5%, diferente dos parâmetros obtidos com as quatro medidas da pistola, que apresentaram valores distintos para cada arranjo (Figura 2.3), variando em até 36%.

O resultado dos experimentos mostra que utilizar a sonda de contado realizando medições em 2 linhas é a metodologia mais adequada para o presente estudo. A ausência de ruído em comprimentos de onda que podem apresentar feições diagnósticas de alguns minerais, e a repetibilidade dos parâmetros espectrais tornam a sonda de contato mais precisa que a pistola. A geometria fixa do ângulo de iluminação e do sensor dentro da sonda de contato e a facilidade de estabelecer uma distância lâmpada-amostra-sensor fixa, permitem que sonda seja mais precisa que a pistola.

## 2.3EMBASAMENTO TEÓRICO

A luz ao interagir com um mineral ou rocha, é preferencialmente absorvida em certos comprimentos de onda, enquanto que em outros comprimentos de onda é transmitida e refletida. Reflectância é definida como a razão entre a intensidade de luz refletida pela amostra e a intensidade de luz incidente (Van der Meer, 2004). Processos de transição eletrônica e transferência de carga (ex. mudança no estado eletrônico de elétrons ligados a átomos ou moléculas) associados a íons de metais de transição como Fe, Ti, Cr, etc., determinam, em grande parte, a posição das feições diagnósticas de absorção dos espectros de alguns minerais na região do VNIR e SWIR (Hunt, 1977; Burns, 1993; Adams, 1974, 1975). Processos de vibração relacionados a $H_2O$ e OH-, também produzem feições de absorção características no SWIR (Hunt, 1977).

A posição, forma e profundidade destas feições de absorção são controladas pela estrutura cristalina em que estes átomos e moléculas absorventes se encontram, e pela estrutura química do material. Logo, as variáveis que caracterizam estas feições de absorção (parâmetros espectrais) podem ser diretamente correlacionadas com a composição química e estrutura cristalina da amostra (Van der Meer, 2004). Os parâmetros espectrais são obtidos da curva polinomial que melhor se ajusta ao espectro de reflectância removido do contínuo. O contínuo é o albedo total da curva de reflectância (Figura 2.5). Matematicamente o espectro removido do contínuo é obtido pela seguinte equação (Clark et al., 2003):

$$L_c(w) = \frac{L(w)}{C_1(w)}$$

onde L(w) é o espectro obtido em função do comprimento de onda, $C_1(w)$ é o contínuo do espectro obtido e $L_c(w)$ é o espectro removido do contínuo.

A posição da feição de absorção é definida como o comprimento de onda em que feição de absorção chega ao mínimo de reflectância da curva, e a posição de uma feição de reflectância é definida como comprimento de onda em que a feição chega ao máximo de reflectância da curva. A profundidade da feição de absorção foi calculada neste estudo utilizando o método de Clark e Roush (1984), subtraindo o valor de reflectância do mínimo da curva polinomial pelo valor de reflectância do contínuo no mesmo comprimento de onda, e dividindo este valor pela reflectância do contínuo. Quando a feição de absorção não está presente no espectro analisado, o valor da profundidade é próximo ou igual a zero, indicando a ausência do mineral investigado. O fator de assimetria da feição é definido por Van der Meer (2004) como a razão entre as áreas a direita e a esquerda do comprimento de onda de mínima reflectância. A inclinação de uma determinada região do espectro é calculada obtendo o coeficiente angular da reta tangente a esta região (Figura 2.5).

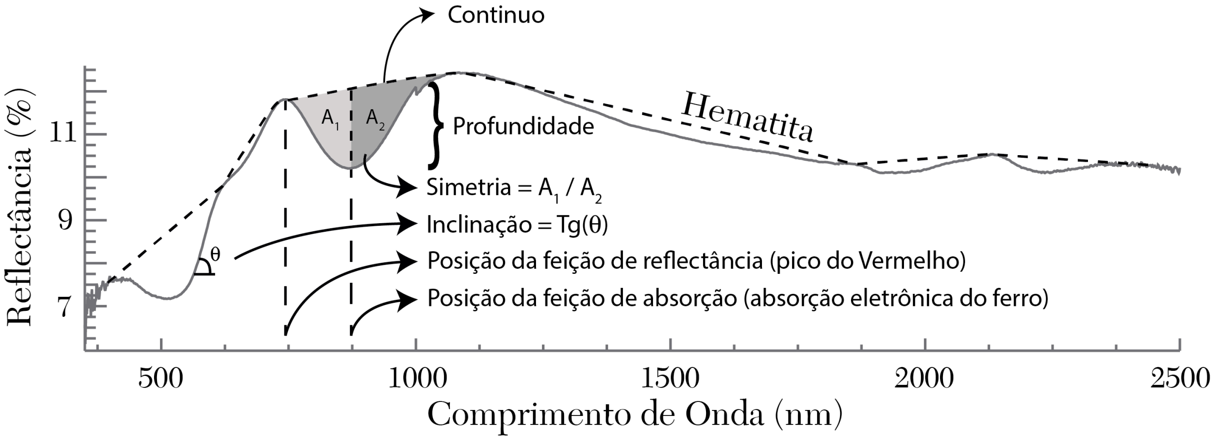

**Figura 2.5** Parâmetros espectrais obtidos dos espectros médios de cada método de amostragem.

Inicialmente, foram calculados parâmetros espectrais de feições de absorção individuais como a profundidade, o comprimento de onda ou a razão entre bandas espectrais. Estes parâmetros foram então integrados para gerar as informações de abundância, composição e cristalinidade dos minerais. Além dos parâmetros espectrais desenvolvidos neste trabalho, alguns parâmetros foram baseados nos propostos por Haest et al. (2012), e adaptados ao projeto.

# 3 ESTRUTURA DA DISSERTAÇÃO

# 3 ESTRUTURA DA DISSERTAÇÃO

Este projeto de pesquisa foi desenvolvido no Instituto de Geociêncidas da Universidade de Brasília sob a orientação da Professora Dra. Adalene Moreira Silva e faz parte do projeto “Geração de modelos prospectivos para o minério de ferro”, um projeto de cooperação com a empresa Vale S.A e interveniência da FUNAPE (Fundação de Apoio a Pesquisa).

A dissertação de mestrado está estruturada em três partes, sendo a primeira constituída do corpo principal do projeto, onde é apresentada a introdução ao problema estudado, os objetivos da dissertação, os materiais e métodos utilizados. A segunda parte está organizada em formato de artigo, em língua inglesa, a ser submetido à *Ore Geology Reviews*, intitulado “Espectrorradiometria de reflectância aplicada à análise quantitativa da mineralogia do depósito N4WS, Província Mineral de Carajás, Pará, Brasil.”. Na terceira parte, encontram-se discussões e considerações sobre os resultados obtidos bem como as principais conclusões sobre a aplicabilidade do método em estudos de exploração mineral futuros.

# 4 ARTIGO CIENTÍFICO

# 4 ARTIGO CIENTÍFICO

## Reflectance Spectroradiometry Applied to a Quantitative Analysis of the Mineralogy of the N4WS Deposit, Carajás Mineral Province, Pará, Brazil.

Elias Martins Guerra Prado[1,2], Adalene Moreira Silva[1], Diego Fernando Ducart[1], Catarina Labouré Bemfica Toledo[1], Luciano Mozer de Assis[3]

[1] Universidade de Brasília (UnB), Campus Darcy Ribeiro, Brasília, Brasil.

[2] Serviço Geológico do Brasil (CPRM), Residência Rondônia (REPO), Porto Velho, Brasil.

[3] Exploração Mineral de Ferrosos, Vale S.A, CTF - Miguelão, Fazenda Rio de Peixe, s/nº, Nova Lima-MG.

### Abstract

Quantifying the abundance and physicochemical properties of minerals using reflectance spectroradiometry in the visible, near infrared and shortwave infrared (400-2,500 nm) regions is an important tool in mineral exploration. In this study, the reflectance spectra of drill cores from the world-class N4WS iron deposit located in the Carajás Mineral Province, Brazil, were obtained. These spectra were validated using geochemical analysis by X-ray fluorescence (XRF) and thin sections. The reflectance spectra were collected using an FieldSpec 3 spectroradiometer (ASD, Boulder, Colorado, USA) in 9 drill cores. The mineralogy of the deposit is mainly hematite, with lesser amounts of magnetite, goethite, quartz, kaolinite, gibbsite, smectite, talc, carbonate and chlorite. The mineralogy of the iron deposit was extracted from the spectral data using the geometry (depth and wavelength) of the reflectance spectrum removed from the continuum. The depth of the absorption features is proportional to the mineral abundance, and the wavelength is proportional to the mineral chemical composition. The diagnostic absorption features of each mineral were used to determine the mineral abundance and composition. The final products include the abundance of iron (hydro) oxide (15.8% root-mean-square error [RMSE] Fe2O3); abundance of aluminous clays (RMSE 6% Al2O3); abundance of talc (8% RMSE MgO); identification of clay type (kaolinite, montmorillonite or gibbsite); composition of carbonate (dolomite vs. calcite); and composition of chlorite (Mg vs. Fe). The mineral abundance and composition results provided an effective characterisation of the ore, protore and host rocks and showed variations within the ore body.

**Keywords:** Carajás Mineral Province, reflectance spectroradiometry, iron ore.

## 4.1INTRODUCTION

Reflectance spectroradiometry is a well-known and effective technique for identifying the mineralogy of mineral deposits in the different stages of mineral exploration projects (Herrmann et al., 2001; Ducart et al., 2006; Silva et al., 2009; Harraden et al., 2013; Dalm et al., 2014). Spectral analysis of these deposits allows for a better understanding of the mineralised areas and can provide additional information on the spatial distribution of ore and contaminants.

In addition to mineralogical mapping, spectral analyses can quantify the identified minerals, which may be performed by correlating the spectral data with spectral libraries that include sample spectra of known mineralogical compositions or by correlating spectral data with independent data, such as X-ray fluorescence (XRF) (Clark and Roush, 1984; Cudahy et al., 2008; Haest et al., 2012).

Quantitative analyses of the mineralogy of a rock through reflectance spectroradiometry require the following assumptions: (1) measured electromagnetic energy travels the same distance during its trajectory from light source to sample and from sample to sensor (cf. Clark and Roush, 1984); (2) absorption intensity of a particular mineral in relation to the background (usually considered the continuum of the spectrum) is a function of the absorption coefficient and abundance of a mineral; thus, when the mineral is identified, its abundance may be determined by the absorption intensity (Hunt and Ashley, 1979; Clark and Roush, 1984); (3) chemical composition of a particular mineral determines the wavelength of its diagnostic absorption feature (cf. Hunt and Salisbury, 1971; Clark et al., 1990; Cudahy and Ramanaidou, 1997); and (4) scattering (crystal orientation, size/distribution/particle orientation) is isotropic (cf. Adams and Filice, 1967; Clark and Roush, 1984; Morris et al., 1985).

The main goal of this study is to develop the use of reflectance spectroradiometry to explore the N4WS iron deposit located in the Carajás Mineral Province, Pará, Brazil. For this purpose, a spectral study of nine drill holes distributed in 3 sections that cuts the N4WS deposit and integration of geological and geochemical data collected in the same range of the measurements were performed. The results were used to perform qualitative and quantitative modelling of the mineralogy of the deposit.

## 4.2 REGIONAL GEOLOGY

The Carajás Mineral Province is located in the oldest part of the Amazonian craton of Archean/Paleoproterozoic age (Gibbs, 1986; Machado et al., 1991). The region is dominated by metamorphosed volcano-sedimentary sequences and granitoids formed between 2.76 and 2.68 Ga as well as by the Pium and Xingu Mesoarchean complexes (Cordani et al., 1979; Santos, 2003; Santos et al., 2000, 2006; Tassinari, 1996; Tassinari et al., 2000; Tassinari and Macambira, 1999, 2004; Tassinari and Macambira, 1999). The province comprises the Mesoarchean granite-greenstone terranes of Rio Maria South Domain, and the Neoarchean volcano-sedimentary sequences and granitoids of Carajás North Domain (Tassinari et al., 1996; Bizzi et al., 2003).

The Carajás domain is bounded to the south by the granite-greenstone terranes of the Rio Maria domain and covered to the west by rocks of Mesoproterozoic age belonging to the Central Amazonian geological province, to the north by rocks of Paleoproterozoic age belonging to the Bacajá domain of the Transamazonian province and to the east by the Araguaia mobile belt of Neoproterozoic age (Bizzi et al., 2003).

The tonalite-trondhjemite-granodiorite (TTG) terranes of the Xingu complex (2.86 Ga; Silva et al., 1974) form the base of the volcano-sedimentary sequence represented by the Itacaiúnas Supergroup. Granites and mafic-ultramafic units with ages ranging from 2.76 to 2.74 Ga intrude these sequences (Figure 4.1).

The Serra dos Carajás is an S-shaped mountain range composed of metamorphosed volcano-sedimentary rocks of the Grão Pará group (2.7 Ga), including the Carajás Formation that consists of jaspillites , which host iron mineralisation (Figure 4.1).

The Parauapebas Formation constitutes the base of the Grão Pará Group and is represented by basalts, basaltic andesites and basic to intermediate pyroclastic rocks in smaller amounts (Krymsky, Macambira and Macambira, 2002; Lobato et al., 2005; Meirelles, Hirata, Amaral, Medeiros Filho and Gato, 1984), which occur concurrently beneath the Carajás Formation and reflect the contemporaneity of the two formations (Beisiegel et al., 1973; Macambira, 2003). These rocks are covered by banded iron formations (BIFs) and basic tuffs.

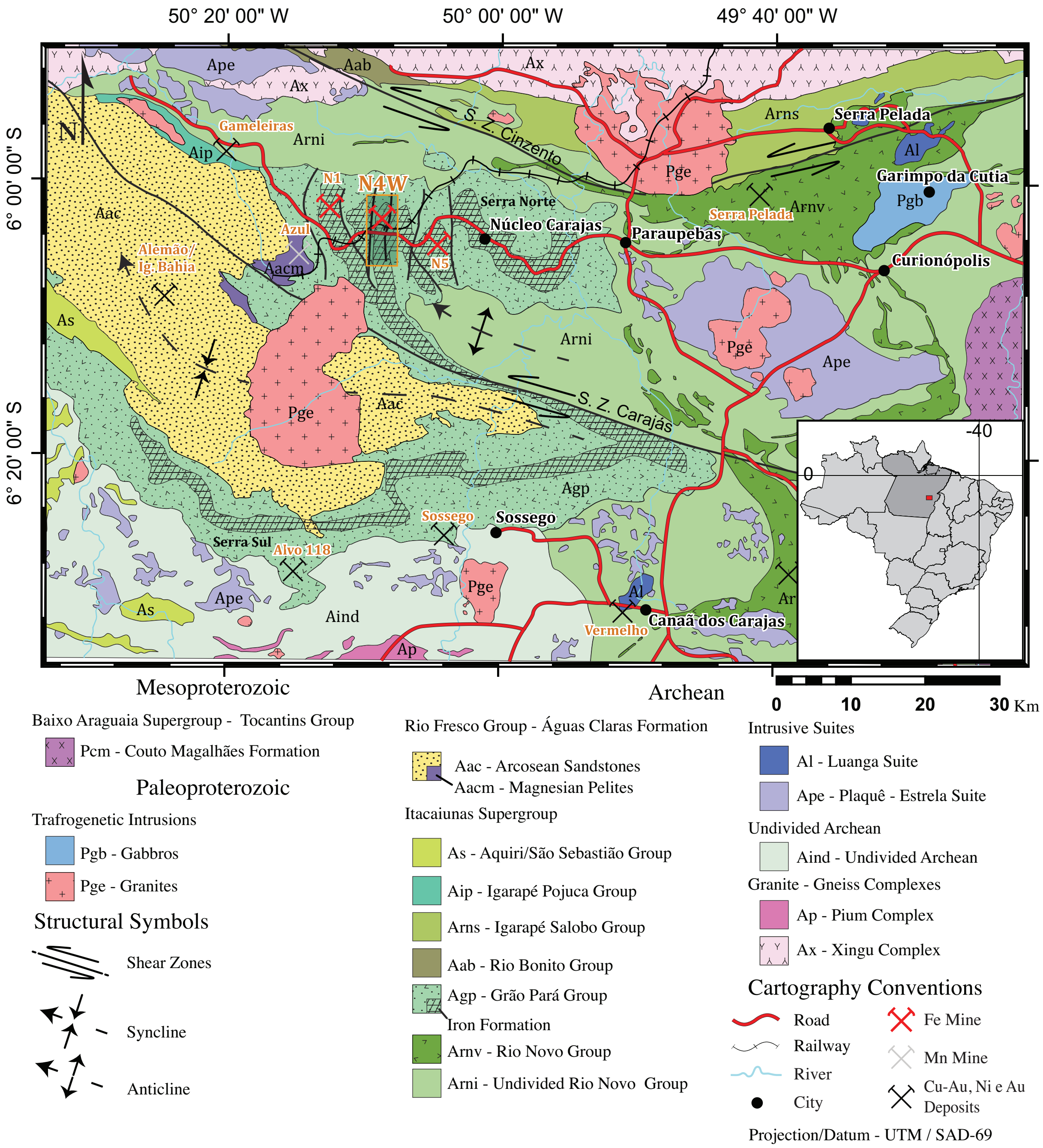

**Figure 4.1** Location map of the Carajás Mineral Province (Rosière et al., 2006) showing the major mineral resources, including the iron deposits N1, N4 and N5 (Serra Norte), Serra Sul and Serra Leste; IOCG deposits (Alemão/Igarapé Bahia, Sossego, Cristalino); Cu-Au (W-Bi-Sn) deposits, such as Gamelera and Alvo 118; gold-platinum-palladium deposit of Serra Pelada; Azul manganese deposit and Vermelho nickel deposit. Adapted from Silva and Hagemann (2013).

The Carajás Formation represents the intermediate portion of the Grão Pará Group (DOCEGEO, 1988) and contains layers and discontinuous lenses of Jaspilites and iron ore intruded by sills and mafic dikes. The Jaspilites have centimetre-thick intercalations of iron oxide, jasper and chert and are heavily weathered, with textures and primary structures preserved only at great depths. The texture of these rocks at depths show that the regional metamorphism weekly affect them. BIFs that include dolomite are also found (Dalstra and Guedes, 2004; Macambira and Schrank, 2002) and interpreted by Dalstra and Guedes (2004) as a carbonate facies of the BIF; however, a hydrothermal origin for this carbonate was suggested by Figueiredo and Silva et al. (2008).

The Igarapé Cigarra Formation is at the top of the Grão Pará Group and consists of mafic flows interlayered with tuffs followed by clastic sedimentary rocks, such as siltites, phyllites and greywackes (Gibbs et al., 1986; Macambira, 2003). The basalts with preserved igneous textures are the most common lithotypes (Macambira, 2003). Contact between this formation and the Carajás Formation is still uncertain, although it may be stratigraphic or structural, which calls into doubt their stratigraphic importance (Meirelles and Dardenne, 1991; Lindenmayer et al., 2001).

Psammo-pelitic rocks, such as arenites, calcarenites, siltites and conglomerates of the Águas Claras Formation, overlay the rocks of the Grão Pará Group (Figure 4.1). The ages obtained from mafic dikes that cut these sedimentary rocks indicate that the deposition of sediments occurred between 2.5 and 2.8 Ga (Mougeot, 1996).

Type-A alkaline to sub-alkaline granites of Paleoproterozoic age, such as the Serra dos Carajás granite, intrude the Itacaiúnas Supergroup and have been dated at 1880 ± 2 Ma (Machado et al., 1991; Figure 4.1). These granites are classified as oxidised magnetite-series rapakivi intrusions (Dall'Agnoll and de Oliveira, 2007).

The Serra dos Carajás is included in the Itacaiúnas Shear Belt (Araújo et al., 1988; Araújo and Maia, 1991). The main regional structures of this belt are oriented in E-W and WNW-ESE directions. The transpression-transtension model of Araújo et al. (1988) suggests that the sigmoidal structure of the Serra dos Carajás was formed during the dextral transtension of the basement rocks, which produced a pull-apart basin and the Carajás and Cinzento shear systems. A subsequent sinistral transpressive event caused the tectonic inversion of the basin and developed the positive flower structure of the

Carajás Shear System. The tectonic reactivation model proposed by Pinheiro and Holdsworth (1997) and Domingos (2009) suggests an intracratonic basin overlying the basement rocks, which were intensely deformed at 2.85 Ga under high-temperature conditions in a sinistral transpressive system. An important dextral transtensive brittle event between 2.8 and 2.7 Ga caused the accommodation of volcano-sedimentary rocks by tectonic subsidence and resulted in the sigmoidal shape of the Serra dos Carajás. The Carajás and Cinzento shear systems were formed during this event; however, various phases of dextral and sinistral reactivation have been proposed after 2.7 Ga (Pinheiro and Holdsworth, 1997; Domingos, 2009). The tectonic inversion of the basin began approximately 2.7 Ga and lasted until 2.6 Ga, and it involved a regional phase of sinistral transpression (Domingos, 2009). A late crustal extension phase at approximately 1.8 Ga allowed the placement of the Serra dos Carajás Intrusive Suite. Gibbs et al. (1986), Wirth et al. (1986), Docegeo (1988), Olszewski et al. (1989), and Tallarico (2003) proposed that the Carajás basin was established in a continental rift environment. Chemical and isotopic evidence show that the magmatism of the Itacaiúnas Supergroup was derived from the mantle and had significant continental crust contamination, thus supporting the model. Tallarico (2003) suggested that the rifting and volcanism were influenced by the mafic magmatism derived from a plume. In contrast, Dardenne et al. (1988) and Texeira (1994) suggested that the Carajás basin was formed in a volcanic arc environment because of the high-potassium calc-alkaline affinity of the basalts belonging to the Itacaiúnas Supergroup. Zucchetti (2007) considered that this geochemical signature may reflect volcanism under continental crust in a back arc environment.

The genesis of the iron ores of the Carajás Mineral Province as represented by the compact and friable hematite of the Carajás Formation is widely discussed in the literature, and three models have been proposed: supergene, hypogene and modified hypogene.

Tolbert et al. (1971) and Dardenne and Schobbenhaus (2001) proposed that the iron oxide enrichment of the ore bodies was residual and resulted from the supergene leaching of quartz and carbonate caused by meteoric waters during the lateritic alteration of the iron formations.

A different origins was proposed by Beisiegel et al. (1973), who suggested a hypogene model for the compact hematites, which indicated that hydrothermal fluids caused the metasomatic replacement of quartz. For the friable hematite, the authors proposed supergene enrichment. The role of hydrothermal fluids in iron mineralisation was also suggested by Dalstra and Guedes (2004), Rosière et al. (2004, 2005) and Lobato et al. (2005a, 2005b). For Rosière et al. (2004, 2005), structural control was observed in these mineralisations because fluid migration in these systems is controlled by areas of higher permeability, thus explaining the location of the ore bodies in the hinge zone of the Carajás synform.

The model advocated by Beisiegel et al. (1973) and Beukes et al. (2002) proposed that the genesis of the ore was associated with the supergene enrichment of areas previously altered by hypogene fluids, thus allowing the development of extensive layers of friable hematite in lateritic profiles that reach 500 m in depth. Tabular bodies of compact hematite occurred in association with friable ore and predominantly in the lower portion of the iron formation, whereas smaller lenticular bodies predominated at the top of the sequence.

## 4.3LITHOTYPES OF THE N4WS DEPOSIT

The plateaus where the iron formations occur were mapped in detail at a scale of 1:20,000. The mapping data are the product of the final reports of the research conducted by Tolbert et al. (1971) and Resende and Barbosa (1972) and update from Macambira (2003), which focused on the iron formations and their host rocks. Figure 4.2 shows the geological map of the N4WS deposit and is restricted to the plateau where the iron formations occur.

During the description of the cores and detailed mapping, which was performed by Vale S.A., 14 lithotypes were discriminated (Table 6-1: most common lithotypes in Serra Norte and their main characteristics (Assis, 2013)), and the following six were described in the drill cores analysed in this study.

Ore “canga” (OC): lateritic cover that forms in situ on the ore outcrops. The thickness can reach over 20 m, and it has high Fe content and relatively low contaminants, enabling their potential use as ore. This lithotype is an indicator of iron ore occurrences.

Chemical “canga” (CC): derived from the regolith of mafic rocks or associated with mature and cemented colluvial deposits; also known as barren lateritic cover.

Jaspilite (JP): banded iron formation that can be found with centimetre- to millimetre-thick laminations or an anastomosing pattern. Occasionally, the laminations alternate between mafic rock and jasper/chert. Breccias with jasper fragments encompassed by a magnetite-rich matrix also occur, commonly with veinlets of quartz and/or carbonate. Constant variation in size between magnetite and martite crystals. Represents the protore in the region and has Fe content ranging between 20-40%.

Friable Hematite (FH): iron ore with an average Fe content of 66%. Highly friable and porous Jaspilite structure partially to totally obliterated because of silica leaching. Colour varies from shades of grey to yellowish, which is associated with aluminium contamination.

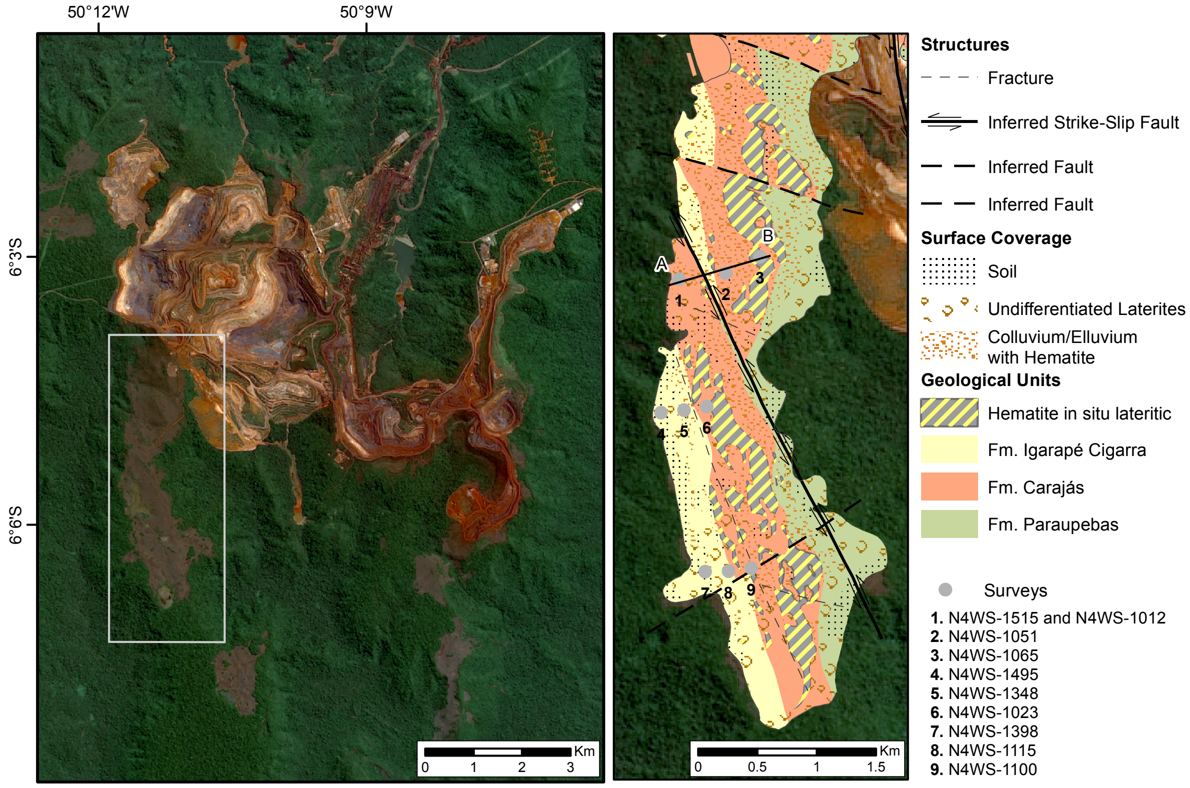

**Figure 4.2** Landsat 8 Operational Land Imager (OLI) sensor satellite image on the left showing the open pit of the N4 mine; the N4WS body is highlighted. On the right is the geological map of the N4WS body, focusing on the lithotypes described in the Serra Norte plateaus (Tolbert et al., 1971; Resende and Barbosa, 1972; Macambira, 2003). The studied drill holes are shown on the map and indicate the direction of the section.

Unweathered mafic (UM): basalts, gabbros and diabases that show little to no weathering. Tuffs of pyroclastic rocks are also described but rarer. Systematically chloritized with rich and restricted levels of talc. Green to dark green, sometimes with typical volcanic structures, such as tonsils filled with quartz, carbonates and chlorites and possibly sulphides. These lithotypes occur either as flows or intruded in JPs in the form of sills and dykes;

Semi-decomposed mafic (SDM): saprolite of mafic rocks with relicts of the original protolith framework or total loss of the original structure.

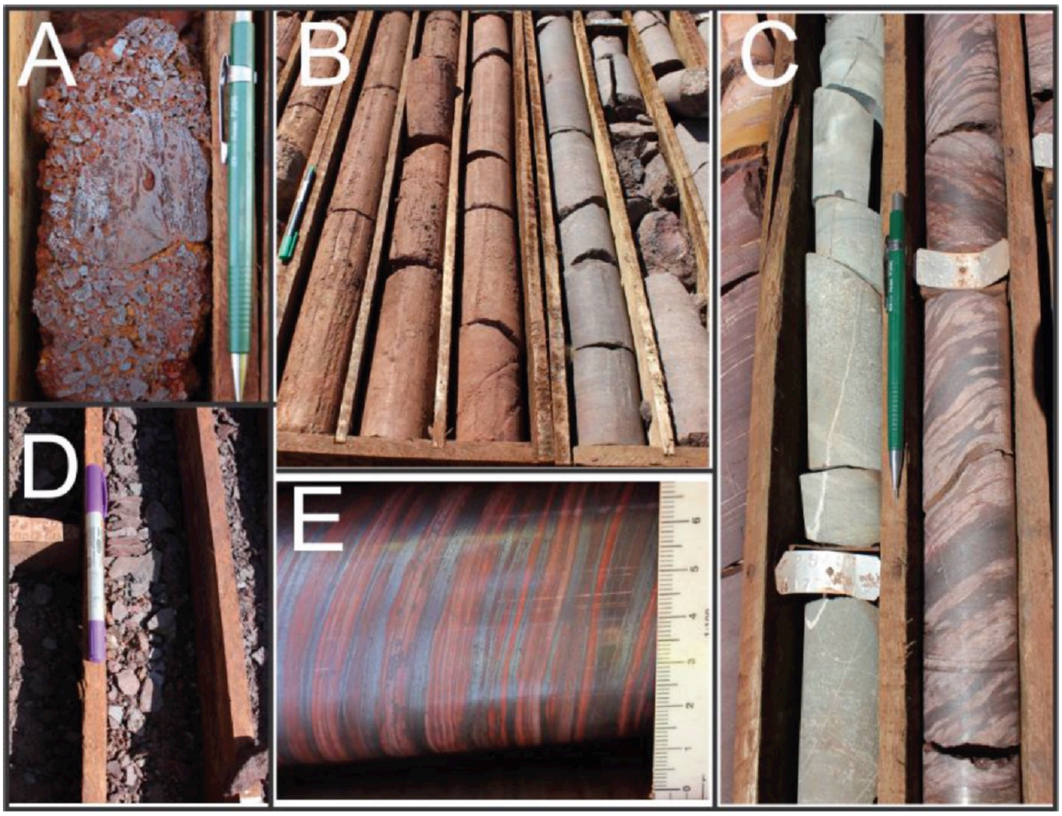

**Figure 4.3** Main lithotypes of the project area. A) Ore "canga" (OC). B) Chemical "canga" (CC) on the left and semi-decomposed mafic (SDM) on the right. C) Unweathered mafic (UM) on the left and jaspilite (JP) on the right. D) Friable hematite (FH). E) Details of the jaspilite (JP) banding showing intercalation of iron oxide and jasper bands.

## 4.4METHODOLOGY

### *Sampling and data collection*

The samples were collected from cores of nine drill holes distributed in three sections that cut in EW direction the N4WS deposit. Representative samples of 15 cm long were collected every 2 m (1766 samples), and half of each sample was separated for geochemical analysis (XRF). Certain samples were selected to produce six polished thin sections to validate the minerals identified by spectral analysis. Magnetic susceptibility data obtained by Ferreira et al. (2014) were incorporated in this study for comparing the results.

The reflectance spectrum of the samples was measured using the FieldSpec3 Hi-Res® (ASD Inc., Boulder, Colorado, USA; 5111 measurements) reflectance spectroradiometer.

The measurements were performed using a contact probe with halogen lamp as an internal light source. The acquisition window of the contact probe has an area of 1 cm2, and the saved spectrum is the mean of 75 spectra collected in the same area.

The device collects the spectra in three modules: one that covers wavelengths from visible to near-infrared (VNIR: 350-1000 nm) and two that cover the short-wave infrared (SWIR: 1000-2500 nm). The sampling interval of the spectrometer is 1.4 nm in the VNIR and 2.0 nm in the SWIR, with a wavelength accuracy of ± 0.5 nm. The spectral resolution is 3 nm in the VNIR and 8 nm in the SWIR. The spectra collected by the spectralradiometer are converted from radiation to reflectance using the signal from a SpectralonTM plate. The device calibration was performed every 20 minutes during data collection.

The quantitative analysis of spectral data is a technique that has been utilized for a number of years. However, because of the variety of sensors available for data collection, there is no standard methodology for this type of analysis. In general, studies using the technique to quantify the mineralogy of soils obtain spectra with diffuse reflectance spectrometers (Fernandes et al., 2004; Carioca et al., 2011 Gonçalves et al., 2012). In studies where the technique is used to quantify the mineralogy of rock samples, the spectra are usually obtained by portable reflectance spectrometers (e.g., ASD, PIMA; Yang et al., 2011; Sonntag et al., 2012), spectrometers mounted on robotic systems (e.g., HyLogger System; Haest et al., 2012), or by hyperspectral drill core scanners (Ross et al., 2013). This study used a portable reflectance spectroradiometer (ASD FieldSpec) that includes two sensors for data collection: pistol grip or contact probe. The pistol grip requires an external light source for data collection; thus, the positioning configuration (distance, slope and height) of the pistol grip (sensor), light source and sample should be set for the specific measurements to be performed. The contact probe has internal illumination, and the data are collected with the probe in direct contact with the sample. The quantitative analyses of spectral data obtained by spectrometers such as this can be performed using both sensors (pistol grip or contact probe); however, studies have not indicated the best sensor for this type of analysis.

The data collection methodology was developed from experiments to determine the sensor (pistol grip or contact probe) that has the greater accuracy and precision. For this purpose, the spectrum of a sample obtained by different methods of acquisition was analysed using the pistol grip and contact probe.

The results of these experiments showed that the contact probe is the most suitable sensor for this study. The absence of noise at wavelengths that indicate the diagnostic features of certain minerals and reproducibility of spectral parameters increase the accuracy and precision of the contact probe relative to that of the pistol grip. The fixed geometry of the illumination angle and sensor within the contact probe and ease of setting a fixed distance between the light source, sample and sensor increase the accuracy and precision of the contact probe relative to that of the pistol grip.

### Analysis of spectral data

When light interacts with a mineral or rock, it is preferably absorbed at certain wavelengths, whereas it is transmitted and reflected at other wavelengths. Reflectance is defined as the ratio between the intensity of the light reflected by the sample and intensity of the incident light (Van der Meer, 2004). Electronic transition and charge transfer processes (e.g., change in the electronic state of electrons bound to atoms or molecules) associated with transition metal ions such as Fe, Ti, Cr, etc. determine the position of the diagnostic spectral absorption features of certain minerals in the VNIR and SWIR regions to a large extent (Hunt, 1977; Burns, 1993; Adams, 1974, 1975). Vibration processes related to H2O and OH- also produce characteristic absorption features in the SWIR region (Hunt, 1977).

The position, shape and depth of these absorption features are controlled by the crystal structure of the atoms and absorbent molecules and chemical structure of the material. Therefore, variables that characterise these absorption features (spectral parameters) can be directly correlated to the chemical composition and crystal structure of the sample (Van der Meer, 2004). The spectral parameters are obtained from the polynomial curve that best fits the reflectance spectrum removed from the continuum, which is the total albedo of the reflectance curve (Figure 4.4). Mathematically, the spectrum removed from the continuum is obtained by the following equation (Clark et al., 2003):

$$L_c(w) = \frac{L(w)}{C_1(w)}$$

where L(w) is the spectrum obtained as a function of the wavelength, C1(w) is the continuum of the obtained spectrum and Lc(w) is the spectrum removed from the continuum.

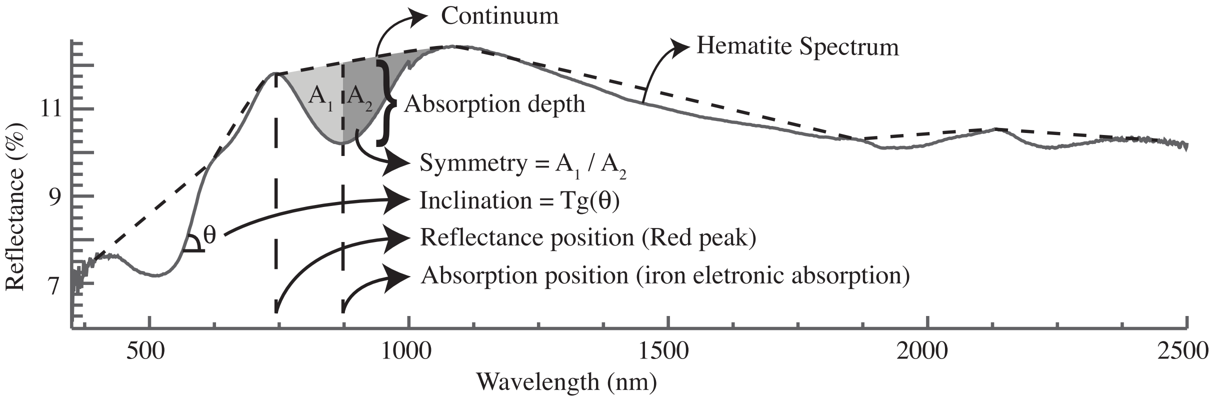

**Figure 4.4** Spectral parameters obtained from the mean spectra of each sampling method developed in this study.

The position of the absorption feature is defined as the wavelength at which the absorption feature reaches the reflectance minimum of the curve, and the position of a reflectance feature is defined as the wavelength at which the feature reaches the reflectance maximum of the curve. The depth of the absorption feature was calculated using the method of Clark and Roush (1984) by subtracting the minimum reflectance value of the polynomial curve by the reflectance value of the continuum at the same wavelength and then dividing this value by the reflectance of the continuum. When the absorption feature is not present in the analysed spectrum, the depth value is equal or close to zero, indicating the absence of the investigated mineral. The asymmetry factor of the feature is defined by Van der Meer (2004) as the ratio of the areas on the right and left of the wavelength of minimum reflectance. The slope of a given region of the spectrum is calculated by obtaining the slope of the line tangent to this region (Figure 4.4).

Data were analysed using the commercial software "The Spectral Geologist" (TSG CoreTM, version 7.1.0.062, CSIRO Earth Science and Resource Engineering (CESRE)

Division, Sydney, Australia), which was used to process the spectral reflectance data, obtain the spectral parameters and extract the mineral abundance, composition and crystallinity data. First, the spectral parameters of individual absorption features, such as the depth, wavelength or ratio between spectral bands (Table 4.1), were calculated and then integrated to generate the abundance, composition and crystallinity data of the minerals (Table 4.2). In addition to the spectral parameters developed in this study, certain parameters were based on those proposed by Haest et al. (2012) and adapted to the project.

Iron oxides produce characteristic absorption features in the VNIR (Hunt and Ashley, 1979; Morris et al., 1985; Sherman and Waite, 1985; Cudahy and Ramanaidou, 1992, 1997). These absorption features are caused by electronic processes involving Fe3+ bonded to an octahedral site by oxygen ligands (hematite) or oxygen and hydroxyl ligands (goethite). Electronic processes include the (1) transition of electrons to an upper energy level within unfilled orbitals (crystal field absorption), (2) transfer of charge between metals and ligands (charge transfer absorption), and (3) transitions resulting from the interaction between adjacent Fe2+ cations (Sherman and Waite, 1985). Goethite and hematite have characteristic crystal field absorptions between 630-715 nm and 850-1000 nm and an absorption feature caused by charge transfers between 480 and 550 nm (Figure 4.5; Curtiss, 1985; Morris et al., 1985). Hunt and Ashley (1979) observed that the abundance of iron (hydro-)oxides is related to the depth of the absorption generated by the crystal field between 850 and 1000 nm, which was confirmed by Cudahy and Ramanaidou (1992). Haest et al. (2012) observed that the

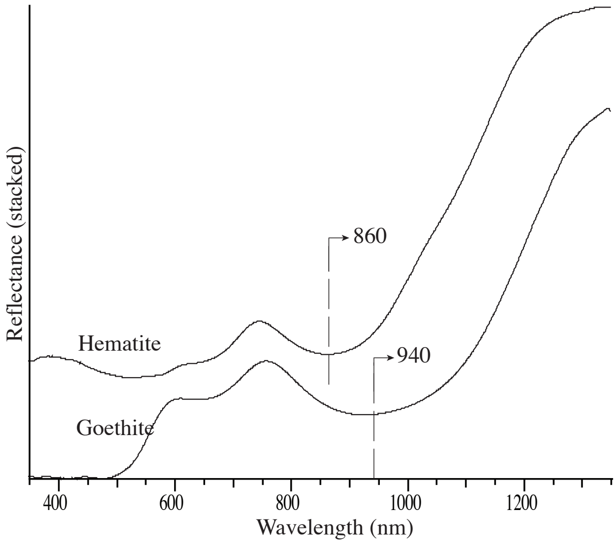

**Figure 4.5** Reflectance spectra of hematite and goethite; the position of the absorption feature of these minerals is highlighted.

depth of this absorption feature is influenced by the albedo of the sample; thus, two samples with the same amount of iron may have different depths of absorption if one is darker than the other.

The identification of iron (hydro-)oxide in the spectrum was performed using the slope of the spectral curve from 600-740 nm (600_740SL, Table 4.1). The iron (hydro-)oxide has a positive slope in this region of the spectrum because of absorption of crystal field from 630-715 nm (Figure 4.5). The depth of the absorption feature from 850-1000 nm was calculated for the samples with the index 600_740SL>0, and it was based on a fifth-degree polynomial and fitted to the continuum removed spectrum from 750-1250 nm and had a focus ranging between 800-1020 nm (900D, Table 4.1 and Table 4.2). To address the influence of albedo, a spectral index was created based on the mean reflectance at 1650 ± 100 nm (N1650R, Table 4.1; Haest et al., 2012).

The position of the absorption feature from 850-1000 nm in the iron (hydro-)oxides is a function of its composition (Figure 4.5; Townsend, 1987; Ramanaidou, 1997). Townsend (1987) observed that the position of the feature varies from ~860 nm for pure hematite samples to ~920 nm for pure goethite samples. The wavelength of the feature position was calculated from a fourth-degree polynomial and fitted to the continuum removed reflectance spectrum from 750-1050 nm, and it had a focus ranging between 800-1020 nm (900Wvl, Table 4.1 and Table 4.2).

Hunt and Salisbury (1970) observed that a broad absorption feature centred at 1100 nm has a depth proportional to the Fe2+ content. The abundance of Fe2+ was obtained from the slope of the spectral curve between 1350 and 1650 nm (1500SL, Table 4.1).

Phyllosilicates and carbonates have characteristic absorption features in the SWIR region related to bonds between H2O molecules, metal-OH and CO32-. In this study, absorption features related to Al-OH bonds, which occur in the kaolin-group minerals, smectite and gibbsite, Mg-OH bonds, which occur in chlorites and talc, and CO3, which occurs in carbonates, were used to extract estimates of the relative mineral abundance and composition.

The minerals containing Al-OH in their structure have characteristic absorption features ranging between 2185 and 2210 nm (Clark et al., 1990). The depth of these absorption features was used in this study to determine the abundance of these minerals. The various minerals that have Al-OH in their structure were differentiated by the presence or absence of characteristic absorption features between 2160 and 2350 nm, and three parameters were observed: abundance of kaolinite, abundance of smectite, and abundance of gibbsite (Table 4.2). The abundance of a specific aluminous phyllosilicate in samples with a mixture of aluminous phyllosilicates cannot be obtained with this method, which only provides the abundance of the "spectrally" dominant phyllosilicate.

Kaolin-group minerals have a dominant absorption feature set at 2208 ± 3 nm that is produced by Al-OH bonds (Figure 4.6; Crowley and Vergo, 1988; Clark et al., 1990; Cudahy, 1997; Bishop et al., 2008). All kaolin-group minerals are characterised by additional absorption features between 2160 and 2190 nm, which are also produced by Al-OH bonds (Clark et al., 1990; Cudahy, 1997). The distinction between the various minerals of this group is based on the position and depth of these additional absorption features. Kaolinite has an absorption feature near 2160 nm (Clark et al., 1990; Cudahy, 1997) that is more pronounced in kaolinites with increased crystallinity (structural order; Figure 4.6). A ratio of four bands was used to test the intensity of the absorption feature from 2160 to 2180 nm and differentiate the kaolin-group minerals from other aluminous phyllosilicates (Cudahy et al., 2008; 2160D2190, Table 4.1) using the condition 2160D2190 > 0.001. The degree of crystallinity of the kaolinite was obtained from the ratio of the reflectance at 2180 nm and 2166 nm plus the depth of the absorption feature at 2208 nm (2170SL, Table 4.1 and Table 4.2; Senna et al., 2008). The abundance of kaolinite was obtained from the calculation of the depth of the absorption feature at 2208 nm using a twelfth-degree polynomial fitted to the continuum removed spectrum between 2130 and 2245 nm, with the focus ranging between 2200 and 2215 nm (2200Dk, Table 4.1 and Table 4.2; Haest et al., 2011).

**Table 4.1** Algorithms for the extraction of spectral data (band ratio, absorption depth, minimum absorption wavelength, etc.) of individual absorption features (Modified from Haest et al., 2012).

| Parameter | Function | TSG Core Algorithm |
|---|---|---|
| 600_700SL | Identify Fe (hydro-)oxides | PFIT: Continuum slope ranging between 600-740 nm |
| 900D | Identify and quantify Fe (hydro-)oxides | PFIT: Depth of the continuum removed spectrum calculated using a fifth-degree polynomial from 750-1250 nm, with a focus ranging between 800-1020 nm |
| 900Wvl | Differentiate hematite-goethite | PFIT: Wavelength of the continuum removed spectrum calculated using a fourth-degree polynomial from 750-1050 nm, with a focus ranging between 800-1020 nm |
| N1650R | Albedo | PROFILE: Mean reflectance at 1650 ±100 nm |
| 2160D2190 | Differentiate kaolin-group minerals from other Al phyllosilicates (e.g., aluminous smectite) | ARITH: (R2136+R2188)/(R2241+R2171) |
| $2200D_K$ | Identify and quantify kaolinite | PFIT: Depth of the continuum removed spectrum calculated using a twelfth-degree polynomial from 2230-2245 nm, with a focus ranging between 2200-2215 nm |
| 2170SL | Kaolinite crystallinity index | ARITH: R2180/R2166 |
| $2200D_S$ | Identify and quantify smectite | PFIT: Depth of the continuum removed spectrum calculated using a tenth-degree polynomial from 2150-2267 nm, with a focus ranging between 2193-2225 nm |
| 2260D | Identify and quantify gibbsite | PFIT: Depth of the continuum removed spectrum calculated using a twelfth-degree polynomial from 2115-2475 nm, with a focus ranging between 2235-2300 nm |
| 1450D | Identify gibbsite | PFIT: Depth of the continuum removed spectrum calculated using a twelfth-degree polynomial from 1350-1710 nm, with a focus ranging between 1430-1467 nm |
| 1400D | Identify talc | PFIT: Depth of the continuum removed spectrum calculated using an eighth-degree polynomial from 1380-1460 nm, with a focus ranging between 1390-1420 nm |
| 2380D | Identify talc | ARITH: (R2365+R2415)/(R2381+R2390) |
| 2310D | Identify and quantify talc | PFIT: Depth of the continuum removed spectrum calculated using a twelfth-degree polynomial from 2242-2342 nm, with a focus ranging between 2305-2320 nm |
| 1500SL | Identify $Fe^{2+}$ | ARITH: (R1650/R1350) |
| 2250D | Identify chlorite | ARITH: (R2227+R2275)/R2241+R2259) |
| 2335D | Identify and quantify chlorite | PFIT: Depth of the continuum removed spectrum calculated using a twelfth-degree polynomial from 2171-2439 nm, with a focus ranging between 2300-2379 nm |
| 2335Wvl | Chlorite composition | PFIT: Wavelength of the continuum removed spectrum calculated using a tenth-order polynomial from 2272-2381 nm, with a focus ranging between 2310-2370 nm |
| 2330D | Identify and kaolify carbonates | PFIT: Depth of the continuum removed spectrum calculated using a tenth-order polynomial from 2250-2360 nm, with focus ranging between 2310-2345 nm |
| 2330De | Identify carbonates | ARITH: (R2265+R2349)/(R2316+R2333) |
| 2330Wvl | Carbonate composition | PFIT: Wavelength of the continuum removed spectrum calculated using a tenth-order polynomial from 2300-2360 nm |
| 2330Asym | Identify carbonates | PFIT: Simetry of the continuum removed spectrum calculated using a eight-order polynomial from 2120-2370 nm, with focus ranging between 2235-2370 nm |

**Table 4.2** Spectral products applied in this study to extract the mineral abundance and compositional data of the N4WS drill cores.

| Name | Detected minerals | Base algorithm | Filters/Masks | Correlation trend | Accuracy |
|---|---|---|---|---|---|
| Abundance of Fe (hydro-)oxides (Fe-$ox_{ab}$) | Hematite, goethite | 900D converted according to N1650R (900D/N1650R) | 900D ≥ 0.025<br>600_740SL > 0 | %Fe total = $-6.5637 * (Fe\text{-}ox_{ab})^2 + 46.573 * (Fe\text{-}ox_{ab}) + 18.35$ | 15.8% Fe total |
| Hematite-goethite distribution | Hematite/goethite ratio | 900Wvl | 600_740SL > 0 | | |
| Abundance of kaolinite | Kaolinite | $2200D_K$ | $2200D_K \geq 0.02$<br>2160D2190 > 0.001 | $\%Al_2O_3 = 69.543 * (2200D_K) + 9.8152$ | 6% $Al_2O_3$ |
| Crystallinity of kaolinite | Kaolinite | 2170SL | $2200D_K \geq 0.02$<br>2160D2190 > 0.001 | | |
| Abundance of Al-smectite | Al-smectite | $2200D_S$ | $2200D_S \geq 0.006$<br>2160D2190 < 0.001<br>1400D > 0.0039 | | |
| Abundance of gibbsite (gib_abun) | Gibbsite | 2260D | 2260D > 0.009<br>1450 > 0.011 | $\%Al_2O_3 = 139.67 * (2260D) + 7.1136$ | 10% $Al_2O_3$ |
| Abundance of talc | Talc | 2310D | 2310D > 0.02<br>1400D > 0.0039<br>2380D > 1 | %MgO = 24.354 * (2310D) + 3.7029 | 8% MgO |
| Abundance of chlorite | Chlorite | 2335D | 2335D > 0.02<br>gib_abun = 0<br>2250D > 1 | | |
| Composition of chlorite | Chlorite | 2335Wvl | 2335D > 0.02<br>gib_abun = 0<br>2250D > 1 | | |
| Abundance of carbonate | Calcite, dolomite | 2330D | 2330D ≥ 0.007<br>2330De > 1.003<br>2330Asym > 1.11<br>2250D < 1.004<br>2380D < 1 | %MgO + %CaO = 74.948 * (2330D) + 1.6862 | 7% (MgO + CaO) |
| Composition of carbonate | Calcite, dolomite | 2330Wvl | 2330D ≥ 0.007<br>2330De > 1.003<br>2330Asym > 1.11<br>2250D < 1.004<br>2380D < 1 | | |

The aluminous smectites do not have the additional absorption features between 2160 and 2190 nm that occur in the kaolinite-group minerals (Figure 4.6; Clark et al., 1990), and they typically contain structural water (deep and asymmetric sharp absorption at 1910 nm). Aluminous smectite and kaolinite-group minerals were distinguished using the following condition: 2160D2190 < 0.001 (Table 4.1). To obtain the abundance of aluminous smectite, the depth of the absorption feature at 2208 nm, which is also present in kaolinite, was calculated. The absorption feature was calculated using a tenth-degree polynomial fitted to the spectral curve removed from the continuum between 2150 and 2267 nm, with a focus between 2193 and 2225 nm (2200Ds, Table 4.1 and Table 4.2).

Gibbsite has a strong characteristic absorption feature near 2268 nm and three less prominent absorption features at 1452, 1521 and 1549 nm (Figure 4.6; Clark et al., 1990). The abundance of gibbsite was obtained from the calculation of the depth of the absorption feature at 2268 nm using a twelfth-degree polynomial fitted to the continuum removed spectrum between 2115 and 2475 nm, with the focus between 2235 and 2300 nm (2260D, Table 4.1 and Table 4.2). The gibbsite was identified using the following condition: 1450D>0.011 and 2260D>0.009.

The Mg-OH bonds present in talc produce a characteristic absorption feature near 2310 nm and 2380 nm and a minor absorption feature at 2290 nm (Figure 4.6; Clark et al., 1990). In addition to these features, talc has the hydroxyl absorption feature at 1400 nm, which is also present in the other phyllosilicates. The abundance of talc was obtained from the depth of the absorption feature at 2310 nm calculated using a twelfth-degree polynomial fitted to the continuum removed spectrum from 2242-2342 nm, with a focus ranging between 2305-2320 nm (2310D, Table 4.1 and Table 4.2). To obtain this parameter, the algorithm used the depth of the features at 2380 and 1400 nm (2380D, 1400D, Table 4.1) to distinguish talc from carbonates and chlorite (Figure 4.6). These minerals also absorb near 2310 nm. The conditions were 2380D > 1 and 1400D > 0.0039.

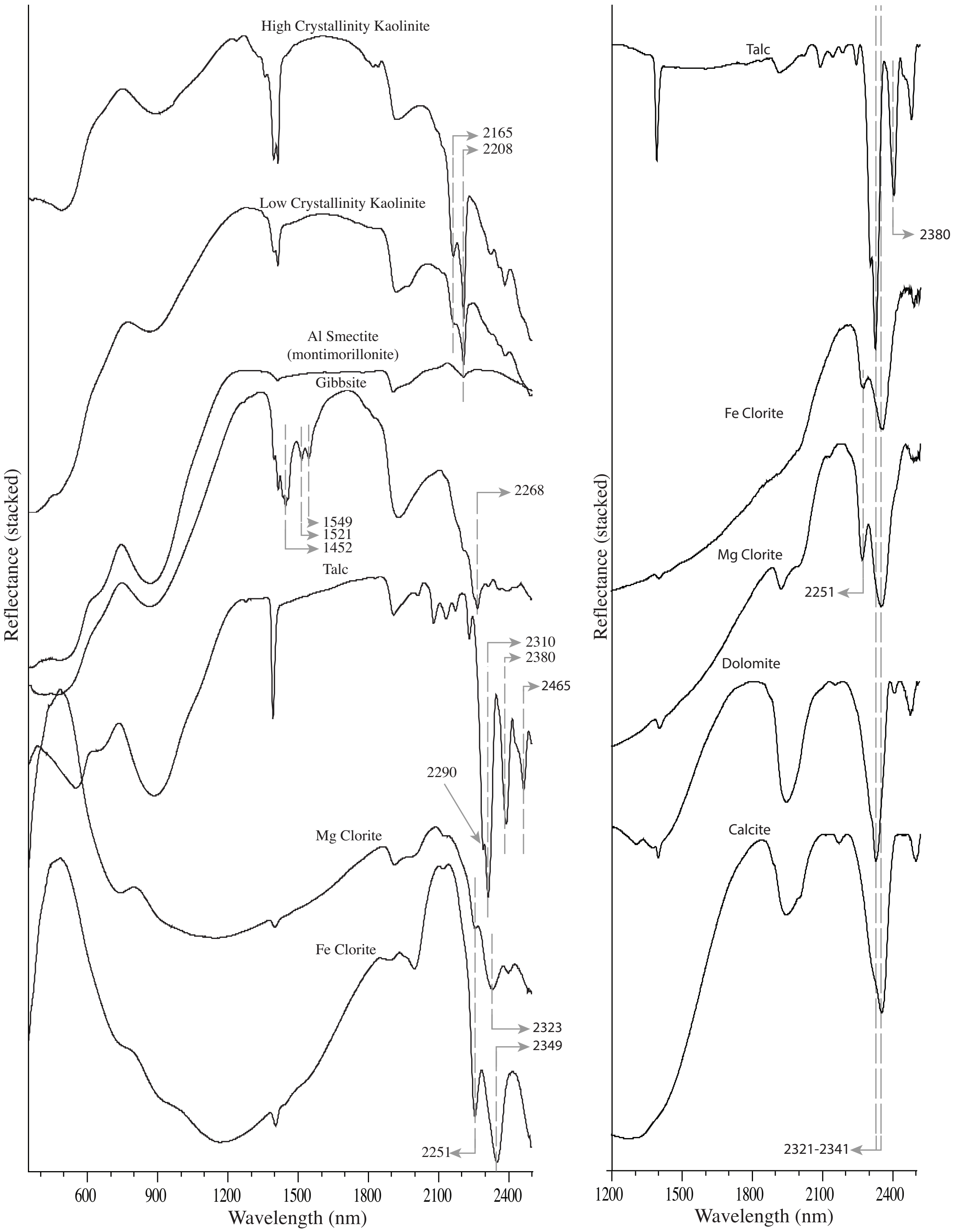

**Figure 4.6** Stacked reflectance spectra of the samples containing iron (hydro-)oxides, phyllosilicates and carbonate of the N4WS deposit, including kaolinite (F1495/014, F1012/130), Al smectite (F1115/025), gibbsite (F1515/22), talc (F1515/194), chlorite (F1115/092, F1398/144), dolomite (F1515/231) and calcite (F1398/090). All samples contain iron (hydro-)oxides. The main absorption features of these minerals are highlighted.

Chlorite has two characteristic absorption features, with one from 2240-2256 nm and the other from 2320-2360 nm, related to Fe-OH and Mg-OH bonds, respectively (Hunt and Salisbury, 1970). The absorption associated with Fe-OH bonds (near ~2251 nm) distinguishes chlorite from talc and carbonates. These minerals also contain Mg-OH and absorb at wavelengths near the main absorption feature of chlorite located from 2320-2350 nm (Figure 4.6; Gaffey, 1986; Clark et al., 1990). The position of this absorption feature varies with the composition, ranging from 2320 nm for magnesian chlorites to 2350 nm for ferrous chlorites (Hunt and Salisbury, 1970). The abundance of chlorite was obtained by calculating the depth using a twelfth-degree polynomial fitted to the continuum removed spectrum from 2171-2439 nm, with a focus ranging between 2300-2379 nm (2335D, Table 4.1 and Table 4.2). The composition of the chlorite was calculated using a twelfth-degree polynomial fitted to the continuum removed spectrum from 2272-2381 nm, with a focus ranging between 2310-2370 nm (2335Wvl, Table 4.1 and Table 4.2). The algorithm used to obtain these parameters employed the depth of the absorption feature at 2351 nm (2350D, Table 4.1) to distinguish chlorite from talc and carbonates. Additionally, the algorithm did not accept mixtures with gibbsite because this mineral has similar absorption features to chlorite. Thus, the conditions necessary to execute the algorithm were 2350D > 1 and abundance of gibbsite = 0.

The vibrations of CO32- ions produce strong absorption features from 2500-2550 nm and 2300-2350 nm and minor absorption features from 2120-2160 nm, 1970-2000 nm and 1850-1870 nm (Figure 4.6; Gaffey, 1986; Clark et al., 1990). The position of these features varies with the composition, ranging from ~2315 nm for dolomite to ~2350 nm for calcite (Gaffey, 1986). The abundance of carbonates in the samples was assessed from the depth of a tenth-degree polynomial fitted to the continuum removed spectrum from 2250-2360 nm, with a focus ranging between 2310-2345 nm (2330D, Table 4.1 and Table 4.2). The composition of carbonates was calculated from a tenth-degree polynomial fitted to the continuum removed spectrum from 2250-2360 nm, with a focus ranging between 2310-2345 nm (2330Wvl, Table 4.1 and Table 4.2). Both the abundance and composition of carbonates were calculated only for samples that had no chlorite and/or talc. These minerals also absorb from 2300-2350 nm, the same region of the main absorption feature of carbonates used for calculations; however, they also have other diagnostic absorption features (Clark et al., 1990; Post and Noble, 1993; Bishop et al., 2008). Chlorite, for example, has a diagnostic absorption feature at ~2255 nm, which is identified by the parameter 2250D (Table 4.1). Talc has an extra absorption feature at ~2380 nm, which is identified by the parameter 2380D (Table 4.1). Therefore, the conditions to calculate the spectral parameters of the carbonates were 2380D < 1 and 2250D < 1.004. In addition to these conditions, the strong asymmetry and the minimum depth of the 2330 nm feature were also considered (2330Asym > 1.11 and 2330D > 1.003, Table 4.2).

## 4.5VALIDATION AND ANALYSIS OF SPECTRAL DATA

### *Abundance of iron (hydro-)oxides*

The iron (hydro-)oxide abundance algorithm (900D, Table 4.1) was compared to the %Fe2O3 from the XRF analyses of the drill cores. The depth of the absorption feature at ~900 nm (900D, Table 4.1) obtained by the algorithm was significantly correlated with the XRF data despite the large observed scattering (Figure 4.7A; 3598 samples). To better understand the data distribution, the samples in Figure 4.7A were plotted on a colour palette according to the albedo (N1650R). The graph shows that the albedo is directly proportional to the depth of the 900D feature for a given %Fe2O3. However, the depth of the 900 nm absorption feature should be constant for samples with the same %Fe2O3. Haest et al. (2012) observed that the depth of the ~900 nm absorption feature is correlated to the albedo and results in abundance values that were underestimated in darker samples and overestimated in lighter samples. This result can be explained by a combination of the grain size variation and effect of opaque minerals reducing the length of the actual path taken by electromagnetic energy and decreasing the interaction/absorption of specific minerals (Clark and Roush, 1984). Consequently, coarse-grained iron (hydro-)oxides have lower albedo, but this change in albedo is more pronounced in the SWIR region because of the trans-opaque behaviour of the iron (hydro-)oxides resulting in a substantial reduction in reflectance at ~1650 nm and lower reduction in the reflectance at ~900 nm (Haest et al., 2012).

The effect of the sample albedo on the calculation of the absorption feature depth can be reduced by applying a transformation. In this case, the iron oxide (900D) abundance algorithm was transformed as a function of the N1650R parameter using the following ratio: 900D/N1650R (Table 4.2). The new algorithm for iron (hydro-)oxide abundance was better correlated with the %$Fe_2O_3$ of the XRF, and a second-order polynomial was used for the correlation (Figure 4.7A B; 3598 samples), which had a root-mean-square error (RMSE) of 15.8% $Fe_2O_3$.

To understand the spectral behaviour of the different analysed rocks, the samples in Figure 4.7B were plotted according to the type of rock (jaspilite, hematite, basalt, etc.). The colour for each lithotype matches the same pattern used in the geological description in several studies performed in Carajás to facilitate data integration. The graph shows that the different lithotypes were grouped into three domains. B has a lower percentage of $Fe_2O_3$ (4-35%) and exhibited albedo-corrected 900D parameter values ranging from 0 to 0.6. JP has an intermediate $Fe_2O_3$ percentage (40 to 65%) and exhibited albedo-corrected 900D parameter values ranging from 0.6 to 1.4. FH has a high content of ore in the deposit, high percentage of $Fe_2O_3$ (>90%) and abundance of iron (hydro-)oxide and exhibited albedo-corrected 900D parameter values greater than 1.4. Thus, in addition to providing an estimate of the $Fe_2O_3$ content in the sample, the spectral analysis can differentiate among the ore in the other rocks of the deposit.

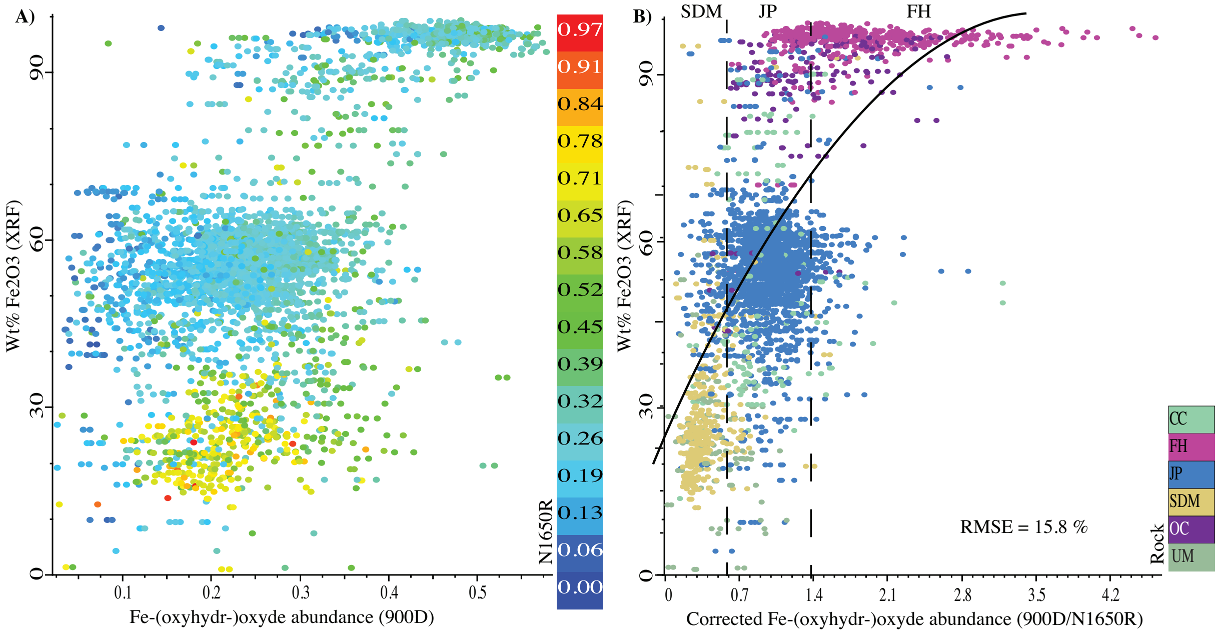

**Figure 4.7** A) Correlation between the iron (hydro-)oxide (900D) abundance algorithm and % Fe of the XRF analyses. B) Correlation between the iron (hydro-)oxide abundance algorithm transformed as a function of the albedo (900D/N1650R) and % Fe2O3 of the XRF analyses; the regression curve is shown. Number of samples: 3598. In A), the samples are coloured according to the mean reflectance from 1550-1750 nm (N1650R), and in B), they are coloured according to the type of rock. CC: chemical canga; FH: friable hematite; JP: jaspilite; SDM: semi-decomposed mafic; OC: ore canga; SM: Ultramafic rock.

### *Composition of the iron (hydro-)oxides (hematite-goethite)*

The accuracy of the algorithm that determines the hematite-goethite distribution (Table 4.2) was validated using the loss on ignition (LOI) data of the samples (goethite dehydrates to hematite at 1000°C; Strezov et al., 2010).

Because the LOI measured for heating to 1000°C is affected by a number of minerals (goethite, Al-OH clays and organic and inorganic carbon (carbonates)), only the samples with low Al2O3, CaO and MgO content and high Fe2O3 (CaO<1%, MgO<1%, Al2O3<2.5% and Fe2O3>55%) content were used to validate the goethite-hematite distribution algorithm. These samples showed a significant correlation between the values of the algorithm and LOI results, although with clustering of the samples near the hematite wavelengths (Figure 4.8; 1285 samples). The goethite samples showed high LOI values (~8%) and long wavelengths of the absorption feature at ~900 nm (~900 nm), whereas the samples richest in hematite showed low LOI values (~2%) and short wavelengths of the absorption feature at ~900 nm (~887nm). The samples clearly showed the predominance of hematite in the N4WS deposit.

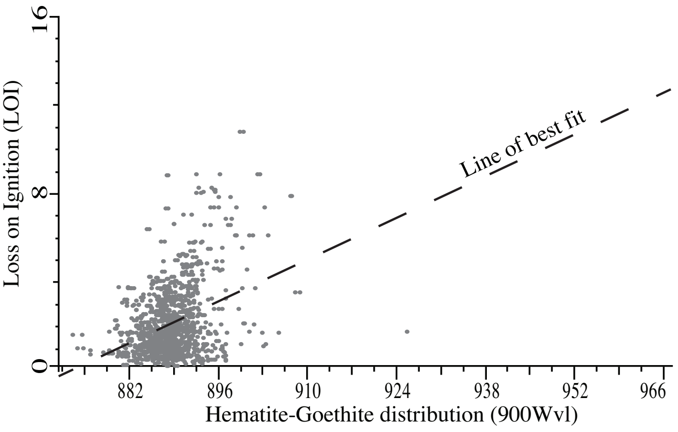

**Figure 4.8** Correlation between the distribution of goethite-hematite (900Wvl) and loss on ignition (LOI) at 1000°C for samples with XRF analyses falling within the following limits: CaO < 1%, MgO < 1%, Al2O3 < 2.5% and Fe > 55%. Number of samples: 1285.

*Abundance of aluminous clays*

The accuracy of the 2200DK and 2260D algorithms (Table 4.1) in measuring the amount of kaolinite and gibbsite, respectively, was evaluated using the percentage of Al2O3 of the XRF analyses of the drill cores.

The 2200DK spectral parameter showed a significant linear correlation compared with the percentage of Al2O3 and had an RMSE value of 6.0% Al2O3 (Figure 4.9A; 788 samples). The algorithm 2260D showed a low linear correlation with a higher RMSE of 10.4% Al2O3 (Figure 4.9B) because of the smaller number of samples (205). This accuracy is within the error range of 5 to 10% reported by Zhang et al. (2001) in the quantification of clays using absorption features related to clays in the SWIR.

The Al-smectite abundance algorithm cannot be correlated with the percentage of Al2O3 measured in the XRF because of the small depth of the absorption feature at ~2200 nm (2200DS) in most of the analysed samples.

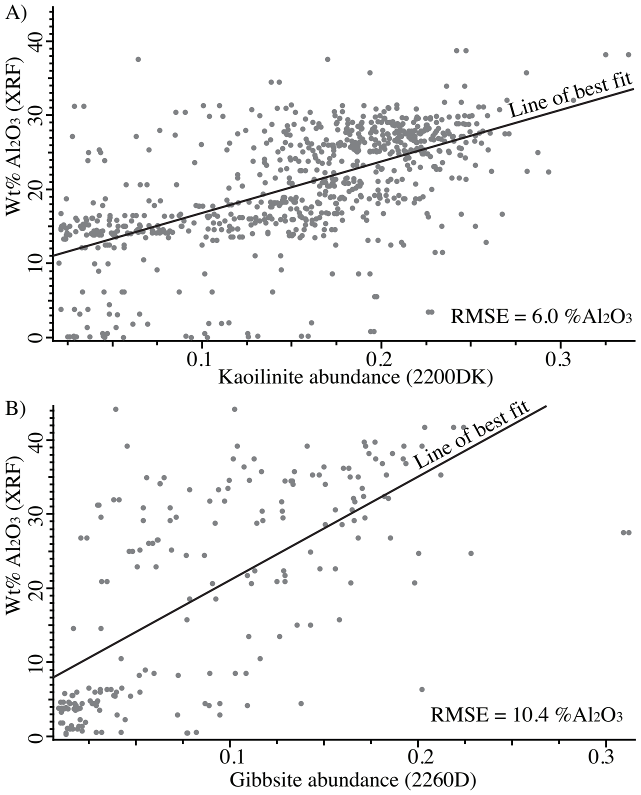

**Figure 4.9** A) Correlation between kaolinite (2200DK) abundance and %Al2O3 (XRF; 788 samples). B) Correlation between gibbsite (2260D) abundance and %Al2O3 (XRF; 205 samples).

*Abundance and composition of chlorite*

The chlorite (2335D) abundance algorithm was correlated with the percentage of Fe2O3 + MgO obtained in the XRF analyses. The abundance of chlorite (2335D) did not show a significant linear correlation with the percentage of Fe2O3 + MgO. However, the identified chlorites are from the metamorphism of the mafic rocks of the N4WS deposit. Therefore, an increase in the abundance of chlorite is not necessarily related to the iron and magnesium enrichment of the mafic rocks.

The composition of chlorite obtained by the parameter 2335Wvl was correlated with the %MgO of the XRF analyses (Figure 4.10). The histogram in Figure 4.4.10 shows that the samples with the longest wavelength of the 2335 nm absorption feature showed a lower percentage of MgO in the XRF analyses and samples with the shortest wavelengths of the 2335 nm feature showed a greater percentage of MgO in the analyses. The histogram also shows that Fe-chlorites predominate in the N4WS deposit samples.

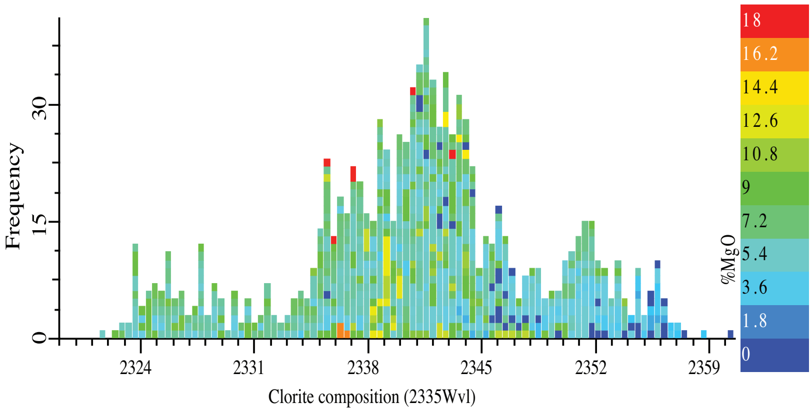

**Figure 4.10** Histogram of the chlorite composition obtained by the 2335Wvl algorithm. The histogram bars are coloured according to the %MgO obtained by the XRF analyses of the samples.

### *Abundance of talc*

The absorption feature at ~2310 nm (2310D) used in the talc abundance algorithm was correlated with the %MgO obtained in the XRF analyses of the drill cores (Figure 4.11; 242 samples). The 2310D algorithm showed a significant correlation with the %MgO of the XRF analyses, which had an RMSE value of 7.9% MgO. Certain samples with high %MgO in the XRF analyses had a low depth of the absorption feature at ~2310 nm (2310D). The heterogeneous distribution of talc in the samples makes it difficult to obtain spectra representing the chemical composition of the entire sample; thus, spectra were obtained from regions with distinct talc concentrations in the same sample.

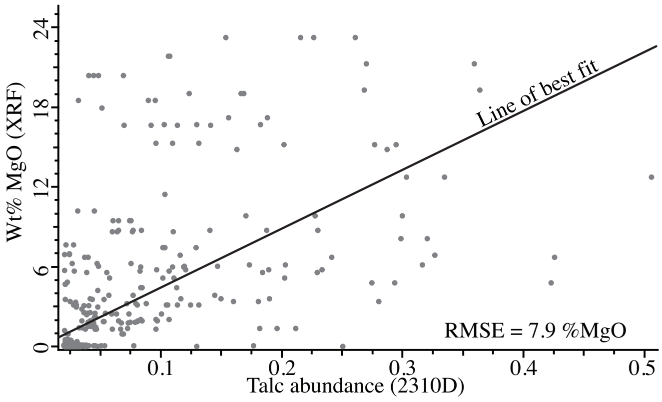

**Figure 4.11** Correlation between the abundance of talc obtained by spectral analysis of the samples (algorithm 2310D) and %MgO obtained by XRF analysis. The line shows the linear function that best fits the data. Number of samples: 242.

*Abundance and composition of carbonates*

The carbonate abundance algorithm was validated using the sum of the percentage of CaO and MgO obtained in the XRF analyses. The depth of the absorption feature at ~2330 nm (2330D) in the carbonates showed a low correlation with the %CaO + %MgO, and it had an RMSE value of 6.8% CaO + MgO (Figure 4.12A; 70 samples). However, the small number of samples with carbonates hinders the correlation of these data.

The carbonates composition algorithm was validated using the %CaO and %MgO data from the XRF analyses. The %CaO and %MgO of the samples with carbonate are shown in Figure 4.12B and coloured according to the wavelength of the 2330 nm feature (Composition of carbonates, Table 4.2). The line in Figure 4.12B (%CaO = 1.6 x %MgO) represents the line at which the dolomite samples with ideal composition (CaMg(CO3)2) should be located to comply with the stoichiometric ratios between the percentages of Ca and Mg because the molar mass of Ca is 1.6 times greater than that of Mg. Samples located along this line have an absorption feature related to CO32- (2330Wvl) between 2321 and 2330 nm (blue to green, Figure 4.12B), indicating dolomitic carbonates with more MgO (Gaffey, 1986; Clark et al., 1990), which is consistent with the geochemical data obtained with XRF. Samples above the dolomite line have a 2330 nm feature at higher wavelengths ranging between 2330-2343 nm, indicating calcitic carbonates poor in magnesium, (Gaffey, 1986; Clark et al., 1990), which is consistent with the %CaO increase determined by the XRF analyses.

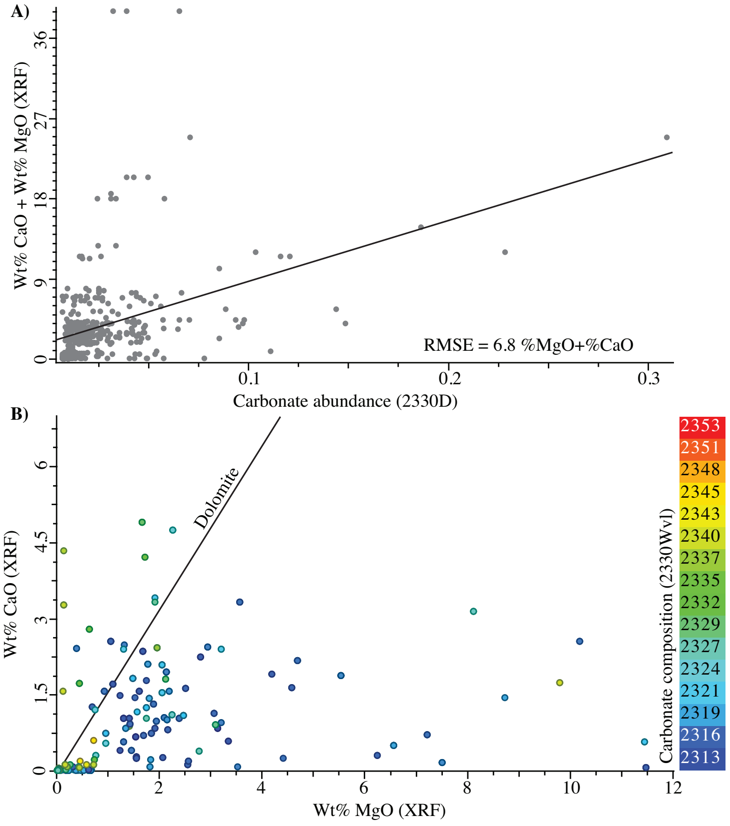

**Figure 4.12** A) Correlation between carbonate (2330D) abundance and %CaO + %MgO of the XRF analyses. The line shows the linear function that best fits the data. Number of samples: 70. B) %CaO vs. %MgO measured by XRF for the samples with carbonate identified through the reflectance spectrum by the 2330D algorithm. The samples are coloured according to the wavelength of the absorption feature at 2330 nm, which was obtained by the 2330Wvl algorithm. Number of samples: 70.

## 4.6ANALYSIS OF THE SPECTRAL PARAMETERS

### *Spectral characterisation of the lithotypes mapped in N4WS*

The spectral parameters obtained by the algorithms in Table 4.2 were used for the in-depth spatial analysis of the nine drill cores. The mineral abundance, crystallinity and composition data obtained from the spectra, geochemical analyses (XRF) and the magnetic susceptibility were used to characterise the lithotypes described and determine areas with similar chemical composition and mineralogy. The spectral characteristics observed are described below.

OC: abundance of iron (hydro-)oxides (900D/1650R) in OC varies between 0.7 and 2.1 and is similar to the variation observed in jaspilites. However, the presence of gibbsite, identified by the 2260D algorithm allows its differentiation from JP and FH. The geochemical data show that this lithotype has higher %Al2O3 (XRF) than JP, which is consistent with the identification of gibbsite in the spectra (Figure 4.14, interval of 45-65 m and Figure 4.15, interval of 0-20 m);

CC: similar to the OC, CC has an iron (hydro-)oxide (900D/1650R) abundance similar to the JP. The abundance of gibbsite, identified by the 2260D algorithm, is greater than that of OC as well as the %Al2O3 (XRF). Certain spectra obtained for the regolith of the mafic rock indicate the presence of talc (Figure 4.14, interval of 0-45 m);

JP: The spectral parameters differentiated JP in four domains, namely: hematite-rich JP (JP(H)), hematite-goethite-rich JP (JP(HG)), JP with talc (JP(T)) and JP with carbonate (JP(C)). The abundance of iron (hydro-)oxides (900D/1650R) is similar in the four domains and varies proportionally to the total %Fe2O3 (XRF; Figure 4.14 and Figure 4.15).

The HG distribution obtained by the 900Wvl algorithm (Table 4.2) was able to differentiate JP(H) and JP(HG). The JP(H) showed 900Wvl values ranging between 872-890 nm, which were lower than the values found in JP(HG) (Figure 4.14, interval of 140-330 m and Figure 4.15, interval of 215-255 m). The increased goethite in JP was related to an increased supergene alteration because JP near the surface has a higher amount of goethite (Figure 4.13) as well as to the proximity of brecciated zones (interval between 360 and 530 m, Figure 4.13). The goethite found near breccias are most likely of hydrothermal origin, such as those described in the study of Lobato et al. (2005). The JP(C) domain can be differentiated from other domains by the carbonate abundance algorithm 2330D (Table 4.2; Figure 4.14, intervals of 390-400 m and 475-530 m, and Figure 4.15, interval of 280-310 m). The samples from this domain had a 2330D index that is superior to all other lithotypes as well as the %CaO (XRF) and %MgO (XRF). In the JP(C) domain, the identification of talc was also possible in certain samples through the 2310D algorithm. The magnetic susceptibility in this domain was higher than in the others, reaching 0.75 (SI unit). Some samples of the JP(C) domain were analysed under a microscope, which confirmed the presence of carbonate and talc. These minerals fill the veinlets of brecciated jaspilite and disseminated in the jasper bands, replacing the primary mineralogy consisting of quartz and hematite. In addition, most of the samples from this domain have porphyrotopes of magnetite in transition to hematite (Figure 4.13F).

The samples from JP(C) zones have a large number of veins filled by carbonates and several brecciated regions (Figure 4.13A). Although the entire interval has been described as JP in the recording of the core, these brecciated regions had already been detected during the recording. However, the areas abundant in talc, which surround the carbonate areas, had not been detected during recording of the core because of the difficulty of visually identifying talc in JPs. The same relationship was observed in other boreholes, where the intervals of JP(C) are surrounded by intervals of JP(T). The appearance of talc in JP(T) intervals may be related to a distal hydrothermal alteration of JPs promoted by the fluids involved in the carbonate veining/brecciating of the JP(C) domain. These brecciated JP intervals can be correlated with the hydrothermalised areas described in Lobato et al. (2005; 2008), Rosiére et al. (2006) and Figueiredo and Silva et al. (2008; 2011).

FH: The abundance of iron (hydro-)oxides found by the 900D/1650R algorithm in the FH is greater than the abundance found in the OC and in the JP, with the 900D/1650R index ranging from 1 to 4.5. The FH has a large variation in the 900D/1650R index, which can be used to distinguish areas with a higher abundance of iron (hydro-)oxides within the unit. The %Fe2O3 of this unit varies up to 10% and is proportional to the variation of the iron (hydro-)oxide abundance ratio. Similar to the JPs, the distribution of hematite-goethite (900Wvl) can be used to distinguish FH in hematite (H) and hematite-goethite (HG). The FH has 900Wvl index values ranging between 872-890 nm lower than the values found in FH with the highest percentage of goethite (HG; Figure 4.15, interval of 20-190 m);

UM and SDM: Fresh or semi-altered mafic rocks are characterised by inclusions of chlorite and/or kaolinite and identified by the 2335D and 2200K algorithms, respectively. These spectral parameters allowed their differentiation in two domains, namely: mafic rock with chlorite predominance (M(Cl)) and mafic rock with kaolinite predominance (M(K)). The intervals more abundant in chlorite (M(Cl)) are correlated with UM (Figure 4.14, interval of 535-560 m, and Figure 4.15, interval of 330-350 m). An analysis of the sections of this unit showed that chlorite is the most abundant alteration mineral in the mafic rocks (Figure 4.13H and I). According to Zucchetti (2007), a portion of the chlorite crystals was formed by submarine hydrothermal alteration and recrystallised during regional metamorphism. Subsequently, a new generation of chlorite formed because of the hydrothermal alteration to chlorite + hematite. The composition of chlorite identified by the 2335Wvl algorithm in these domains can be used to distinguish intervals where Fe-chlorites are predominant from intervals where Mg-chlorites are predominant. The variation in chlorite composition may be the result of supergene alterations of the mafic rocks; however, Zucchetti (2003) proposed that there is a compositional variation in hydrothermal chlorites, with the Mg-chlorites associated with oxidising hydrothermal fluids that promote the crystallisation of hydrothermal hematite together with chlorite. The M(K) domain is correlated with SDM (Figure 4.14, interval of 100-140 m) because the appearance of kaolinite indicates a greater degree of supergene alteration of the mafic rocks. The crystallinity of kaolinite, obtained by the parameter 2170SL, can be used to distinguish intervals in the M(K) domain with a predominance of kaolinites of low crystallinity. These intervals may indicate fault zones or fractures in which kaolinite recrystallized.

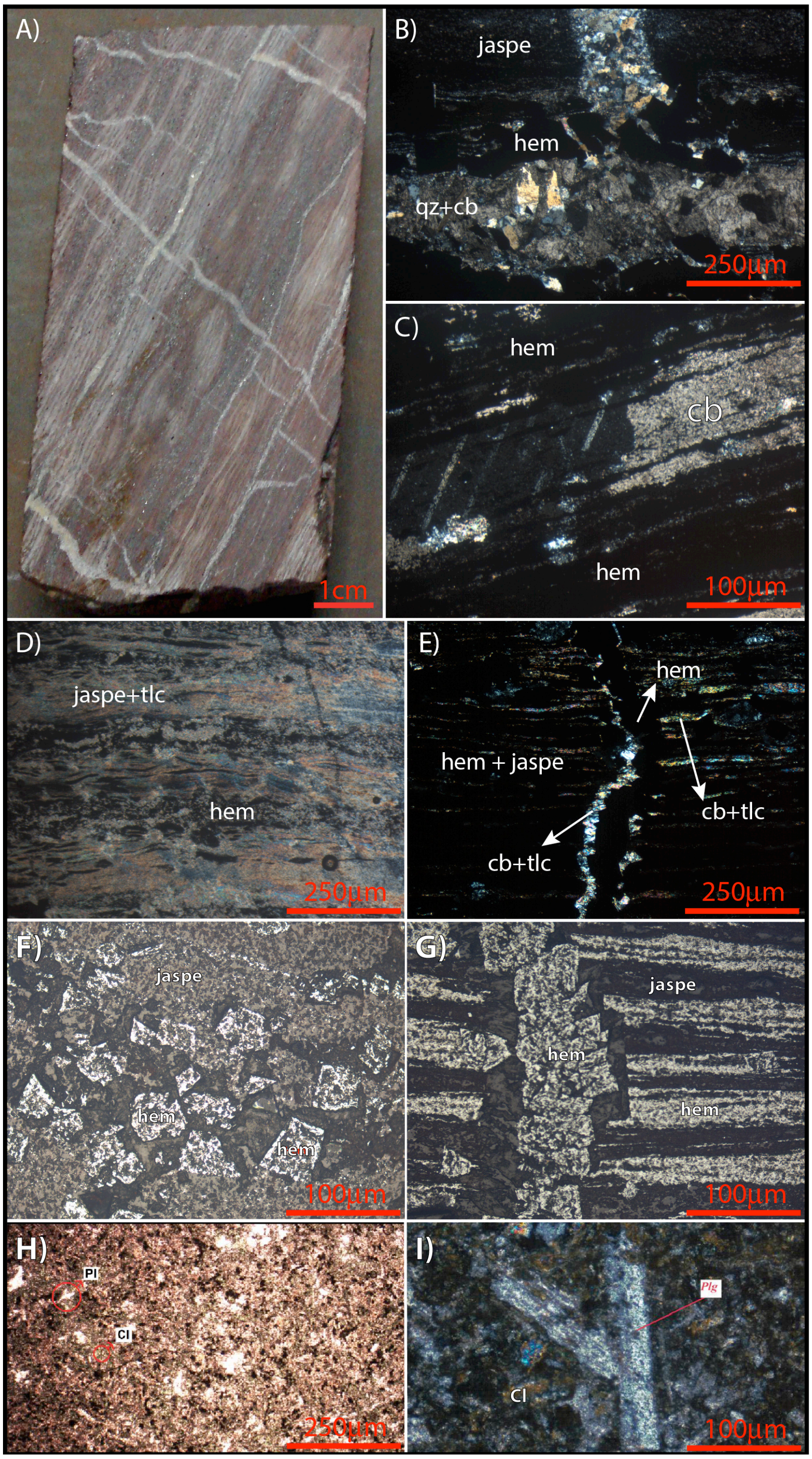

**Figure 4.13** A) Photo of brecciated jaspilite with carbonate veinlets (JP(C)). B) Photo of the brecciated jaspilite section (JP(C)) in transmitted light; in detail, veinlets filled with carbonate and quartz; crossed nicols. C) Photo of jaspilite with jasper bands replaced by a carbonate section in the transmitted light; crossed nicols. D) Photo of jaspilite with talc in the jasper bands section in transmitted light; crossed nicols. E) Jaspilite with veinlets filled with talc and carbonate. F) Photo of jaspilite with martite sections in reflected light. G) Photo of the section in reflected light of the photo detail in D), showing a veinlet filled by hematite. H) Photo of the fresh mafic (UM) section in transmitted light showing the preserved igneous texture; parallel nicols. I) Photo detail of H) with crossed nicols. Highlighted is a plagioclase crystal and matrix being altered to chlorite. hem, hematite; tlc, talc; cb, carbonate; qz, quartz; pl, plagioclase; and cl, chlorite.

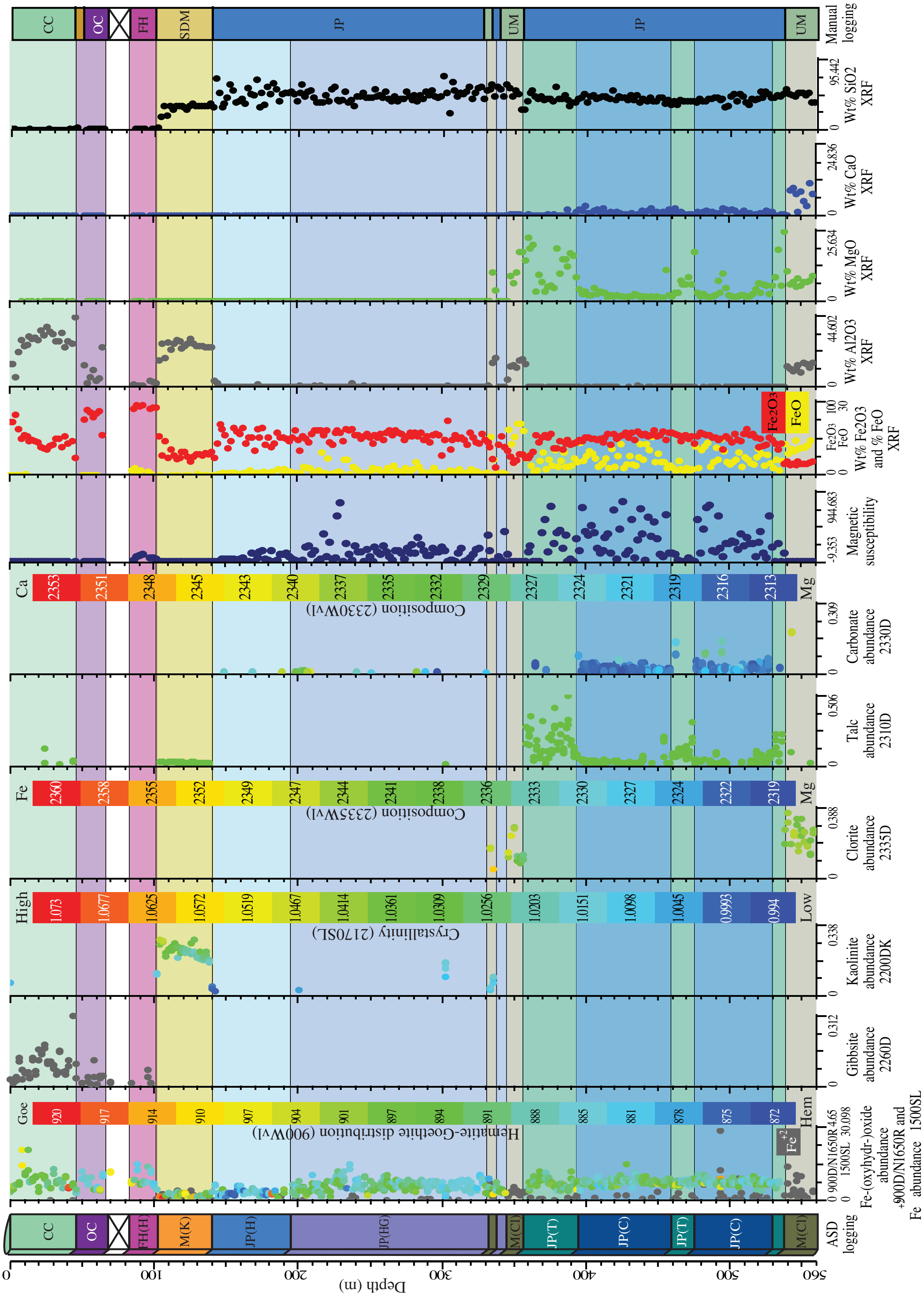
Depth (m)
0
100
200
300
400
500
560
ASD logging
CC
OC
FH(H)
M(K)
JP(H)
JP(HG)
M(Cl)
JP(T)
JP(C)
Fe-(oxyhydr-)oxide abundance +900D/N1650R and Fe abundance 1500SL
0 900D/N1650R 4.65
0 1500SL 30.098
Hematite-Goethite distribution (900Wvl)
Goe
920 917 914 910 907 904 901 897 894 891 888 885 881 878 875 872
Hem
Fe+2
Gibbsite abundance 2260D
0 0.312
Kaolinite abundance 2200DK
0 0.338
Crystallinity (2170SL)
High
1.073 1.0677 1.0625 1.0572 1.0519 1.0467 1.0414 1.0361 1.0309 1.0256 1.0203 1.0151 1.0098 1.0045 0.9993 0.994
Low
Clorite abundance 2335D
0 0.388
Composition (2335Wvl)
Fe
2360 2358 2355 2352 2349 2347 2344 2341 2338 2336 2333 2330 2327 2324 2322 2319
Mg
Talc abundance 2310D
0 0.506
Carbonate abundance 2330D
0 0.309
Composition (2330Wvl)
Ca
2353 2351 2348 2345 2343 2340 2337 2335 2332 2329 2327 2324 2321 2319 2316 2313
Mg
Magnetic susceptibility
-9.353 944.683
Wt% Fe2O3 and % FeO XRF
Fe2O3 0 100
FeO 0 30
Fe2O3
FeO
Wt% Al2O3 XRF
0 44.602
Wt% MgO XRF
0 25.634
Wt% CaO XRF
0 24.836
Wt% SiO2 XRF
0 95.442
Manual logging
CC
OC
FH
SDM
JP
UM
JP
UM

**Figure 4.14** Results of mineral abundance and composition analyses using the reflectance spectroscopy data for the F1515 borehole. The geochemical analysis of certain elements obtained by XRF, magnetic susceptibility and lithotypes described during the recording of the cores are also shown. The scatter plots show variations in mineral abundance as a function of depth. Certain diagrams are coloured in accordance with the sweeping in the composition of these minerals. The colour bars in the diagrams of abundance of iron (hydro-)oxides, chlorite and carbonate show the wavelength in nm of the reflectance minimum of the absorption feature of these minerals. The diagram of abundance of kaolinite is coloured according to the crystallinity of kaolinite. The intervals that have similar mineralogical characteristics were grouped into the same colour horizons.

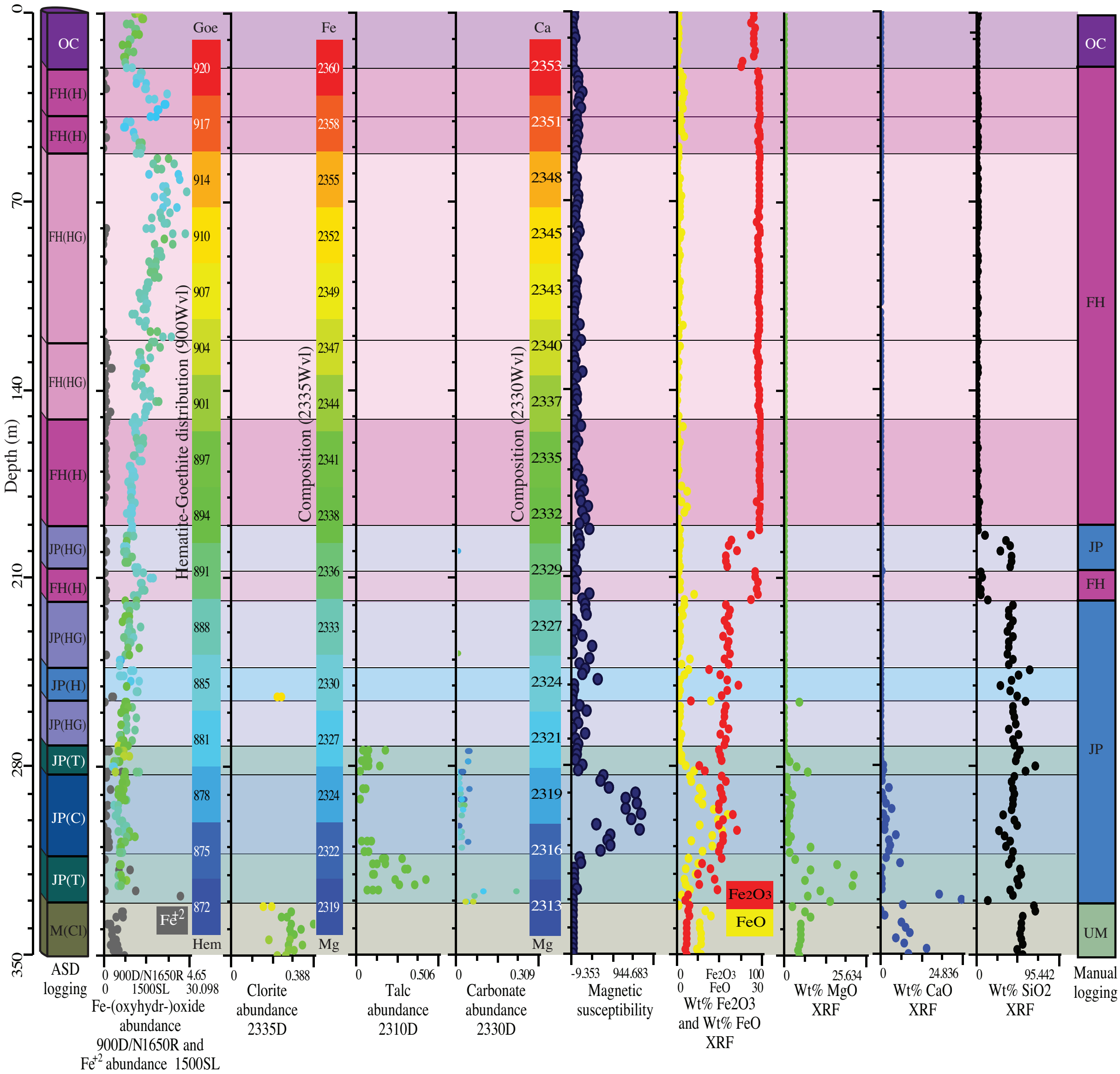

**Figure 4.15** Results of abundance and mineral composition analyses using the reflectance spectroscopy data for the F1051 borehole. The geochemical analysis of certain elements obtained by XRF, magnetic susceptibility and lithotypes described during the recording of the core are also shown. The scatter plots show variations in mineral abundance as a function of depth. Certain diagrams are coloured in accordance with the sweeping in the composition of these minerals. The colour bars in the diagrams of abundance of iron (hydro-)oxides, chlorite and carbonate show the wavelength in nm of the reflectance minimum of the absorption feature of these minerals. The intervals that have similar mineralogical characteristics were grouped into the same colour horizons.

*Correlation of spectral parameters in 2D*

After performing a spectral characterisation of the lithotypes described in drill cores, a two dimensional (2D) analysis was performed in which the spectral domains were correlated in the profile. Figure 4.16 shows one of the correlated profiles. To facilitate the correlation, boreholes that were not analysed in this study were added to the profile (analysed boreholes are highlighted in Figure 4.16).

The spectral domains showed good correlations in the profile and helped to identify areas that were not distinguished in previous lithological correlations. The ease of determining the intervals of brecciated JP (JP(C)) and JP(T) facilitated determining the spatial distribution of these intervals in the profile. These intervals predominated at the base of the analysed cores, indicating that the brecciation related to carbonation/talcification of JPs occurred near the basal basalt of the cores. The JP(T) surround the brecciated JP(C), illustrating the relationship between talcification with brecciation and carbonation of JPs.

The hydrothermal hypogene model for the iron mineralisation of the Carajás Mineral Province proposed in Lobato et al. (2005; 2008), Rosiére et al. (2006) and Figueiredo and Silva et al. (2008; 2011) suggests that JPs richer in iron are found in brecciated zones that experienced leaching of silica and crystallisation of magnetite, hematite, goethite, chlorite, talc and sulphides. However, the brecciated JP found in the JP(C) and JP(T) zones had an abundance of iron (hydro-)oxide determined by spectral analysis (900D/1650R algorithm) and %Fe2O3 obtained by geochemical analysis similar to non-brecciated JPs. The JPs from the N4WS deposit, which is richer in iron, were strongly weathered, and represented by FH, which resulted from the supergene alteration of JPs.

The correlation of spectral domains was also used to detail the contact between the OC and FH. The presence of clay minerals and increased abundance of goethite are characteristics of the OC that can be accurately identified by analysing the spectra, which can be used to differentiate OC from FH. Detailing the contact between these units is important for ore mining planning because the identification and quantification of clay minerals, such as gibbsite and kaolinite, affect ore processing planning.

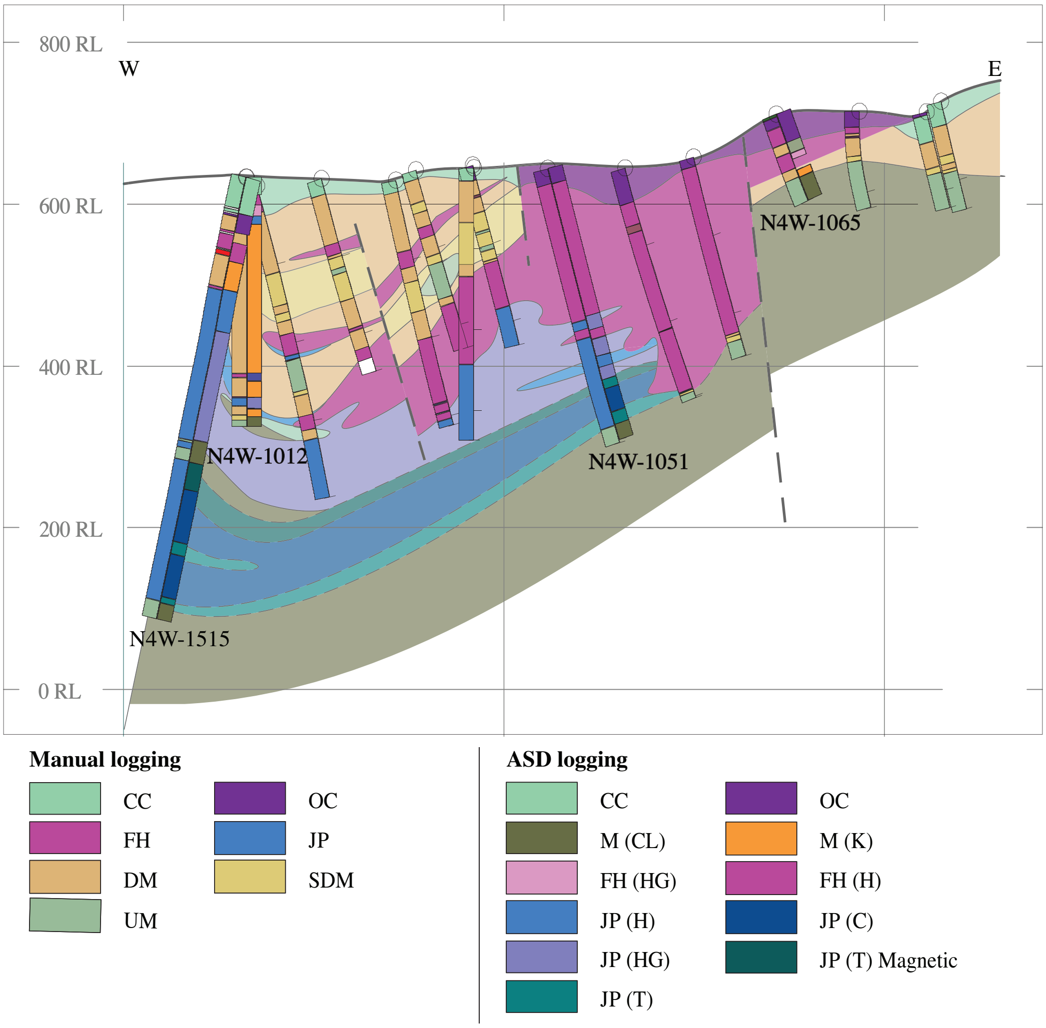

**Figure 4.16** Lithological section interpreted from the N4WS deposit running through the N4W-1515, N4W-1012, N4W-1051 and N4W-1065 cores (Figure 4.2). The lithotypes were correlated according to the spectral domains, which represent compositional variations of the mapped lithologies. The unidentified cores were added to facilitate interpretation, and they only show the lithology. The dotted lines indicate possible faults. CC: chemical canga; OC: ore canga; FH: friable hematite; FH(HG): friable hematite with greater abundance of goethite; FH (H): friable hematite with lower abundance of goethite; JP: jaspilite; JP(H): hematite-rich jaspilite; JP(HG): jaspilite with goethite; JP(C): jaspilite with carbonate; JP(T): jaspilite with talc; DM: decomposed mafic; SDM: semi-decomposed mafic; UM: unweathered mafic; M(CL): mafic with chlorite; M(K): mafic with kaolinite.

## 4.7CONCLUSION

The algorithms developed to estimate the abundance and composition of minerals based on reflectance spectroradiometry data were successfully validated using independent geochemical data of the same samples from the N4WS iron deposit, which is located in the Carajás Mineral Province in northern Brazil. The validated spectral algorithms provided the following information.

1. The estimation of iron (hydro-)oxide abundance, which showed a significant correlation with the %Fe (XRF) data for most of the ~1700 core samples, had an RMSE of 15.8% of Fe. A large part of the error is associated with changes dependent on the albedo wavelength of the samples because of a combination of variations in grain size and behaviour of trans-opaque iron (hydro-)oxides as well as different amounts of silica (quartz), thus causing variations in the distance between the sensor and iron (hydro-)oxides.

2. The accuracy of the algorithm that defines the hematite-goethite distribution was validated using the LOI data of the samples, and a significant correlation was observed between the values of the algorithm and the LOI results.

3. The aluminous clays abundance algorithms were correlated with the %Al2O3 (XRF) data and had an RMSE value of 6% for kaolinite and 10.4% for gibbsite. Similar to the iron (hydro-)oxide results, the accuracy of the abundance of aluminous clays based on the spectra is negatively influenced by the presence of silica in the samples. Moreover, the error can also be associated with the substitution of Al in the goethite structure.

4. The chlorite abundance algorithm was correlated with the percentage of Fe2O3 + MgO obtained in the XRF analyses. The abundance of chlorite did not show a significant linear correlation with the XRF data. However, the identified chlorites may have originated from the metamorphism or metasomatism of the mafic rocks of the N4WS deposit. Therefore, the increase in chlorite abundance is not necessarily related to the Fe and/or Mg enrichment of the mafic rocks.

5. The chlorite composition algorithm was correlated with the %MgO of the XRF analyses. The samples showed a significant correlation with the XRF data.

6. The talc abundance obtained using the reflectance data was correlated with the %MgO obtained in the XRF analyses of the drill cores. The algorithm showed a significant correlation with the %MgO of the XRF analyses and had an RMSE of 7.9% for MgO. Certain samples with high %MgO in the XRF analyses had low abundance values according to the algorithm. However, this error may have been caused by the

heterogeneous distribution of the talc in the samples, which makes it difficult to obtain spectra representing the chemical composition of the entire sample.

7. The carbonate abundance algorithm was validated using the sum of the percentage of CaO and MgO obtained in the XRF analyses. The algorithm showed low correlation with the %CaO + %MgO obtained in the XRF analyses and had an RMSE of 6.8% for CaO + MgO. However, the small number of samples with carbonates hindered the correlation of these data.

8. The carbonate composition algorithm was validated using the sum of the percentage of CaO and MgO obtained in the XRF analyses and showed a significant correlation with the XRF data.

This study showed that reflectance spectroradiometry in the VNIR-SWIR regions can be used to characterise and evaluate the mineral distribution of an iron deposit. The main minerals found in the N4WS iron deposit were identified, including the mineralogy of the ore. An analysis of the thin sections showed that all of the minerals identified by reflectance spectroradiometry were present in the samples.

The mineral abundance parameters obtained in this study, which had RMSE values between 6 and 15.8%, indicated that this method can be useful as a quick estimate of the content of iron and certain minerals associated with the deposit. Hillier (2000) showed that quantitative analyses using the XRD results of clays and other minerals in sandstones and other rock samples in general are capable of producing results with ± 3% accuracy and a confidence level of 95%. These routine analyses with XRD, however, require significant time for sample preparation and data collection, and problems may still arise (e.g., preferential orientation, different smectite mixtures, etc.).

The analysis of the spectral parameters obtained by the algorithms were capable of identifying the ore, protore and host rocks described during the recording of the cores and detailing the intervals, which produced the following results:

1. Minerals were identified that had not described before in these rock types, such as the talc identified in some JP samples;

2. Zones that are difficult to differentiate were distinguished; e.g., zones where hematite is predominant were differentiated from the zones where goethite is predominant in the JP and FH intervals;
3. Zones with higher oxide content were differentiated in the JP and FH intervals;
4. Zones with carbonate were differentiated in the JP intervals;
5. Chlorite composition was identified in the basalt intervals;
6. Basalts and semi-decomposed mafic were differentiated by the kaolin content obtained using the kaolinite abundance algorithm.

Therefore, quick spectral analyses of drill cores are of great value because they can easily generate information required by geoscientists for the mineralogical characterisation of geological environments. In addition, the universal applicability of these spectral algorithms is becoming reality because validation studies such as the study presented here have been performed using different spectral systems in different geological environments.

## 4.8ACKNOWLEDGMENTS

We gratefully acknowledge Vale for permitting the use of geological data and access to the N4WS, as well as the research funding, , the National Council for Scientifical and Technological Development (CNPq) for the research grant to A.M. Silva and E.M.G Prado scholarship. D.F.Ducart thanks the Coordination for Enhancement of Higher Education Personnel (CAPES) for his fellowship toward his postdoctoral research. We also thank the Laboratory of Applied Geophysics of the University of Brasília for technical support.

## 4.9BIBLIOGRAPHY

Adams, J.B., 1974. Visible and near-infrared diffuse reflectance: spectra of pyroxenes as applied to remote sensing of solid objects in the solar system. J. Geophys. Res. 79, 4829–4836.

Adams, J.B., 1975. Interpretation of visible and near-infrared diffuse reflectance spectra of pyroxenes and other rock forming minerals. In: Karr, C. (Ed.), Infrared and Raman Spectroscopy of Lunar and Terrestrial Materials. Academic Press, New York, pp. 91–116.

Adams, J.B., and Filice, A.L., 1967, Spectral reflectance 0.4 to 2.0 microns of silicate rock powders: Journal of Geophysical Research, v. 72, p. 5705–5715.

Almeida, F. F. M., Hasui, Y., Neves, B. B. B., e Fuck, R. A., 1977. Províncias estruturais brasileiras (pp. 363–391). In: Simpósio de Geologia do Nordeste, 8, Campina Grande, 1977.: Atas... Campina Grande, SBG, p. 363-391.

Araújo, O.J.B., Maia, R.G.N., Jorge João, X.S., Costa, J.B.S., 1988, A megaestruturação arqueana da Folha Serra dos Carajás: Anais do Congresso Latinoamericano de Geologia, v. 1, p. 324-338.

Araújo, O.J.B., and Maia R.G.N. 1991. Programa levantamentos geológicos básicos do Brasil. Projeto especial mapas de recursos minerais, de solos e de vegetação para a área do Programa Grande Carajás: Subprojeto Recursos Minerais, Serra dos Carajás, Folha SB.22-Z-A. Brasília, DNPM/Companhia de Pesquisa e Recursos Minerais-CPRM, 152 p.

Assis L. M. 2013. Geração de Modelo Exploratório para o Minério de Ferro da Província Mineral de Carajás Através da Integração de Dados Multifonte. Dissertação de Mestrado, Universidade de Brasília, Brasília. 154 p.

Beisiegel, V.R., Bernardelli, A.L., Drummond, N.F., Ruff, A.W., Tremaine, J.W. 1973. Geologia e recursos minerais da Serra dos Carajás: Revista Brasileira de Geociências, v. 3: 215-242.

Beukes, N.J., Gutzmer, J., and Mukhopadhyay, J., 2002. The geology and genesis ofhigh-grade hematite iron ore deposits: Australasian Institute of Mining and Metallurgy, Publication Series, 7: 23-29.

Bishop, J.L., Lane, M.D., Dyar, M.D., and Brown, A.J., 2008, Reflectance and emission spectroscopy study of four groups of phyllosilicates: Smectites, kaolinite-serpentines, chlorites and micas: Clay Minerals, v. 43, p. 35–54.Burns, R.G., 1993. Origin of electronic spectra of minerals in the visible and near-infrared region. In: Pieters, C.M., Englert, P.A.J. (Eds.), Remote Geochemical Analysis: Elemental and Mineralogical Composition. Cambridge University Press, New York, pp. 3–30.

Burns, R. Mineralogical Applications of Crystal Field Theory, Second Edition, Cambridge University Press, Cambridge, 551p. 1993.

Carioca, A. C., Costa, G. M., Barrón, V., Ferreira, C. M., Torrent, J., 2011. Application of diffuse reflectance spectroscopy in the quantification of the constituents of bauxite and iron ore. Revista Escola de Minas, Ouro Preto, v. 64(2), p. 199-204.

Clark, R.N., and Roush, T.L., 1984, Reflectance spectroscopy-quantitativeanalysis techniques for remote-sensing applications: Journal of GeophysicalResearch, v. 89, p. 6329–6340.

Clark, R.N., King, T.V.V., Klejwa, M., Swayze, G.A., and Vergo, N., 1990,High spectral resolution reflectance spectroscopy of minerals: Journal of Geophysical Research, v. 95, p. 12653−12680.

Cordani, U.G., Tassinari, C.C.G., Teixeira, W., Basei, M.A.S., Kawashita, K., 1979. Evolução tectônica da Amazônia com base nos dados geocronológicos. Congress. Geol. Chileno, 2, Arica, Chile, Actas, 4: 137-148.

Crowley, J.K., and Vergo, N., 1988, Near-infrared reflectance spectra of mixtures of kaolin-group minerals: Use in clay mineral studies: Clays and Clay Minerals, v. 36, p. 310−316.

Cudahy, T., 1997a, Pima-II spectral characteristics of natural kaolins, CSIRO/AMIRA Project P435: Sydney, Australia, CSIRO Division for Exploration and Mining Report 420R, 62 p.

Cudahy, T., Jones, M., Thomas, M., Cocks, P., Agustin, F., Caccetta, M., Rodger, A., 2009. Drill core logging of plagioclase feldspar composition and other minerals associated with Archean gold mineralization at Kambalda, Western Australia, using bidirectional thermal infrared reflectance system. Reviews in Economic Geology, 16, 223–235.

Cudahy, T., Jones, M., Thomas, M., Laukamp, C., Caccetta, M., Hewson, R.,Rodger, A., and Verrall, M., 2008, Next generation mineral mapping:Queensland Airborne

HyMap and Satellite ASTER surveys 2006–2008:Perth, Publicly Available Report P2007/364 (http://c3dmm.csiro.au/NGMM/), CSIRO Exploration and Mining, 152 p.

Cudahy, T., and Ramanaidou, E.R., 1992, Relationships between spectral properties and ferric oxides, CSIRO/AMIRA Project P243: Wembley, Australia, CSIRO Division of Exploration Geoscience Report 244R, 68 p.

—1997, Measurement of the hematite:goethite ratio using field visible and near-infrared reflectance spectrometry in channel iron deposits, Western Australia: Australian Journal of Earth Sciences, v. 44, p. 411–420.

Curtiss, B., 1985, Evaluation of the physical properties of naturally occurringiron (III) oxyhydroxides on rock surfaces in arid and semi-arid regionsusing visible and near infrared spectroscopy: Unpublished Ph.D. thesis, Seattle, WA, University of Washington, 106 p.

Dall'Agnoll, R., e de Oliveira, D. C., 2007. Oxidized, magnetite-series, rapakivi- type granites of Carajás, Brazil: Implications for classification and petrogenesis of A-type granites. Lithos, 93, 215–233.

Dalstra, L. W., e Guedes, S. 2004. Giant hydrothermal hematite deposits with Mg-Fe metasomatism: A comparison of the Carajás, Hamersley, and other iron ores. Economic Geology, 99, 1793–1800.

DOCEGEO. (1988). Revisão litoestratigráfica da Província Mineral de Carajás: Congresso Brasileiro de Geologia, 35th, Sociedade Brasileira de Geologia, Belém, Brazil, 11–54.

Domingos, F.H.G., 2009, The structural setting of the Canaã dos Carajás region and Sossego-Sequeirinho deposits, Carajás, Brazil: Unpublished Ph.D. dissertation, Durhan, United Kingdom, Durham University, 483 p.

Ducart, D. F., 2004. Caracterização da alteração hidrotermal associada às ocorrências auríferas de Los Menucos, Argentina, por meio de técnicas de sensoriamento remoto e espectroscopia de reflectância. Dissertação de Mestrado em Geociências. Universidade Estadual de Campinas,, 86.

Ducart, D. F., 2006. Alteração hidrotermal do prospecto aurífero Cerro La Mina, Los Menucos, Patagônia, Argentina: geologia, sensoriamento remoto e isótopos estáveis. Tese de dourado em Geociências. Universidade Estadual de Campinas, Campinas-SP, 173.

Ducart, D. F., Crósta, A. P., Souza Filho, C. R., e Coniglio, J., 2006. Alteration Mineralogy at the Cerro La Mina Epithermal Prospect, Patagonia, Argentina: Field Mapping, Short-Wave Infrared Spectroscopy, and ASTER Images. Economic Geology, 101, 981–996.

Fernandes, R. B. A., Barrón, V., Torrent, J., Fontes, M. P. F., 2004. Quantification of iron óxides of brazilian soils using diffuse reflectance spectroscopy.Revista Brasileira de Ciências do Solo, v.28, p. 245-257.

Ferreira, V. N., 2014. Caracterização de formações ferríferas bandadas através de dados de propriedades físicas de rocha e sua integração com dados aerogeofísicos: o estudo de caso do corpo N4WS, Serra Norte –Província Mineral de Carajás. Dissertção de mestrado, Universidade de Brasília.

Figueiredo e Silva, R. C., Lobato, L. M., Rosière, C. A., Hagemann, S., Zucchetti, M., Baars, F. J., … Andrade, I., 2008. Hydrothermal origin for the jaspilite-hosted, giant Serra Norte iron ore deposits in the Carajás mineral province, Para State, Brazil. Reviews in Economic Geology, 15, 255–290.

Figueiredo e Silva, R. C., Lobato, L.M., Rosière, C.A., Hagemann, S.H. 2011. Petrographic andgeochemical studies at giant Serra Norte iron ore deposits in the Carajás mineral province, Pará State, Brazil. Geonomos, v.19, p.198 - 223. Gaffey, S.J., 1986, Spectral reflectance of carbonate minerals in the visible and near-infrared (0.35 to 2.55 microns): Calcite, aragonite, and dolomite: American Mineralogist, v. 71, p. 151–162.

Gibbs, A. K., Wirth, K. R., Hirata, W. K., e Olszewski, W. J., J., 1986. Age and composition of the Grão Pará Group volcanics, Serra dos Carajás. Revista Brasileira de Geociências, 16, 201–211.

Gonçalves, I. G., Petter, C. O., Machado, J. L., 2012. Quantification of hematite and goethite concentrations in kaolinusing diffuse reflectance spectroscopy: A new approach to Kubelka-Munk theory. Clays and Clay Minerals, v. 60, 473-483.

Grainger, C. J., Grooves, D. I., Tallarico, F. B., e Fletcher, I. R., 2008. Metallogenesis of the Carajás mineral province, southern Amazon craton, Brazil: Varying styles of Archean through Paleoproterozoic to Neoproterozoicbase- and precoius-metal mineralization. Ore Geology Reviews, 33, 451–484.

Haest, M., e Cudahy, T., 2012. Quantitative mineralogy from infrared spectroscopic data. I. Validation of mineral abundance and composition algoritms at the rocklea channel iron deposit in Western Australia. Economic Geology, 107(1983), 209–228. Retrieved from http://gsecongeo.highwire.org/content/107/2/209.short

Harraden C. L., Brian A. Mcnulty, Melissa J. Gregory, and James R. Lang. Shortwave Infrared Spectral Analysis of Hydrothermal Alteration Associated with the Pebble Porphyry Copper-Gold-Molybdenum Deposit, Iliamna, Alaska Economic Geology, v. 108, p. 483-494, doi:10.2113/econgeo.108.3.483. 2013.

Herrmann, W., Blake, M., Doyle, M., Huston, D., Kamprad, J., Merry, N. and Pontual, S.. Short wavelength infrared (SWIR) spectral analysis of hydrothermal alteration zones associated with base metal sulfide deposits at Rosebery and Western Tharsis, Tasmania, and Highway-Reward, Queensland. Economic Geology and the Bulletin of the Society of Economic Geologists, 96 (5), 939-955. 2001.

Hunt, G.R., 1977. Spectral signatures of particulate minerals in the visible and near-infrared. Geophysics 42, 501–513.

Hunt, G.R., and Ashley, R.P., 1979, Spectra of altered rocks in the visible and near-infrared: ECONOMIC GEOLOGY, v. 74, p. 1613−1629.

Hunt, G. R., and J. W. Salisbury, Visible and near-infrared spectra of minerals and rocks, I, Silicate minerals, Mod. Geol., 1, 283-300, 1970.

Hunt, G.R., Salisbury, J.W., and Lehnoff, C.J., 1971, Visible and near infrared spectra of minerals and rocks: III. Oxides and oxyhydroxides: Modern Geology,v. 2, p. 195−205.

Kruse, F. A., Boardman, J. W., e Huntington, J. F., 2003. Comparison of Airborne hyperspectral data and EO-1 Hyperion for mineral mapping. IEEE Transaction on Geosciences and Remote Sensing, 41(6), 1388–1400.

Krymsky, R. S., Macambira, J. B., e Macambira, M. B. J., 2002. Geocronologia U-Pb em zircão de rochas vulcânicas da Formação Carajás, Estado do Pará [abs.]. Simpósio sobre vulcanismo e ambientes associados, 2nd, Belém, Brazil, 41.

Lobato, L. M., Rosière, C. A., Figueiredo e Silva, R. C., Zucchetti, M., Baars, F. J., Seoane, J. C. S., … Monteiro, A. M. (2005). A mineralização hidrotermal de ferro da Província Mineral de Carajás-Controle estrutural e contexto na evolução metalogenética da província, in Marini, O.J., de Queiroz, E.T., and Ramos, B.W., eds., Caracterização de depósitos minerais em distritos mineir, 25–92.

Lobato L.M., Hagemann S.G., Figueiredo e Silva R.C., Thorne W., Zucchetti M., Gutzmer J. 2008. Hypogene hydrothermal alteration associated with BIF-related iron ore mineralization. In: Hagemann, S.G., Rosière, C.A., Gutzmer, J., and Beukes, N.J., BIF-Related High-Grade Iron Mineralization. Reviews in Econ. Geo., 15: 107-128.

Macambira, J. B., e Schrank, A., 2002. Químio-estratigrafia e evolução dos jaspilitos da Formação Carajás (PA). Revista Brasileira de Geociências, 32, 567–578.

Macambira J.B., 2003. O ambiente deposicional da Formação Carajás e uma proposta de modelo evolutivo para a Bacia Grão Pará. Tese de Doutorado, Instituto de Geociências, Universidade Estadual de Campinas, 217p.

Machado, N., Lindenmayer, Z., Krogh, T. E., e Lindenmayer, D., 1991. UPb geochronology of Archean magmatism and basement reactivation in the Carajás area, Amazon shield, Brazil. Precambrian Research, 49, 329–354.

Meirelles, E. M., Hirata, W. K., Amaral, A. F., Medeiros Filho, C. A., e Gato, W. C., 1984. Geologia das folhas Carajás e Rio Verde, Província Mineral de Carajás, Estado do Pará. Congresso Brasileiro de Geologia, Rio de Janeiro, Annals, 33, 2164–2174.

Morris, R.V., Lauer, H.V., Lawson, C.A., Gibson, E.K., Nace, G.A., and Stewart, C., 1985, Spectral and other physicochemcial properties of submicron powders of hematite (alpha-Fe2O3), maghemite (gamma-Fe2O3), magnetite (Fe3O4), goethite (alpha-FeOOH) and lepidocrocite (gamma-FeOOH): Journal of Geophysical Research-Solid Earth and Planets, v. 90, p. 3126–3144.

Mougeot, R., 1996. Estude de la limite Archeen-Proterozoique et des mineralizations Au, ±U associees. Exemples de la region de Jacobina (Etat de Bahia, Bresil) et de Carajás (Etat de Para, Bresil). Unpublished Ph.D. thesis, Monpellier, France, University of Montpellier II.

Olszewski, W. J., J., Wirth, K. R., Gibbs, A. K., e Gaudette, H. E., 1989. The age, origin, and tectonics of the Grão Pará Group and associated rocks, Serra dos Carajás, Brazil: Archean continental volcanism and rifting. Precambrian Research, 42, 229–254.

Pinheiro, R.V.L., and Holdsworth, R.E., 1997, Reactivation of Archaean strike-slip fault systems, Amazon region, Brazil: Journal of the Geological Society of London, v. 154, p. 99–103.

Post, J.L., and Noble, P.N., 1993, The near-infrared combination band frequencies of dioctahedral smectites, micas, and illites: Clays and Clay Minerals, v. 41, p. 639–644.

Rosière, C. A., Baars, F. J., Seoane, J. C. ., Lobato, L. M., da Silva, L. L., De Souza, S. R. C., e Mendes, G. E. (2006). Structure and iron mineralisation of the Carajás province. Transactions of the Institution of Mining and Metallurgy, 115, B126–B136.

Ross, P.-S, Bourke, A., Fresia, B. 2013. A multi-sensor logger for rock cores: Methodology and preliminary results from the Matagami mining camp, Canada. Ore Geology Reviews, v. 53, p. 93-111.

Santos, J.O.S., Hartmann, L.A., Gaudette, H.E, Groves, D.I., McNaughton, N.J., Flecher, I.R., (2000). New uderstanding of the Amazon Craton provinces, based on field work and radiogenic isotope data. Gondwana Research 3, 4: 453-488.

Santos, J. O. S., 2003. Geotectônica dos Escudos da Guianas e Brasil-Central, in Bizzi, L. A., Schobbenhaus, C., Vidotti, R. M., Gonçalves, J. H., eds., Geologia, Tectônica e Recursos Minerais do brasil, Compania de Pesquisa e Recursos Minerais-CPRM, 169–226.

Santos, J.S.O., Hartmann, L.A., Faria, M.S., Riker, S.R., Souza, M.M., Almeida, M.E. McNaughton, N.J., 2006. A compartimentação do Cráton Amazonas em províncias: avanços ocorridos no período 2000-2006. Simpósio de Geologia da Amazônia, 9, Sociedade Brasileira de Geologia, Belém, Brazil, Resumos Expandidos, CD ROM.

Senna, J. A., Souza Filho C. R., Angélica R. S., 2008. Characterization of clays used in the ceramic manufacturing industry by reflectance spectroscopy: An experiment in the São Simão ball-clay deposit, Brazil. Applied clay science, v. 41, p 85-98.

Sherman, D.M., and Waite, T.D., 1985. Electronic spectra of Fe3+ oxides and oxide hydroxides in the near IR to near UV: American Mineralogist, v. 70, p. 1262–1269.

Silva, G. g., Lima, M. I. C., Andrade, A. R. F., Issler, R. S., e Guimarães, G., 1974. Geologi das folhas SB-22 Araguaia e parte da SC-22 Tocantins, in Levantamento de Recursos Minerais, Projeto Radam (Departamento Nacional de Produção Mineral-SNPM e Companhia de Pesquisa e Recursos Minerais-CPRM), 143 p.

Silva, R. e, e Hagemann, S., 2013. Hydrothermal Fluid Processes and Evolution of the Giant Serra Norte Jaspilite-Hosted Iron Ore Deposits, Carajás Mineral Province, Brazil. Economic …, 108, 739–779. Retrieved from http://gsecongeo.highwire.org/content/108/4/739.short

Silva, S. M. P., 2009. Espectroscopia de imageamento e gamaespectrometria aérea e terrestre de pegmatitos e granitos da porção sul da Província Pegmatítica da Borborema (PPB), nordeste do Brasil. Tese de doutorado em Geociências, Universidade Estadual de Campinas, Campinas-SP, 173.

Sonntag, I., Laukamp, C., Hagemann, S. G., 2012. Low potassium hydrothermal alteration in low sulfidation epithermal systems as detected by IRS e XRD: An exemple from Co-O mine, eastern Mindanao, Philippines. Ore Geology Reviews, v. 45, p. 47-60.

Strezov, V., Ziolkowski, A., Evans, T.J., and Nelson, P.F., 2010, Assessment of evolution of loss on ignition matter during heating of iron ores: Journal of Thermal Analysis and Calorimetry, v. 100, p. 901–907.

Tallarico, F.H.B., 2003, O cinturão cupro-aurífero de Carajás, Brasil: Unpublished Ph.D. dissertation, Campinas, Brazil, Universidade Estadual de Campinas, 229 p.

Tassinari, C.C.G. 1996. O mapa geocronológico do Cráton Amazônico no Brasil: revisão dos dados isotópicos. 139p. Universidade de São Paulo, Instituto de Geociências, São Paulo. (Tese de Livre-doscência).

Tassinari, C.C.G. e Macambira, M.J.B. 1999. Geochronological provinces of the Amazonian Craton. Episodes, 22:174-182.

Tassinari, C.C.G.; Bettencourt, J.S.; Geraldes, M.C.; Macambira, M.J.B.; Lafon, J.M. 2000. The Amazonian Craton. In: Cordani, U.G.; Milani, E.J.; Filho, A.T.; Campos, D.A. (eds.) Tectonic Evolution of South America. Rio de Janeiro. p.41-95.

Tassinari, C.C.G. e Macambira, M.J.B. 2004. A evolução tectônica do Cráton Amazônico. In: Mantesso-Neto, V.; Bartorelli, A.; Carneiro, C.D.R.; Brito Neves, B.B. (eds.) Geologia do Continente Sul-Americano: Evolução da Obra de Fernando Flávio Marques de Almeida. São Paulo, p. 471-485.

Tolbert G.E., Tremaine J.W., Melcher G.C., Gomes C.B., 1971, The recently discovered Serra dos Carajás iron deposits, Northern Brazil: Economic Geology, v. 7, p. 985-994.

Townsend, T.E., 1987, Discrimination of iron alteration minerals in visible and near-infrared reflectance data: Journal of Geophysical Research-Solid Earth and Planets, v. 92, p. 1441–1454.

Trendall, A. F., Basei, M. A. S., Laeter, J. R., e Nelson, D. R., 1998. Shrimp zircon U-Pb constraints on the age of the Carajás Formation, Grão Pará Group, Amazon craton. Journal of South American Earth Sciences, 11, 265–277.

Van der Meer, F., 2004. Analysis of spectral absorption features in hyperspectral imagery. Int. J. Earth Observ. Geoinf. 5 (1), 55– 68.

Wirth, K. R., Gibbs, A. K., e Olszewski, W. J., J., 1986. U-Pb ages of zircons from the Grão-Pará Group and Serra dos Carajás Granite, Pará, Brazil. Revista Brasileira de Geociências, 16, 195–200.

Yang, K., Huntington, J. F., Gemmel, J. B., Scott, J. M., 2011. Variation on composition and abundanceof ehite mica in hydrothermal alteration system in Hellyer, Tasmania, as reveled by infrared reflectance spectroscopy. Journal of Geochemical Exploration, v. 108, p. 143-156.

Zhang, G.Y., Wasyliuk, K., and Pan, Y.M., 2001. The characterization and quantitative analysis of clay minerals in the Athabasca Basin, Saskatchewan: Application of shortwave infrared reflectance spectroscopy: Canadian Mineralogist, v. 39, p. 1347–1363.

# 5 CONCLUSÕES

# 5 CONCLUSÕES

Os algoritmos desenvolvidos para estimar a abundância e composição de alguns minerais a partir dos dados de espectrorradiometria de reflectância das amostras do depósito N4W foram validados utilizando dados de XRF com sucesso.

Os algoritmos espectrais validados incluem os seguintes:

1. A estimativa da abundância de (hidrox)óxidos de ferro, que mostrou uma correlação significativa com os dados de % Fe (XRF) para a maioria das ~1700 amostras de testemunho, com um RMSE de 15.8 % de Fe. Grande parte do erro está associado com mudanças dependentes do comprimento de onda no albedo das amostras, devido a uma combinação da variação no tamanho dos grãos e do comportamento transopaco dos (hidrox)óxidos de ferro, assim como diferentes quantidades de sílica (quartzo), gerando variações na distância entre o sensor e os (hidrox)óxidos de ferro.
2. A acurácia do algoritmo que determina a distribuição hematita-goetita foi validada utilizando os dados de perda ao fogo das amostras, que mostraram correlação significativa entre os valores do algoritmo e os resultados de perda ao fogo.
3. Os algoritmos de abundância das argilas aluminosas foram correlacionados com os dados de % Al2O3 (XRF), com um RMSE de 6 % para a caulinita e de 10.4% para gibbsita. Da mesma forma que os resultados dos (hidrox)óxidos de ferro, a acurácia da abundância de argilas aluminosas baseada nos espectros é influenciada negativamente pela presença de sílica nas amostras. Além disso, o erro também pode estar associado à substituição de Al na estrutura da goetita.
4. O algoritmo de abundância da clorita foi correlacionado com a porcentagem de $Fe_2O_3$ + MgO obtida nas análises de XRF. A abundância de clorita não mostrou uma correlação linear significativa com os dados de XRF. Entretanto, as cloritas identificas podem ser provenientes do metamorfismo ou do metasomatismo das rochas máficas do depósito N4WS. Portanto o aumento da abundância de clorita não esta necessariamente relacionado ao enriquecimento de Fe e/ou Mg das rochas máficas.

5. O algoritmo de composição da clorita foi correlacionada com a %MgO das análises de XRF. As amostras mostraram uma correlação significativa com os dados de XRF.
6. A abundância de talco obtida pelos dados de reflectância foi correlacionada com a %MgO obtida nas análises de XRF dos testemunhos de sondagem. O algoritmo mostrou uma correlação significativa com a %MgO das análises de XRF, apresentando um RMSE de 7.9% de MgO. Algumas amostras com a %MgO das análises de XRF elevada, possuem o valor de abundância obtido pelo algoritmo baixo. Entretanto, este erro pode ser devido a distribuição heterogênea do talco nas amostras, que dificulta a obtenção de espectros que representem a composição química de toda a amostra.
7. O algoritmo de abundância de carbonatos foi validado utilizando a soma da porcentagem de CaO e MgO obtida nas análise de XRF. O algoritmo mostrou baixa correlação com %CaO+%MgO obtida nas análises de XRF, apresentando RMSE de 6.8% de CaO+MgO. Entretanto, o reduzido número de amostras com carbonatos, dificulta a correlação destes dados.
8. O algoritmo de composição dos carbonatos foi validado utilizando a soma da porcentagem de CaO e MgO obtida nas análise de XRF, e mostrou correlação significativa com os dados de XRF.

Este estudo mostrou que a espectrorradiometria de reflectância no VNIR-SWIR pode ser utilizada para caracterizar e avaliar a distribuição da mineralogia de um depósito de ferro. Os principais minerais presentes no depósito de ferro N4WS foram identificados , incluindo a mineralogia do minério. O estudo das lâminas delgadas mostrou que todos os minerais identificados pela espectrorradiometria de reflectância estavam presentes nas amostras.

Os parâmetros de abundância mineral obtidos neste trabalho, com acurácia entre 6 e 15,8 % (RMSE), mostram que este método pode ser de grande utilidade como uma estimativa rápida do conteúdo de ferro e de alguns minerais relacionados ao depósito. Hillier (2000) mostrou que as análises quantitativas obtidas por DRX de argilas e outros minerais em arenitos, e em outras amostras de rochas em geral, são capazes de obter resultados com uma acurácia de ±3 % com um grau de confiança de 95%. Estas rotinas com DRX, entretanto, necessitam de bastante tempo para a preparação das amostras e coleta dos dados, e mesmo depois problemas podem surgir (ex. orientação preferencial, mistura de esmectita diferentes, etc.).

A análise dos parâmetros espectrais obtidos pelos algoritmos, além de identificar o minério, protominério e as encaixantes descritos durante o registro dos testemunhos, permitiu o detalhamento dos intervalos (Apêndices 1 e 2), possibilitando:

1. A identificação de minerais não descritos anteriormente dentro desses tipos rochoso, como o talco identificado em algumas amostras dos jaspilitos.
2. Discriminar as zonas que predominam hematita das zonas que predominam goetita nos intervalos de jaspilito e hematita friável.
3. Discriminar as zonas com maior conteúdo de óxidos nos intervalos do jaspilito e da hematita friável
4. Discriminar as zonas com carbonato nos intervalos do jaspilito.
5. Identificar a composição da clorita nos intervalos de basalto.
6. Diferenciar os basaltos da máfica semidecomposta pelo conteúdo de caulina obtido pelo algoritmo de abundância da caulinita.

A facilidade na estimativa de abundância mineral proporcionada pelo método pode ser de grande auxílio durante a lavra do depósito. A identificação de contaminantes como argilominerais, e a estimativa do teor do material lavrado facilita o beneficiamento no minério, uma vez que estas informações são de grande importância para a planta de beneficiamento.

Portanto, é de grande valor a rápida análise espectral de testemunhos de sondagem para gerar as informações necessárias pelos geocientistas para a caracterização mineralógica dos ambientes geológicos. Além disso, a aplicabilidade universal destes algoritmos espectrais estão se tornando realidade a medida que estudos de validação como este vem sendo feito utilizando diferentes sistemas espectrais em ambientes geológicos distintos.

# 6 REFERÊNCIAS BIBLIOGRÁFICAS

# 6 REFERÊNCIAS BIBLIOGRÁFICAS

Adams, J.B., 1974. Visible and near-infrared diffuse reflectance: spectra of pyroxenes as applied to remote sensing of solid objects in the solar system. J. Geophys. Res. 79, 4829–4836.

Adams, J.B., 1975. Interpretation of visible and near-infrared diffuse reflectance spectra of pyroxenes and other rock forming minerals. In: Karr, C. (Ed.), Infrared and Raman Spectroscopy of Lunar and Terrestrial Materials. Academic Press, New York, pp. 91–116.

Adams, J.B., and Filice, A.L., 1967, Spectral reflectance 0.4 to 2.0 microns of silicate rock powders: Journal of Geophysical Research, v. 72, p. 5705−5715.

Almeida, F. F. M., Hasui, Y., Neves, B. B. B., e Fuck, R. A. (1977). Províncias estruturais brasileiras (pp. 363–391). In: Simpósio de Geologia do Nordeste, 8, Campina Grande, 1977.: Atas... Campina Grande, SBG, p. 363-391.

Beisiegel, V.R., Bernardelli, A.L., Drummond, N.F., Ruff, A.W., Tremaine, J.W. 1973. Geologia e recursos minerais da Serra dos Carajás: Revista Brasileira de Geociências, v. 3: 215-242.

Bishop, J.L., Lane, M.D., Dyar, M.D., and Brown, A.J., 2008, Reflectance and emission spectroscopy study of four groups of phyllosilicates: Smectites, kaolinite-serpentines, chlorites and micas: Clay Minerals, v. 43, p. 35−54.Burns, R.G., 1993. Origin of electronic spectra of minerals in the visible and near-infrared region. In: Pieters, C.M., Englert, P.A.J. (Eds.), Remote Geochemical Analysis: Elemental and Mineralogical Composition. Cambridge University Press, New York, pp. 3–30.

Burns, R. Mineralogical Applications of Crystal Field Theory, Second Edition, Cambridge University Press, Cambridge, 551p. 1993.

Carioca, A. C., Costa, G. M., Barrón, V., Ferreira, C. M., Torrent, J. (2011). Application of diffuse reflectance spectroscopy in the quantification of the constituents of bauxite and iron ore. Revista Escola de Minas, Ouro Preto, v. 64(2), p. 199-204.

Clark, R.N., and Roush, T.L., 1984, Reflectance spectroscopy-quantitativeanalysis techniques for remote-sensing applications: Journal of GeophysicalResearch, v. 89, p. 6329−6340.

Clark, R.N., King, T.V.V., Klejwa, M., Swayze, G.A., and Vergo, N., 1990,High spectral resolution reflectance spectroscopy of minerals: Journal of Geophysical Research, v. 95, p. 12653−12680.

Crowley, J.K., and Vergo, N., 1988, Near-infrared reflectance spectra of mixtures of kaolin-group minerals: Use in clay mineral studies: Clays and Clay Minerals, v. 36, p. 310−316.

Cudahy, T., 1997a, Pima-II spectral characteristics of natural kaolins, CSIRO/AMIRA Project P435: Sydney, Australia, CSIRO Division for Exploration and Mining Report 420R, 62 p.

Cudahy, T., Jones, M., Thomas, M., Cocks, P., Agustin, F., Caccetta, M., … Rodger, A. (2009). Drill core logging of plagioclase feldspar composition and other minerals associated with Archean gold mineralization at Kambalda, Western Australia, using bidirectional thermal infrared reflectance system. Reviews in Economic Geology, 16, 223–235.

Cudahy, T., Jones, M., Thomas, M., Laukamp, C., Caccetta, M., Hewson, R.,Rodger, A., and Verrall, M., 2008, Next generation mineral mapping:Queensland Airborne HyMap and Satellite ASTER surveys 2006−2008:Perth, Publicly Available Report P2007/364 (http://c3dmm.csiro.au/NGMM/), CSIRO Exploration and Mining, 152 p.

Cudahy, T., and Ramanaidou, E.R., 1992, Relationships between spectral properties and ferric oxides, CSIRO/AMIRA Project P243: Wembley, Australia, CSIRO Division of Exploration Geoscience Report 244R, 68 p.

—1997, Measurement of the hematite:goethite ratio using field visible and near-infrared reflectance spectrometry in channel iron deposits, Western Australia: Australian Journal of Earth Sciences, v. 44, p. 411–420.

Curtiss, B., 1985, Evaluation of the physical properties of naturally occurringiron (III) oxyhydroxides on rock surfaces in arid and semi-arid regionsusing visible and near infrared spectroscopy: Unpublished Ph.D. thesis, Seattle, WA, University of Washington, 106 p.

Dall'Agnoll, R., e de Oliveira, D. C. (2007). Oxidized, magnetite-series, rapakivi- type granites of Carajás, Brazil: Implications for classification and petrogenesis of A-type granites. Lithos, 93, 215–233.

Dalstra, L. W., e Guedes, S. (2004). Giant hydrothermal hematite deposits with Mg-Fe metasomatism: A comparison of the Carajás, Hamersley, and other iron ores. Economic Geology, 99, 1793–1800.

Dardenne, M.A., Ferreira Filho, C.F., and Meirelles, M.R., 1988, The role of shoshonitic and calc-alkaline suites in the tectonic evolution of the Carajás district, Brazil: Journal of South American Earth Sciences, v. 1, p. 363–372.

DOCEGEO. (1988). Revisão litoestratigráfica da Província Mineral de Carajás: Congresso Brasileiro de Geologia, 35th, Sociedade Brasileira de Geologia, Belém, Brazil, 11–54.

Ducart, D. F. (2004). Caracterização da alteração hidrotermal associada às ocorrências auríferas de Los Menucos, Argentina, por meio de técnicas de sensoriamento remoto e espectroscopia de reflectância. Dissertação de Mestrado em Geociências. Universidade Estadual de Campinas,, 86.

Ducart, D. F. (2006). Alteração hidrotermal do prospecto aurífero Cerro La Mina, Los Menucos, Patagônia, Argentina: geologia, sensoriamento remoto e isótopos estáveis. Tese de dourado em Geociências. Universidade Estadual de Campinas, Campinas-SP, 173.

Ducart, D. F., Crósta, A. P., Souza Filho, C. R., e Coniglio, J. (2006). Alteration Mineralogy at the Cerro La Mina Epithermal Prospect, Patagonia, Argentina: Field Mapping, Short-Wave Infrared Spectroscopy, and ASTER Images. Economic Geology, 101, 981–996.

Fernandes, R. B. A., Barrón, V., Torrent, J., Fontes, M. P. F. (2004). Quantification of iron óxides of brazilian soils using diffuse reflectance spectroscopy.Revista Brasileira de Ciências do Solo, v.28, p. 245-257.

Ferreira, V. N., 2014. Caracterização de formações ferríferas bandadas através de dados de propriedades físicas de rocha e sua integração com dados aerogeofísicos: o estudo de caso do corpo N4WS, Serra Norte –Província Mineral de Carajás. Dissertção de mestrado, Universidade de Brasília.

Figueiredo e Silva, R. C., Lobato, L. M., Rosière, C. A., Hagemann, S., Zucchetti, M., Baars, F. J., … Andrade, I. (2008). Hydrothermal origin for the jaspilite-hosted, giant Serra Norte iron ore deposits in the Carajás mineral province, Para State, Brazil. Reviews in Economic Geology, 15, 255–290.

Gaffey, S.J., 1986, Spectral reflectance of carbonate minerals in the visible and near-infrared (0.35 to 2.55 microns): Calcite, aragonite, and dolomite: American Mineralogist, v. 71, p. 151–162.

Gibbs, A. K., Wirth, K. R., Hirata, W. K., e Olszewski, W. J., J. (1986). Age and composition of the Grão Pará Group volcanics, Serra dos Carajás. Revista Brasileira de Geociências, 16, 201–211.

Gonçalves, I. G., Petter, C. O., Machado, J. L. (2012). Quantification of hematite and goethite concentrations in kaolinusing diffuse reflectance spectroscopy: A new approach to Kubelka-Munk theory. Clays and Clay Minerals, v. 60, 473-483.

Grainger, C. J., Grooves, D. I., Tallarico, F. B., e Fletcher, I. R. (2008). Metallogenesis of the Carajás mineral province, southern Amazon craton, Brazil: Varying styles of Archean through Paleoproterozoic to Neoproterozoicbase- and precoius-metal mineralization. Ore Geology Reviews, 33, 451–484.

Haest, M., e Cudahy, T. (2012). Quantitative mineralogy from infrared spectroscopic data. I. Validation of mineral abundance and composition algoritmos at the rocklea channel iron deposit in Western. Economic Geology, 107(1983), 209–228. Retrieved from http://gsecongeo.highwire.org/content/107/2/209.short

Harraden C. L., Brian A. Mcnulty, Melissa J. Gregory, and James R. Lang. Shortwave Infrared Spectral Analysis of Hydrothermal Alteration Associated with the Pebble Porphyry Copper-Gold-Molybdenum Deposit, Iliamna, Alaska Economic Geology, v. 108, p. 483-494, doi:10.2113/econgeo.108.3.483. 2013.

Herrmann, W., Blake, M., Doyle, M., Huston, D., Kamprad, J., Merry, N. and Pontual, S.. Short wavelength infrared (SWIR) spectral analysis of hydrothermal alteration zones associated with base metal sulfide deposits at Rosebery and Western Tharsis, Tasmania, and Highway-Reward, Queensland. Economic Geology and the Bulletin of the Society of Economic Geologists, 96 (5), 939-955. 2001.

Hunt, G.R., 1977. Spectral signatures of particulate minerals in the visible and near-infrared. Geophysics 42, 501–513.

Hunt, G.R., and Ashley, R.P., 1979, Spectra of altered rocks in the visible and near-infrared: ECONOMIC GEOLOGY, v. 74, p. 1613−1629.

Hunt, G. R., and J. W. Salisbury, Visible and near-infrared spectra of minerals and rocks, I, Silicate minerals, Mod. Geol., 1, 283-300, 1970.

Hunt, G.R., Salisbury, J.W., and Lehnoff, C.J., 1971, Visible and near infrared spectra of minerals and rocks: III. Oxides and oxyhydroxides: Modern Geology,v. 2, p. 195−205.

Kruse, F. A., Boardman, J. W., e Huntington, J. F. (2003). Comparison of Airborne hyperspectral data and EO-1 Hyperion for mineral mapping. IEEE Transaction on Geosciences and Remote Sensing, 41(6), 1388–1400.

Krymsky, R. S., Macambira, J. B., e Macambira, M. B. J. (2002). Geocronologia U-Pb em zircão de rochas vulcânicas da Formação Carajás, Estado do Pará [abs.]. Simpósio sobre vulcanismo e ambientes associados, 2nd, Belém, Brazil, 41.

Lobato, L. M., Rosière, C. A., Figueiredo e Silva, R. C., Zucchetti, M., Baars, F. J., Seoane, J. C. S., … Monteiro, A. M. (2005). A mineralização hidrotermal de ferro da Província Mineral de Carajás-Controle estrutural e contexto na evolução metalogenética da província, in Marini, O.J., de Queiroz, E.T., and Ramos, B.W., eds., Caracterização de depósitos minerais em distritos mineir, 25–92.

Macambira, J. B., e Schrank, A. (2002). Químio-estratigrafia e evolução dos jaspilitos da Formação Carajás (PA). Revista Brasileira de Geociências, 32, 567–578.

Macambira J.B. 2003. O ambiente deposicional da Formação Carajás e uma proposta de modelo evolutivo para a Bacia Grão Pará. Tese de Doutorado, Instituto de Geociências, Universidade Estadual de Campinas, 217p.

Machado, N., Lindenmayer, Z., Krogh, T. E., e Lindenmayer, D. (1991). UPb geochronology of Archean magmatism and basement reactivation in the Carajás area, Amazon shield, Brazil. Precambrian Research, 49, 329–354.

Meirelles, E. M., Hirata, W. K., Amaral, A. F., Medeiros Filho, C. A., e Gato, W. C. (1984). Geologia das folhas Carajás e Rio Verde, Província Mineral de Carajás, Estado do Pará. Congresso Brasileiro de Geologia, Rio de Janeiro, Annals, 33, 2164–2174.

Morris, R.V., Lauer, H.V., Lawson, C.A., Gibson, E.K., Nace, G.A., and Stewart, C., 1985, Spectral and other physicochemcial properties of submicron powders of hematite (alpha-Fe2O3), maghemite (gamma-Fe2O3), magnetite (Fe3O4), goethite (alpha-FeOOH) and lepidocrocite (gamma-FeOOH): Journal of Geophysical Research-Solid Earth and Planets, v. 90, p. 3126–3144.

Mougeot, R. (1996). Estude de la limite Archeen-Proterozoique et des mineralizations Au, ±U associees. Exemples de la region de Jacobina (Etat de Bahia, Bresil) et de Carajás (Etat de Para, Bresil). Unpublished Ph.D. thesis, Monpellier, France, University of Montpellier II.

Olszewski, W. J., J., Wirth, K. R., Gibbs, A. K., e Gaudette, H. E. (1989). The age, origin, and tectonics of the Grão Pará Group and associated rocks, Serra dos Carajás, Brazil: Archean continental volcanism and rifting. Precambrian Research, 42, 229–254.

Post, J.L., and Noble, P.N., 1993, The near-infrared combination band frequencies of dioctahedral smectites, micas, and illites: Clays and Clay Minerals, v. 41, p. 639–644.

Rosière, C. A., Baars, F. J., Seoane, J. C. ., Lobato, L. M., da Silva, L. L., De Souza, S. R. C., e Mendes, G. E. (2006). Structure and iron mineralisation of the Carajás province. Transactions of the Institution of Mining and Metallurgy, 115, B126–B136.

Ross, P.-S, Bourke, A., Fresia, B. 2013. A multi-sensor logger for rock cores: Methodology and preliminary results from the Matagami mining camp, Canada. Ore Geology Reviews, v. 53, p. 93-111.

Santos, J. O. S. (2003). Geotectônica dos Escudos da Guianas e Brasil-Central, in Bizzi, L. A., Schobbenhaus, C., Vidotti, R. M., Gonçalves, J. H., eds., Geologia, Tectônica e Recursos Minerais do brasil, Compania de Pesquisa e Recursos Minerais-CPRM, 169–226.

Senna, J. A., Souza Filho C. R., Angélica R. S.(2008). Characterization of clays used in the ceramic manufacturing industry by reflectance spectroscopy: An experiment in the São Simão ball-clay deposit, Brazil. Applied clay science, v. 41, p 85-98.

Sherman, D.M., and Waite, T.D., 1985, Electronic spectra of Fe3+ oxides and oxide hydroxides in the near IR to near UV: American Mineralogist, v. 70, p. 1262–1269.

Silva, G. g., Lima, M. I. C., Andrade, A. R. F., Issler, R. S., e Guimarães, G. (1974). Geologi das folhas SB-22 Araguaia e parte da SC-22 Tocantins, in Levantamento de Recursos Minerais, Projeto Radam (Departamento Nacional de Produção Mineral-SNPM e Companhia de Pesquisa e Recursos Minerais-CPRM), 143 p.

Silva, R. e, e Hagemann, S. (2013). Hydrothermal Fluid Processes and Evolution of the Giant Serra Norte Jaspilite-Hosted Iron Ore Deposits, Carajás Mineral Province, Brazil. Economic ..., 108, 739–779. Retrieved from http://gsecongeo.highwire.org/content/108/4/739.short

Silva, S. M. P. (2009). Espectroscopia de imageamento e gamaespectrometria aérea e terrestre de pegmatitos e granitos da porção sul da Província Pegmatítica da Borborema (PPB), nordeste do Brasil. Tese de doutorado em Geociências, Universidade Estadual de Campinas, Campinas-SP, 173.

Sonntag, I., Laukamp, C., Hagemann, S. G. (2012). Low potassium hydrothermal alteration in low sulfidation epithermal systems as detected by IRS e XRD: An exemple from Co-O mine, eastern Mindanao, Philippines. Ore Geology Reviews, v. 45, p. 47-60.

Strezov, V., Ziolkowski, A., Evans, T.J., and Nelson, P.F., 2010, Assessment of evolution of loss on ignition matter during heating of iron ores: Journal of Thermal Analysis and Calorimetry, v. 100, p. 901–907.

Teixeira, J.B.G., 1994, Geochemistry, petrology, and tectonic setting of Archean basaltic and dioritic rocks from the N4 iron deposit, Serra dos Carajás, Pará, Brazil: Unpublished Ph.D. dissertation, State College, Pennsylvania, Pennsylvania State University, 161 p.

Townsend, T.E., 1987, Discrimination of iron alteration minerals in visible and near-infrared reflectance data: Journal of Geophysical Research-Solid Earth and Planets, v. 92, p. 1441–1454.

Trendall, A. F., Basei, M. A. S., Laeter, J. R., e Nelson, D. R. (1998). Shrimp zircon U-Pb constraints on the age of the Carajás Formation, Grão Pará Group, Amazon craton. Journal of South American Earth Sciences, 11, 265–277.

Van der Meer, F., 2004. Analysis of spectral absorption features in hyperspectral imagery. Int. J. Earth Observ. Geoinf. 5 (1), 55– 68.

Wirth, K. R., Gibbs, A. K., e Olszewski, W. J., J. (1986). U-Pb ages of zircons from the Grão-Pará Group and Serra dos Carajás Granite, Pará, Brazil. Revista Brasileira de Geociências, 16, 195–200.

Yang, K., Huntington, J. F., Gemmel, J. B., Scott, J. M. (2011). Variation on composition and abundanceof ehite mica in hydrothermal alteration system in Hellyer, Tasmania, as reveled by infrared reflectance spectroscopy. Journal of Geochemical Exploration, v. 108, p. 143-156.

Zhang, G.Y., Wasyliuk, K., and Pan, Y.M., 2001, The characterization and quantitative analysis of clay minerals in the Athabasca Basin, Saskatchewan: Application of shortwave infrared reflectance spectroscopy: Canadian Mineralogist, v. 39, p. 1347–1363.

Zucchetti, M., 2007, Rochas máficas do grupo Grão Pará e sua relação com a mineralização de ferro dos depósitos N4 E N5, Carajás, PA: Unpublished Ph.D. dissertation, Belo Horizonte, Brazil, Universidade Federal de Minas Gerais, 165 p.

# APÊNDICE 1

# APÊNDICE 1 - INTERPRETAÇÃO ESPECTRAL DOS FUROS

Resultados de abundância e composição mineral obtidos pelos dados de espectroscopia de reflectância para os furos F1023, F1100, F1115, F1498, 1012, F1348, F1495, F1065.

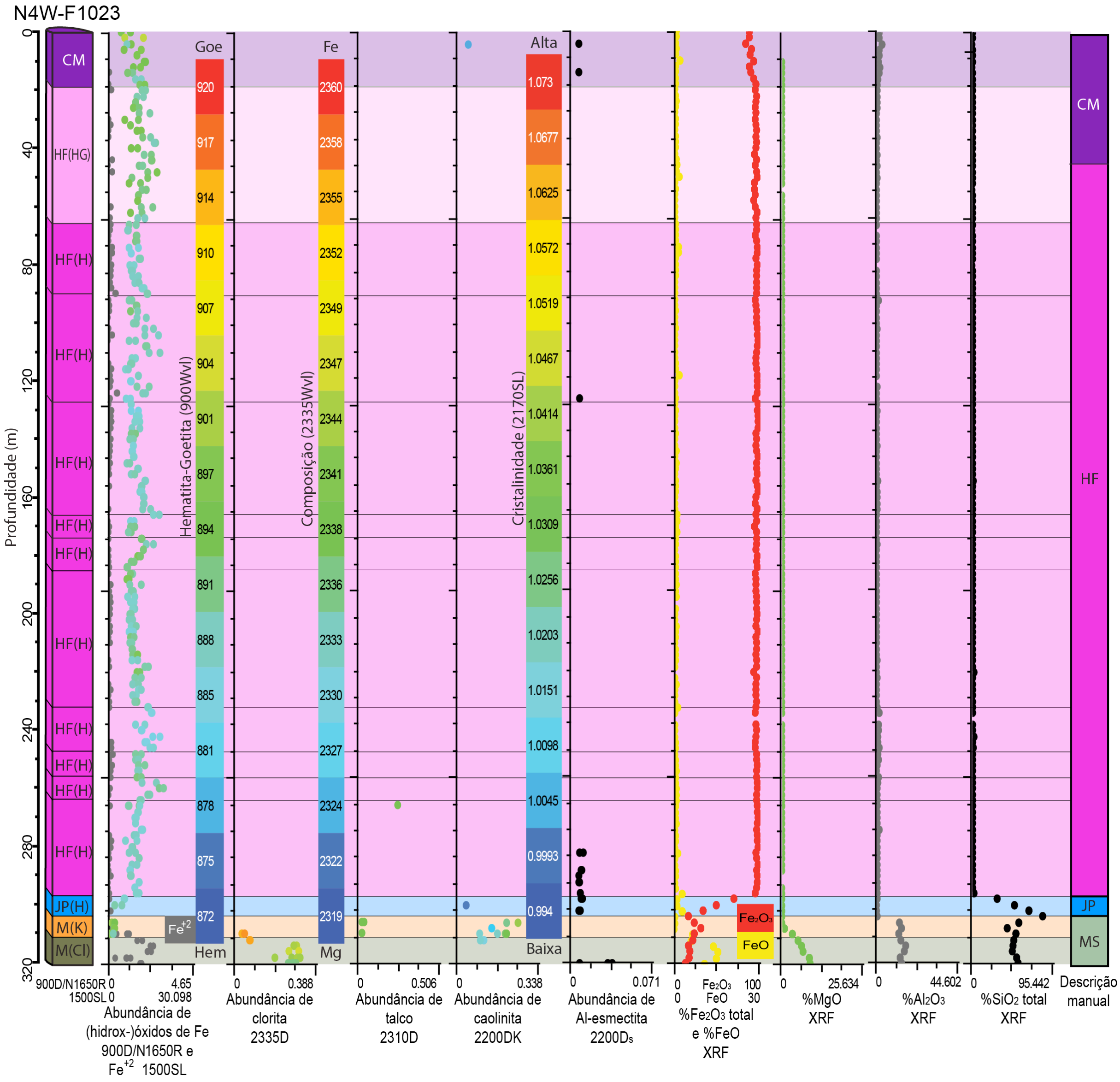

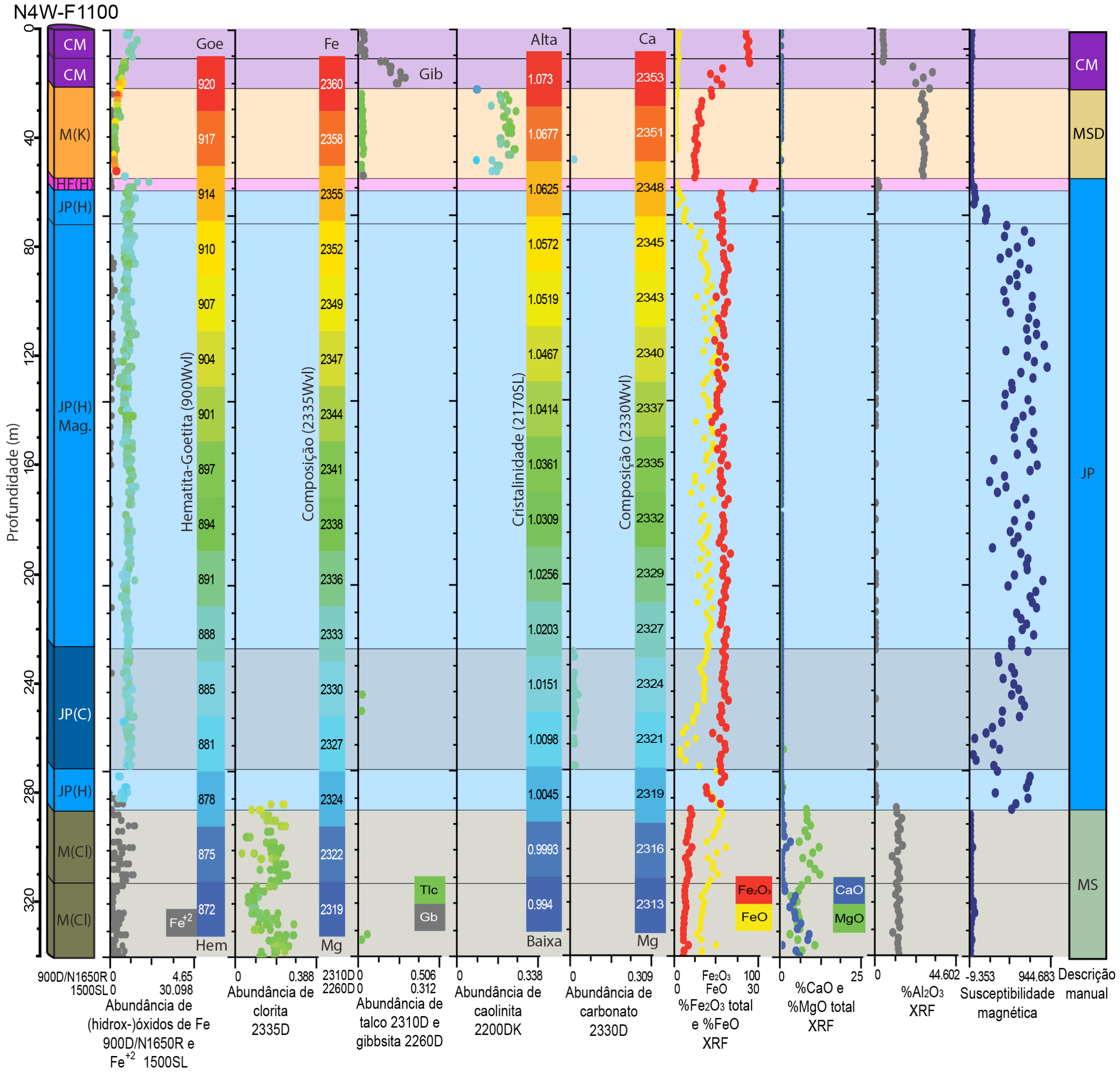

N4W-F1100

Profundidade (m)
0
40
80
120
160
200
240
280
320
CM
CM
M(K)
HF(H)
JP(H)
JP(H) Mag.
JP(C)
JP(H)
M(Cl)
M(Cl)
Goe
Hem
Fe$^{+2}$
Hematita-Goetita (900Wvl)
920
917
914
910
907
904
901
897
894
891
888
885
881
878
875
872
Fe
Mg
Composição (2335Wvl)
2360
2358
2355
2352
2349
2347
2344
2341
2338
2336
2333
2330
2327
2324
2322
2319
Gib
Tlc
Gb
Alta
Baixa
Cristalinidade (2170SL)
1.073
1.0677
1.0625
1.0572
1.0519
1.0467
1.0414
1.0361
1.0309
1.0256
1.0203
1.0151
1.0098
1.0045
0.9993
0.994
Ca
Mg
Composição (2330Wvl)
2353
2351
2348
2345
2343
2340
2337
2335
2332
2329
2327
2324
2321
2319
2316
2313
Fe2O3
FeO
CaO
MgO
CM
MSD
JP
MS
900D/N1650R 0 4.65
1500SL 0 30.098
Abundância de (hidrox-)óxidos de Fe 900D/N1650R e Fe$^{+2}$ 1500SL
0 0.388
Abundância de clorita 2335D
2310D 0 0.506
2260D 0 0.312
Abundância de talco 2310D e gibbsita 2260D
0 0.338
Abundância de caolinita 2200DK
0 0.309
Abundância de carbonato 2330D
0 Fe2O3 100
0 FeO 30
%Fe2O3 total e %FeO XRF
0 25
%CaO e %MgO total XRF
0 44.602
%Al2O3 XRF
-9.353 944.683
Susceptibilidade magnética
Descrição manual

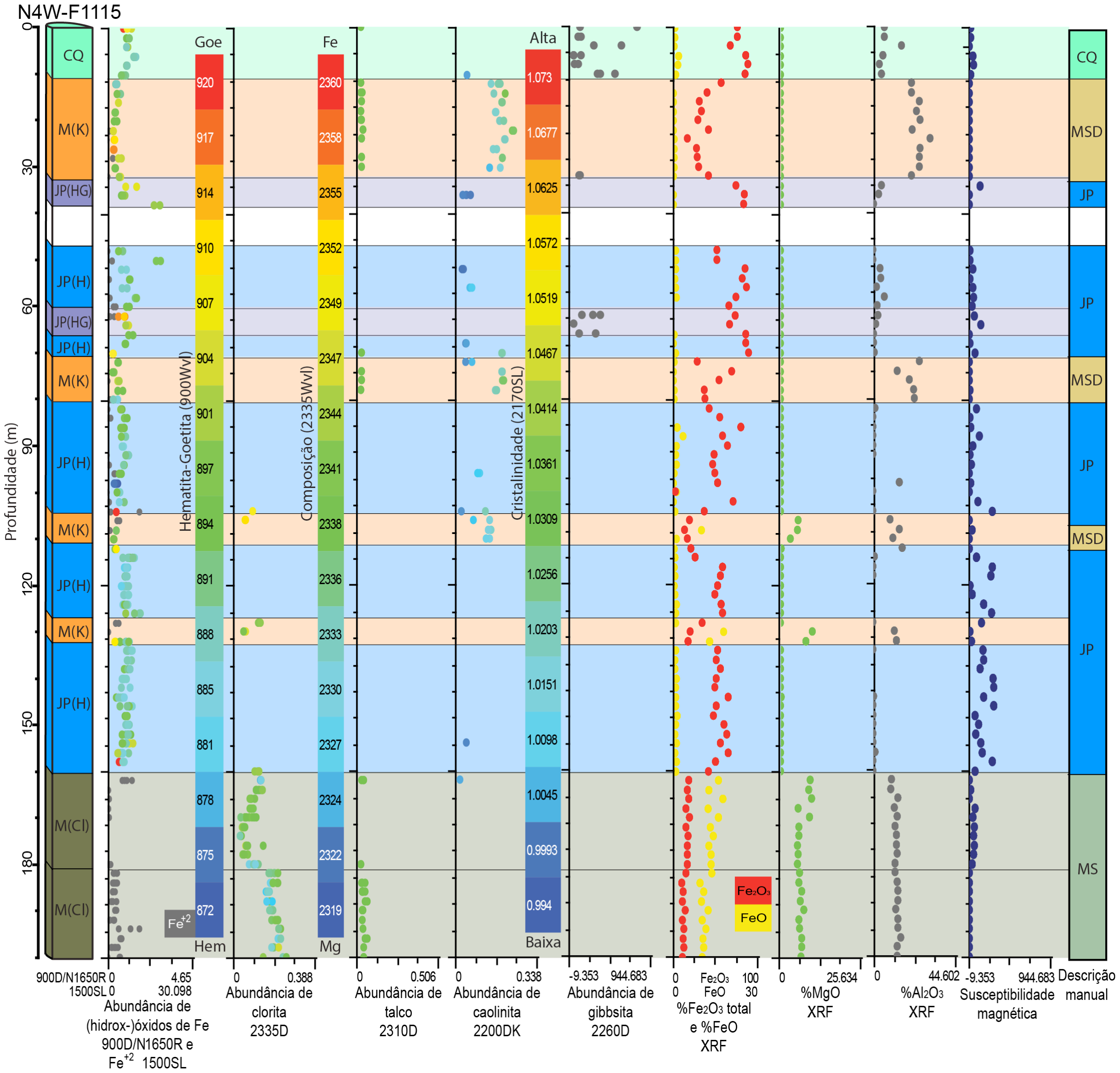
N4W-F1115
Profundidade (m)
0
30
60
90
120
150
180
CQ
M(K)
JP(HG)
JP(H)
JP(HG)
JP(H)
M(K)
JP(H)
M(K)
JP(H)
M(K)
JP(H)
M(Cl)
M(Cl)
Goe
920
917
914
910
907
904
901
897
894
891
888
885
881
878
875
872
Hem
Fe$^{+2}$
Hematita-Goetita (900Wvl)
Fe
2360
2358
2355
2352
2349
2347
2344
2341
2338
2336
2333
2330
2327
2324
2322
2319
Mg
Composição (2335Wvl)
Alta
1.073
1.0677
1.0625
1.0572
1.0519
1.0467
1.0414
1.0361
1.0309
1.0256
1.0203
1.0151
1.0098
1.0045
0.9993
0.994
Baixa
Cristalinidade (2170SL)
Fe$_2$O$_3$
FeO
CQ
MSD
JP
JP
MSD
JP
MSD
JP
MS
900D/N1650R 0 4.65
1500SL 0 30.098
Abundância de (hidrox-)óxidos de Fe 900D/N1650R e Fe$^{+2}$ 1500SL
0 0.388
Abundância de clorita 2335D
0 0.506
Abundância de talco 2310D
0 0.338
Abundância de caolinita 2200DK
-9.353 944.683
Abundância de gibbsita 2260D
0 Fe$_2$O$_3$ 100
0 FeO 30
%Fe$_2$O$_3$ total e %FeO XRF
0 25.634
%MgO XRF
0 44.602
%Al$_2$O$_3$ XRF
-9.353 944.683
Susceptibilidade magnética
Descrição manual

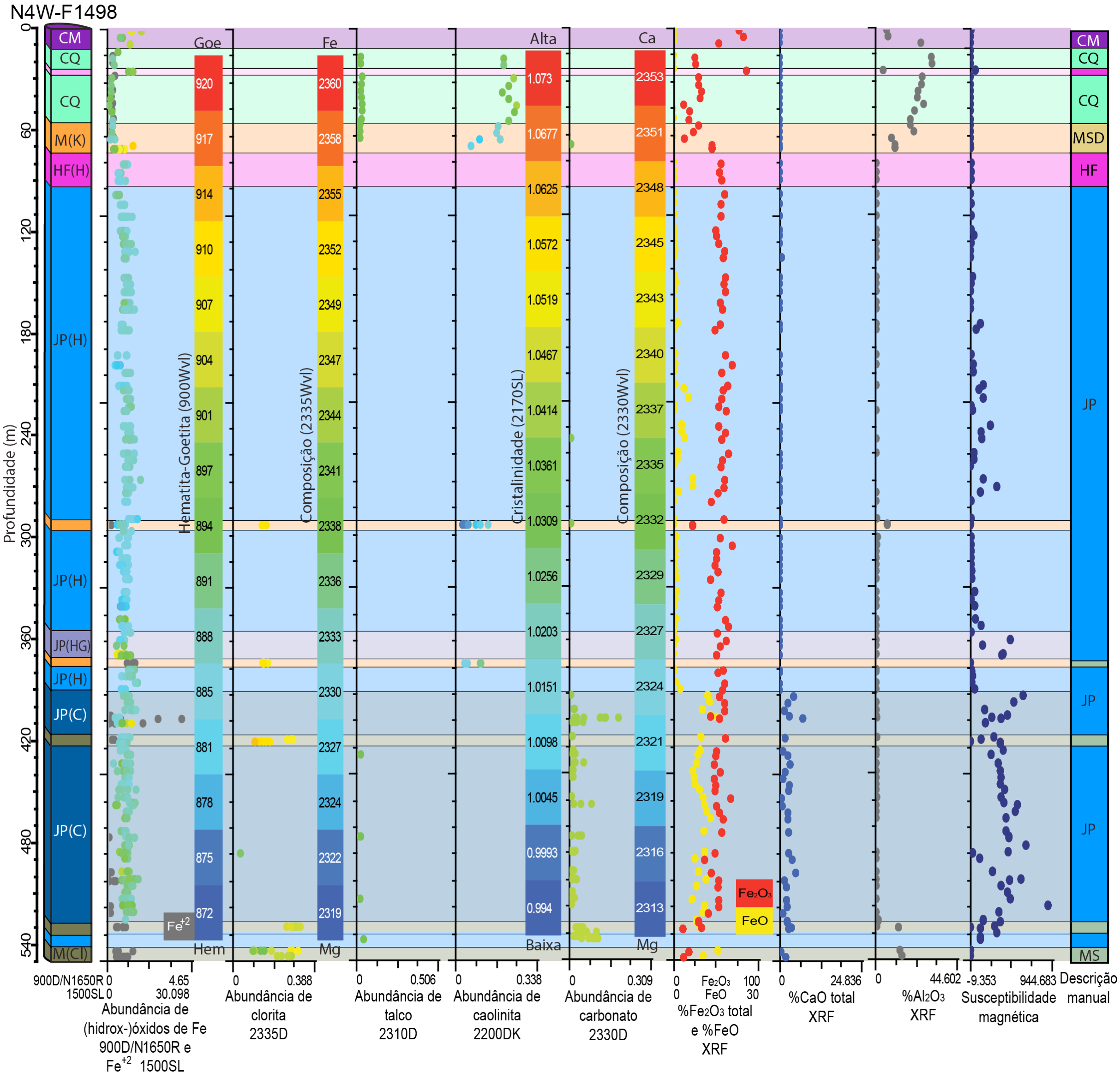
N4W-F1498
Profundidade (m)
0
60
120
180
240
300
360
420
480
540
CM
CQ
CQ
M(K)
HF(H)
JP(H)
JP(H)
JP(HG)
JP(H)
JP(C)
JP(C)
M(Cl)
Goe
920
917
914
910
907
904
901
897
894
891
888
885
881
878
875
872
Hem
Fe+2
Hematita-Goetita (900Wvl)
Fe
2360
2358
2355
2352
2349
2347
2344
2341
2338
2336
2333
2330
2327
2324
2322
2319
Mg
Composição (2335Wvl)
Alta
1.073
1.0677
1.0625
1.0572
1.0519
1.0467
1.0414
1.0361
1.0309
1.0256
1.0203
1.0151
1.0098
1.0045
0.9993
0.994
Baixa
Cristalinidade (2170SL)
Ca
2353
2351
2348
2345
2343
2340
2337
2335
2332
2329
2327
2324
2321
2319
2316
2313
Mg
Composição (2330Wvl)
Fe₂O₃
FeO
CM
CQ
CQ
MSD
HF
JP
JP
JP
MS
900D/N1650R 0 4.65
1500SL 0 30.098
Abundância de (hidrox-)óxidos de Fe 900D/N1650R e Fe+2 1500SL
0 0.388
Abundância de clorita 2335D
0 0.506
Abundância de talco 2310D
0 0.338
Abundância de caolinita 2200DK
0 0.309
Abundância de carbonato 2330D
0 Fe₂O₃ 100
0 FeO 30
%Fe₂O₃ total e %FeO XRF
0 24.836
%CaO total XRF
0 44.602
%Al₂O₃ XRF
-9.353 944.683
Susceptibilidade magnética
Descrição manual

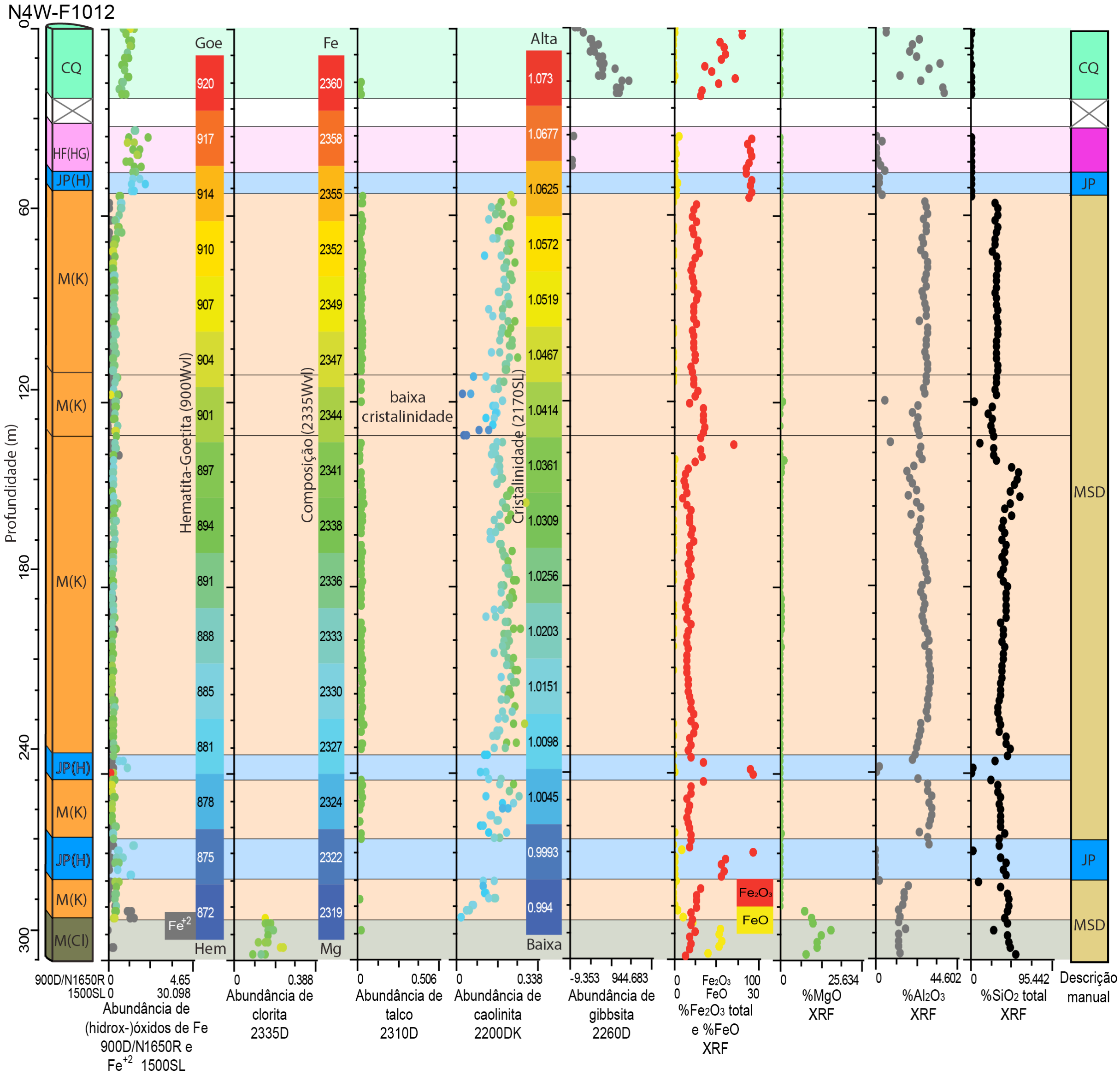
N4W-F1012
Profundidade (m)
0
60
120
180
240
300
CQ
HF(HG)
JP(H)
M(K)
M(K)
M(K)
JP(H)
M(K)
JP(H)
M(K)
M(Cl)
Goe
Hematita-Goetita (900Wvl)
920
917
914
910
907
904
901
897
894
891
888
885
881
878
875
872
Hem
Fe+2
Fe
Composição (2335Wvl)
2360
2358
2355
2352
2349
2347
2344
2341
2338
2336
2333
2330
2327
2324
2322
2319
Mg
baixa cristalinidade
Alta
Cristalinidade (2170SL)
1.073
1.0677
1.0625
1.0572
1.0519
1.0467
1.0414
1.0361
1.0309
1.0256
1.0203
1.0151
1.0098
1.0045
0.9993
0.994
Baixa
Fe₂O₃
FeO
CQ
JP
MSD
JP
MSD
900D/N1650R 0 4.65
1500SL 0 30.098
Abundância de (hidrox-)óxidos de Fe 900D/N1650R e Fe+2 1500SL
0 0.388
Abundância de clorita 2335D
0 0.506
Abundância de talco 2310D
0 0.338
Abundância de caolinita 2200DK
-9.353 944.683
Abundância de gibbsita 2260D
0 Fe₂O₃ 100
0 FeO 30
%Fe₂O₃ total e %FeO XRF
0 25.634
%MgO XRF
0 44.602
%Al₂O₃ XRF
0 95.442
%SiO₂ total XRF
Descrição manual

N4W-F1348

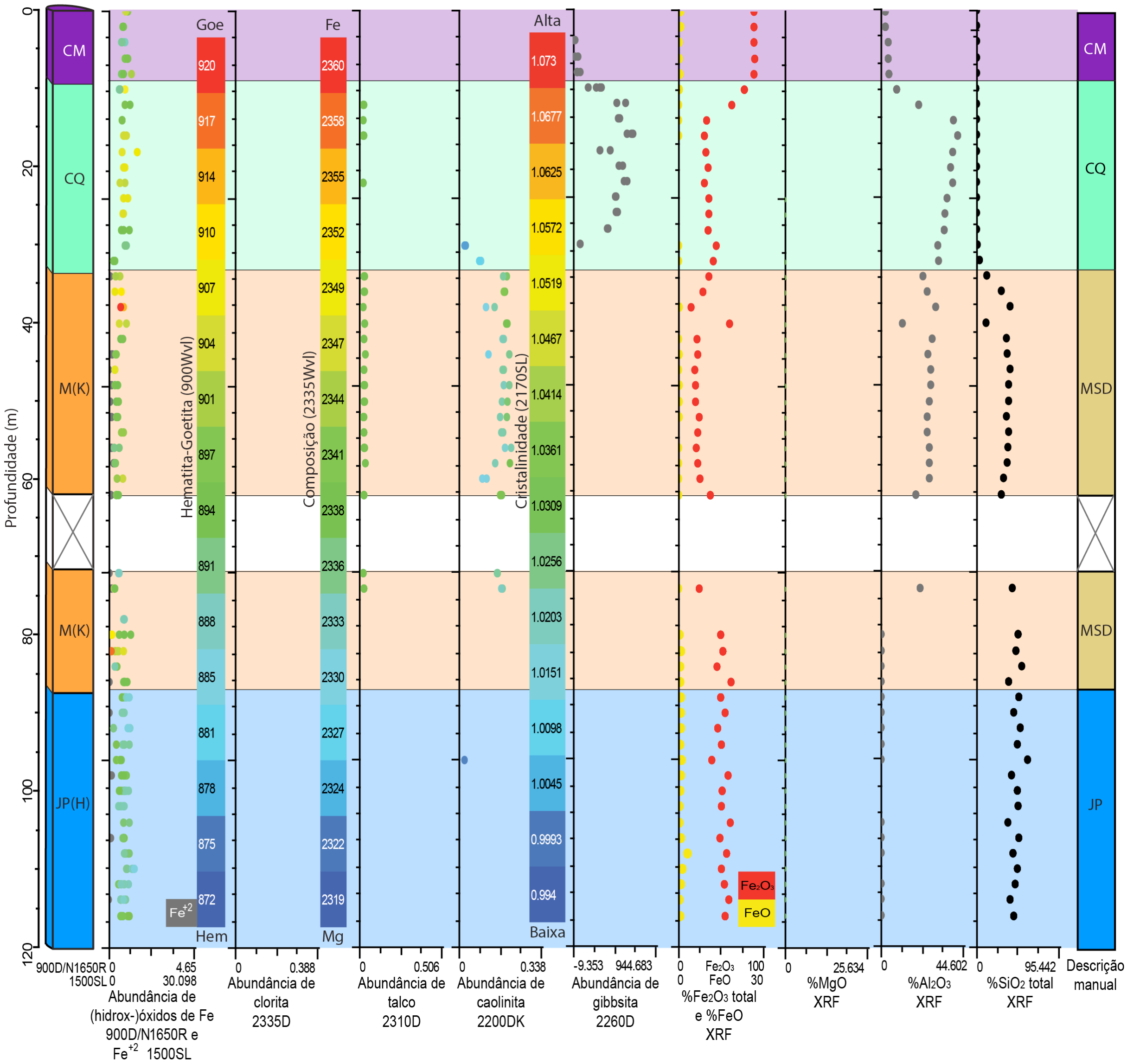
Profundidade (m)
0
20
40
60
80
100
120
CM
CQ
M(K)
M(K)
JP(H)
Goe
920
917
914
910
907
904
901
897
894
891
888
885
881
878
875
872
Hem
Fe+2
Hematita-Goetita (900Wvl)
Fe
2360
2358
2355
2352
2349
2347
2344
2341
2338
2336
2333
2330
2327
2324
2322
2319
Mg
Composição (2335Wvl)
Alta
1.073
1.0677
1.0625
1.0572
1.0519
1.0467
1.0414
1.0361
1.0309
1.0256
1.0203
1.0151
1.0098
1.0045
0.9993
0.994
Baixa
Cristalinidade (2170SL)
Fe2O3
FeO
CM
CQ
MSD
MSD
JP
900D/N1650R 0 4.65
1500SL 0 30.098
Abundância de (hidrox-)óxidos de Fe 900D/N1650R e Fe+2 1500SL
0 0.388
Abundância de clorita 2335D
0 0.506
Abundância de talco 2310D
0 0.338
Abundância de caolinita 2200DK
-9.353 944.683
Abundância de gibbsita 2260D
0 Fe2O3 100
0 FeO 30
%Fe2O3 total e %FeO XRF
0 25.634
%MgO XRF
0 44.602
%Al2O3 XRF
0 95.442
%SiO2 total XRF
Descrição manual

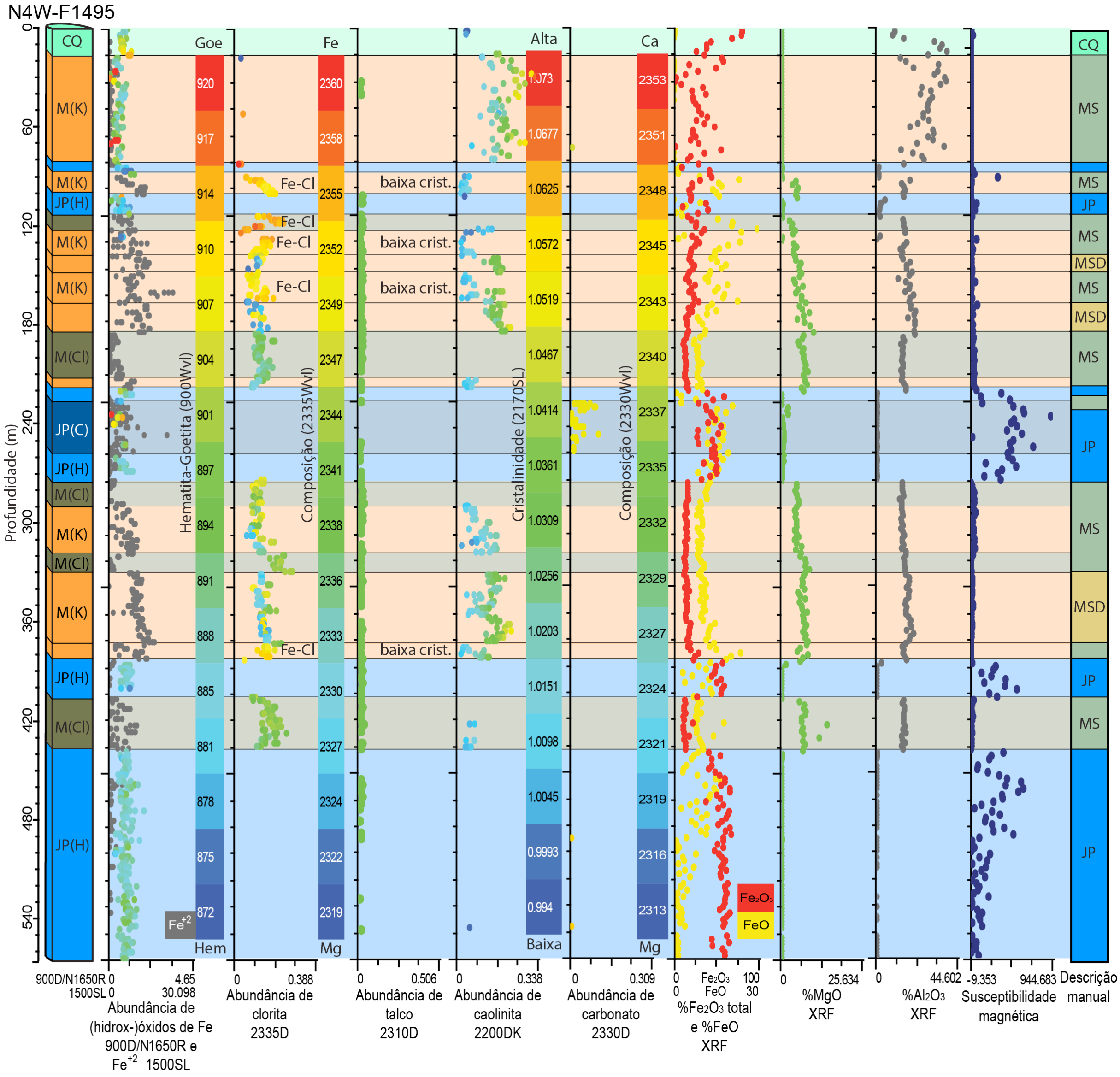
N4W-F1495
Profundidade (m)
0
60
120
180
240
300
360
420
480
540
CQ
M(K)
JP(H)
M(Cl)
JP(C)
Goe
Hem
Fe+2
Hematita-Goetita (900Wvl)
920
917
914
910
907
904
901
897
894
891
888
885
881
878
875
872
900D/N1650R 0 4.65
1500SL 0 30.098
Abundância de (hidrox-)óxidos de Fe 900D/N1650R e Fe+2 1500SL
Fe
Mg
Fe-Cl
Composição (2335Wvl)
2360
2358
2355
2352
2349
2347
2344
2341
2338
2336
2333
2330
2327
2324
2322
2319
0 0.388
Abundância de clorita 2335D
baixa crist.
0 0.506
Abundância de talco 2310D
Alta
Baixa
Cristalinidade (2170SL)
1.073
1.0677
1.0625
1.0572
1.0519
1.0467
1.0414
1.0361
1.0309
1.0256
1.0203
1.0151
1.0098
1.0045
0.9993
0.994
0 0.338
Abundância de caolinita 2200DK
Ca
Mg
Composição (2330Wvl)
2353
2351
2348
2345
2343
2340
2337
2335
2332
2329
2327
2324
2321
2319
2316
2313
0 0.309
Abundância de carbonato 2330D
Fe2O3
FeO
0 Fe2O3 100
0 FeO 30
%Fe2O3 total e %FeO XRF
0 25.634
%MgO XRF
0 44.602
%Al2O3 XRF
-9.353 944.683
Susceptibilidade magnética
CQ
MS
JP
MSD
Descrição manual

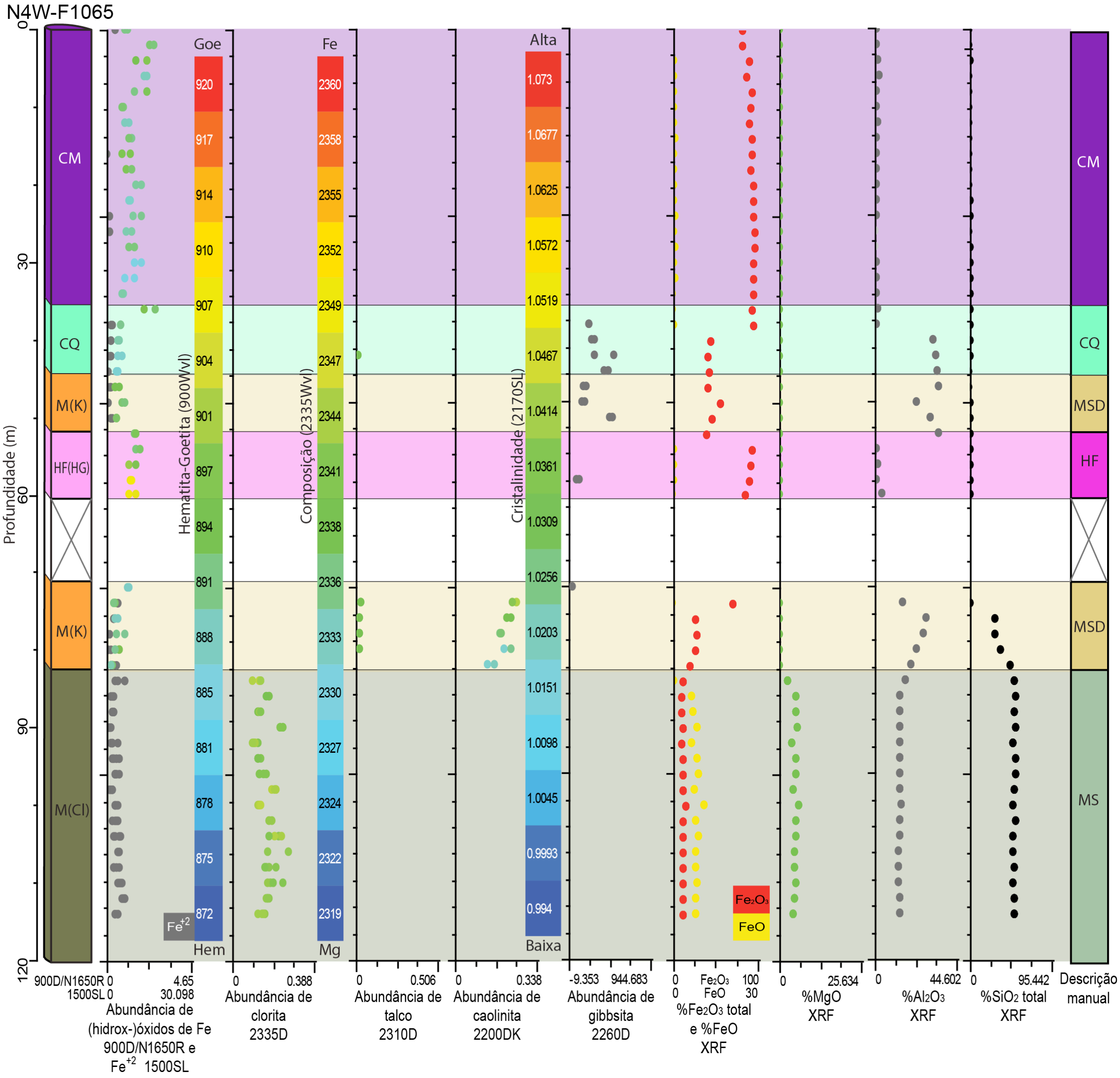
N4W-F1065
Profundidade (m)
0
30
60
90
120
CM
CQ
M(K)
HF(HG)
M(K)
M(CI)
Goe
920
917
914
910
907
904
901
897
894
891
888
885
881
878
875
872
Hem
Fe+2
Hematita-Goetita (900Wvl)
Fe
2360
2358
2355
2352
2349
2347
2344
2341
2338
2336
2333
2330
2327
2324
2322
2319
Mg
Composição (2335Wvl)
Alta
1.073
1.0677
1.0625
1.0572
1.0519
1.0467
1.0414
1.0361
1.0309
1.0256
1.0203
1.0151
1.0098
1.0045
0.9993
0.994
Baixa
Cristalinidade (2170SL)
Fe2O3
FeO
900D/N1650R 0 4.65
1500SL 0 30.098
Abundância de (hidrox-)óxidos de Fe 900D/N1650R e Fe+2 1500SL
0 0.388
Abundância de clorita 2335D
0 0.506
Abundância de talco 2310D
0 0.338
Abundância de caolinita 2200DK
-9.353 944.683
Abundância de gibbsita 2260D
0 Fe2O3 100
0 FeO 30
%Fe2O3 total e %FeO XRF
0 25.634
%MgO XRF
0 44.602
%Al2O3 XRF
0 95.442
%SiO2 total XRF
Descrição manual
CM
CQ
MSD
HF
MSD
MS

# APÊNDICE 2

# APÊNDICE 2 - SEÇÕES LITOLÓGICAS INTERPRETADAS

Seções litológicas interpretadas do corpo N4WS entre os testemunhos N4W-1495, N4W-1023, N4W-1348 E N4W-1398, N4W-1115, N4W-1100. A litologia (à esquerda) e os domínios espectrais (à direita) destes testemunhos são mostrados. Os testemunhos não identificados foram adicionados para facilitar a interpretação, mostrando apenas a litologia. As linhas pontilhadas indicam possíveis falhamentos.

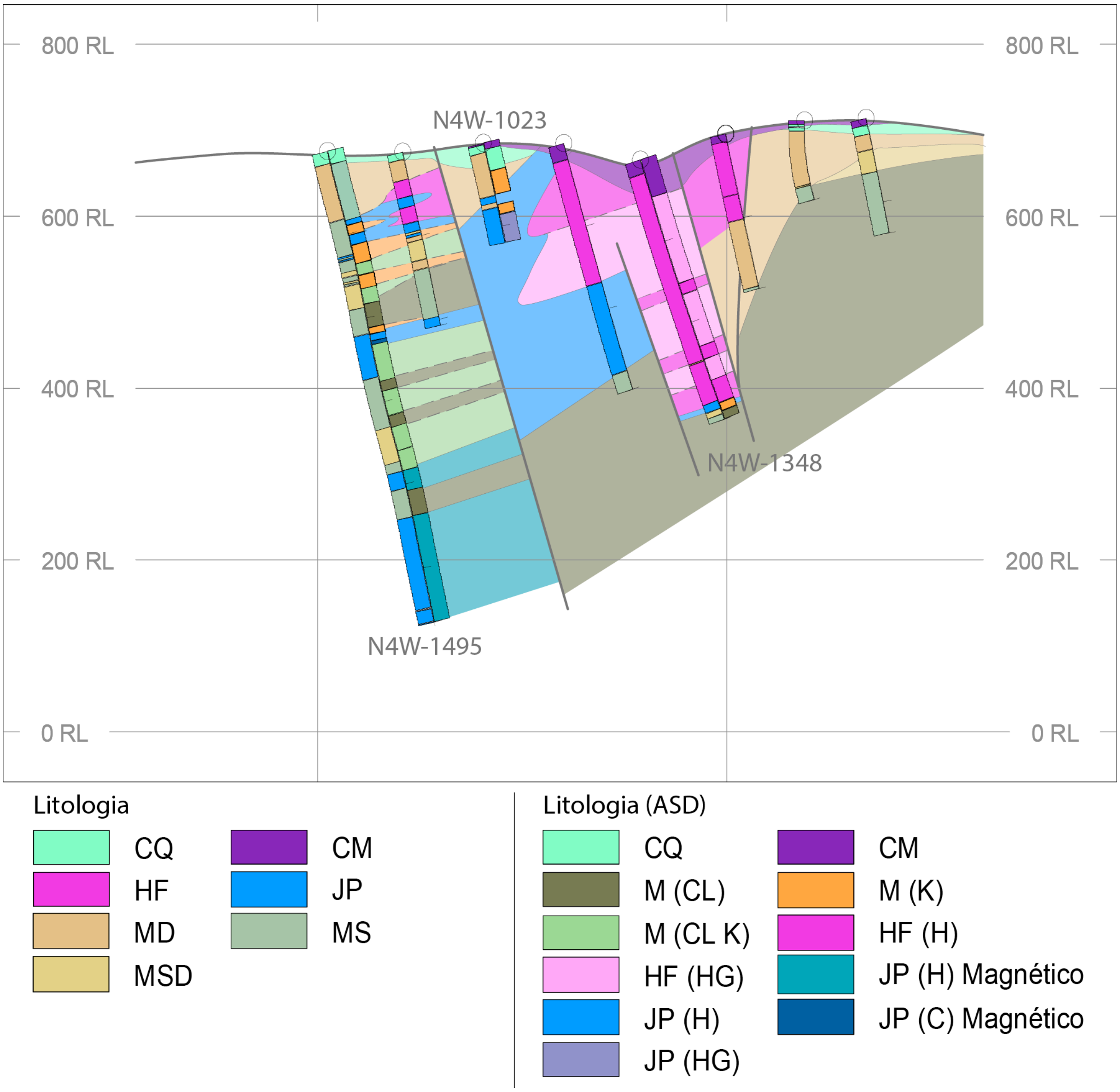

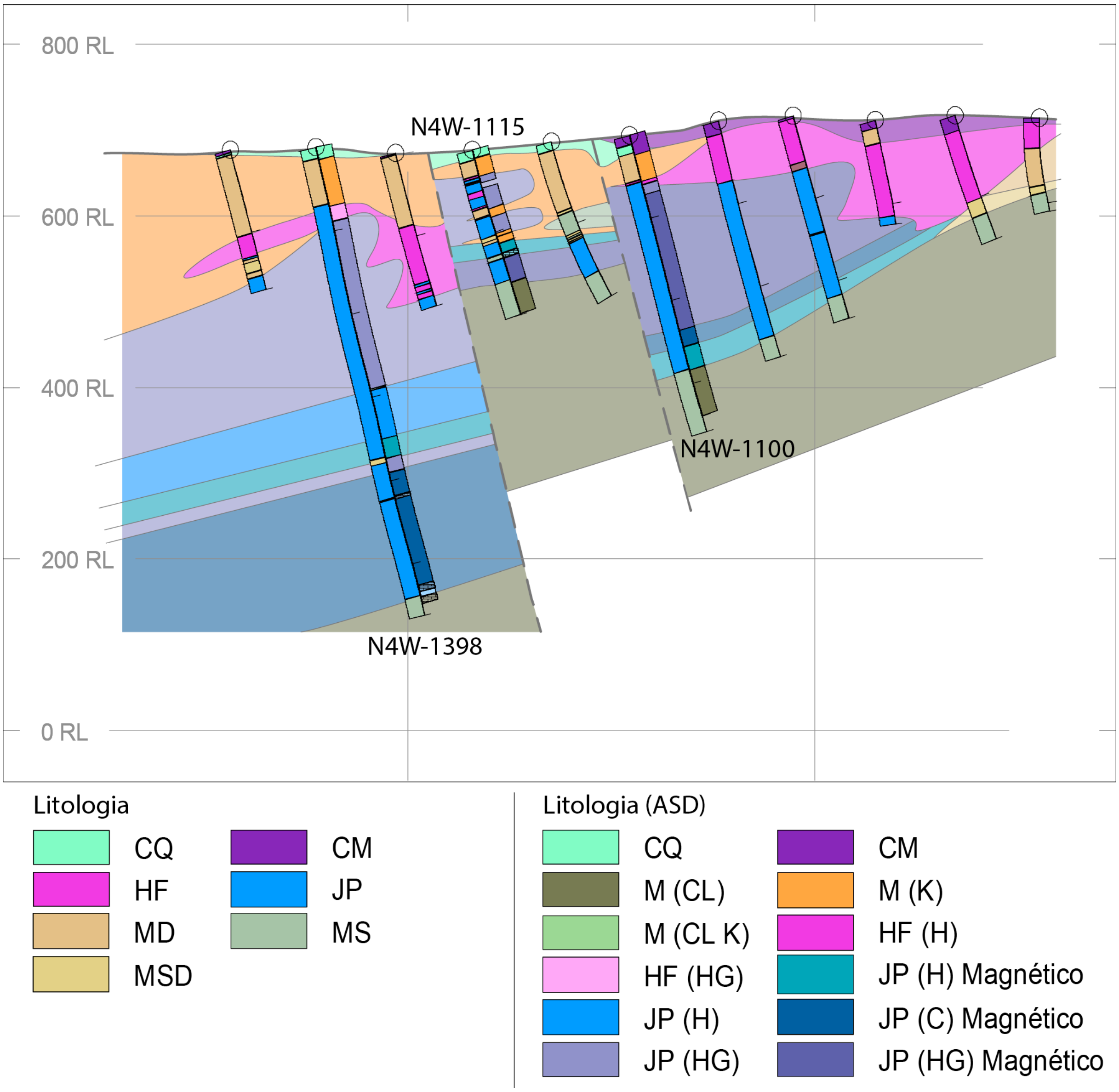
800 RL
600 RL
400 RL
200 RL
0 RL
N4W-1115
N4W-1100
N4W-1398
Litologia
CQ
HF
MD
MSD
CM
JP
MS
Litologia (ASD)
CQ
M (CL)
M (CL K)
HF (HG)
JP (H)
JP (HG)
CM
M (K)
HF (H)
JP (H) Magnético
JP (C) Magnético
JP (HG) Magnético